

NANO-METALLIC OPTICS FOR
WAVEGUIDES AND PHOTODETECTORS

A DISSERTATION
SUBMITTED TO THE DEPARTMENT OF ELECTRICAL
ENGINEERING
AND THE COMMITTEE ON GRADUATE STUDIES
OF STANFORD UNIVERSITY
IN PARTIAL FULFILLMENT OF THE REQUIREMENTS
FOR THE DEGREE OF
DOCTOR OF PHILOSOPHY

Şükrü Ekin Kocabas
September 2009

© Copyright by Şükrü Ekin Kocabaş 2009

All Rights Reserved

I certify that I have read this dissertation and that, in my opinion, it is fully adequate in scope and quality as a dissertation for the degree of Doctor of Philosophy.

(David A.B. Miller) Principal Adviser

I certify that I have read this dissertation and that, in my opinion, it is fully adequate in scope and quality as a dissertation for the degree of Doctor of Philosophy.

(Mark Brongersma)

I certify that I have read this dissertation and that, in my opinion, it is fully adequate in scope and quality as a dissertation for the degree of Doctor of Philosophy.

(Shanhui Fan)

Approved for the University Committee on Graduate Studies.

સુ

Abstract

This dissertation focuses on the use of nano-metallic structures in optical systems, specifically in waveguide geometries and photodetectors. The use of metals makes it possible to design optical components that are smaller than the wavelength of light. The optical properties of metals at infrared and visible wavelengths enable such designs.

The first part of the dissertation focuses on waveguides and investigates the metal-insulator-metal (MIM) geometry. We begin by deriving the full set of modes that the MIM geometry supports. We show the necessity of taking into consideration all supported modes through the use of mode-matching calculations. Following our analysis of the modal structure of the MIM waveguides, we then illustrate how to analyze junctions of MIM waveguides by designing a mode converter which converts the mode of a large waveguide into that of a smaller waveguide. Our analysis uses scattering matrices and is much faster than full-field simulations. We conclude the first part of the dissertation by providing an exact circuit model for waveguide junctions.

The second part of the dissertation is about scattering of light off of nano-metallic volumes. We review various techniques of scattering analysis, and then illustrate a photodetector design which integrates an antenna for near-infrared wavelengths with a sub-wavelength volume of Ge. The use of the antenna makes it possible to focus light into a sub-wavelength volume. We then describe the experimental work we did with Si photodetectors of different geometries and provide our measurement results. Finally, we present our conclusions.

દ્વા

Acknowledgements

There are many factors that affect a person’s education, and therefore the formation of a dissertation.¹ The parents—who they are, what they do, whom they know—make a huge difference. I would first of all like to thank my mother and father, without whom I would not be. My sister, as well, has greatly helped me become who I am.

The dissertation focuses on different aspects of theoretical and experimental optics. On the experimental side, I received assistance from a number of friends. Rohan Kekatpure, Onur Fidaner, Ali Kemal Okyay all taught me some aspects of clean room fabrication. The staff at the Stanford Nanofabrication Facility were very helpful as well. I especially thank James Conway for the enthusiasm with which he shared his knowledge on e-beam technology.

Also on the experimental side, I received a lot of assistance from Salman Latif, Dany-Sébastien Ly-Gagnon, and Krishna C. Balram on setting up optics, experimental planning, nano-fabrication recipe development and various measurements. It was a pleasure working with them and I cannot overemphasize their contribution to the work described in this dissertation. Furthermore, I enjoyed collaborating with Luke Tang and Ali Kemal Okyay on the Ge based photodetector work.

On the modeling and theory side, I closely worked with Georgios Veronis and Shanhui Fan and learned a lot from their insightful analyses and comments. Furthermore, Mark Brongersma’s encouragement and his excitement about research were a source of inspiration for me.

¹Writing the acknowledgements section of a dissertation is harder than one might think. As noted in [1], “dissertation acknowledgments are, like other academic texts, staged genres with a coherent structure,” where “the constraints of academic discourses still operate.”

I am indebted to David A. B. Miller for the invaluable role that he played as my advisor. In addition to asking critically important questions, he also had great suggestions whenever I was stuck on a problem. I learned a lot about teaching and writing from him as well.

Lastly, all the friends that I interacted with during my PhD years made life much more enjoyable and meaningful. I hope we continue to keep in touch.

*Omnesque medicinam Romae
professos et liberalium artium
doctores, quo libentius et ispi urbem
incolerent et coeteri appeterent
civitate donavit.*

He conferred citizenship on all who practiced medicine at Rome, and on all teachers of the liberal arts, to make them more desirous of living in the city and to induce others to resort to it.[†]

[†]Suetonius, *The Lives of the Caesars*, vol. I, XLII, with an English translation by J.C. Rolfe, Harvard University Press, Cambridge, MA, 1998, p. 89.

સુ

ં

Contents

Title Page	i
Copyright Page	ii
Signature Page	iii
Abstract	v
Acknowledgements	vii
Contents	xi
List of Tables	xiv
List of Figures	xv
1 Introduction	I
2 Background Information	7
2.1 Permittivity of Metals	7
2.1.1 Microwave Regime	II
2.1.2 Infrared Regime	12
2.1.3 Ultraviolet Regime	12
2.2 Surface Impedance of Metals	I3
2.3 Metal - Insulator Waveguides	I6
2.4 Metal - Insulator - Metal Waveguides	I8

3 Metal–Insulator–Metal Modes	23
3.1 Introduction	23
3.2 Some Definitions	26
3.3 Spectrum	29
3.3.1 Point Spectrum	31
3.3.2 Continuous Spectrum	35
3.3.3 Residual Spectrum	37
3.3.4 Orthogonality relationships	38
3.4 Mode-Matching	41
3.4.1 Birth of the Discretuum	43
3.4.2 Are the modes complete?	45
3.4.3 Field Stitching	47
3.5 Discussion	52
3.6 Conclusion	56
4 Circuit Theory for MIM Waveguides	59
4.1 Introduction	59
4.2 Scattering Matrix Description of Junctions	61
4.3 Cascade Connection of Junctions	67
4.3.1 Conditions for Zero Reflection	68
4.3.2 Mode Converter Design	71
4.4 Circuit Model for the Waveguide Junction	73
4.4.1 Exact Model	75
4.4.2 Simplified Model	78
4.4.3 Interpretation of Circuit Models	79
4.5 Conclusion	81
5 Fundamentals of Antennas	83
5.1 Introduction	83
5.2 Basics of Antenna Theory	84
5.3 Antennas as Scatterers	87
5.3.1 Mie Theory	87

5.3.2	Method of Moments	94
5.3.3	Finite-Difference Time-Domain	98
5.3.4	Green's Function Methods	105
5.3.5	Summary	106
5.4	Sleeve Dipole Design for a Closely Integrated Antenna-Detector System	106
6	Fabrication and Measurement Results	113
6.1	Introduction	113
6.2	Changes in the Design at 850 nm	114
6.3	Clean Room Fabrication	114
6.3.1	SOI thinning	118
6.3.2	Shaping the Silicon	118
6.3.3	Crowning the Silicon with a Golden Antenna	121
6.4	Opto-Electronic Measurement Setup	123
6.4.1	Optics	124
6.4.2	Electronics	125
6.4.3	Mechanics	127
6.5	Measurement Results and Discussion	127
6.5.1	Transport	128
6.5.2	Photoresponse	132
6.6	Concluding Remarks	139
7	Conclusion	141
A	Overview of Maxwell's Equations for Guided Modes	147
B	Argument Principle Method	150
C	Some Details of the Mode Matching Algorithm	152
D	Fabrication Recipe	153
	Bibliography	157

List of Tables

3.1	Adjectives used to describe the modes of MIM	40
3.2	κ_m/k_0 values for the modes labeled in Figure 3.4	42
5.1	Third order Lorentz fit to experimental permittivity values for Au around 1500 nm.	109
6.1	Fourth order Lorentz fit to experimental permittivity values for Au around 850 nm.	114

List of Figures

2.1	Simple model for the electrons in the Lorentz model.	8
2.2	Distribution of positively charged ions and negatively charged electrons before and after the application of electric field.	9
2.3	Phase and amplitude of the permittivity for a Drude metal with $\delta = 1/\tau = 0.01\omega_p$	11
2.4	Real and imaginary parts of the surface impedance for Au.	15
2.5	Geometry of the surface plasmon.	16
2.6	Normalized $\omega - k$ diagram for an MI waveguide with $\delta = 1/\tau = 0.05\omega_p$. .	18
2.7	Skin depth vs ω for the surface plasmon mode and the bulk metal for $\delta = 1/\tau = 0.05\omega_p$	19
2.8	Mode profile for an MI waveguide with $\delta = 0.05\omega_p$	20
2.9	Geometry of the metal-insulator-metal (MIM) parallel plate waveguide. .	20
3.1	Qualitative properties of the MIM geometry as a function operation frequency	26
3.2	Classification of the spectrum for an operator in a general space.	29
3.3	Geometry for the even modes of the MIM waveguide.	30
3.4	Spectrum of the MIM waveguide.	35
3.5	Spectrum of the MIM waveguide as a function of $d = 2a$, $\text{Re}(k_z/k_0)$ and $\text{Im}(k_z/k_0)$	36
3.6	Visualization of the spectrum on the κ_m plane.	42
3.7	Effects of loss on the spectrum.	43
3.8	Geometry for mode matching calculations.	44
3.9	Effects of termination of the metal by a PEC wall on the spectrum.	45

3.10	Effects of the continuous spectrum on mode expansion.	48
3.11	Convergence study of the reflection coefficient, R_{11}^L , of the main mode of the left waveguide traveling toward the right waveguide.	50
3.12	Magnetic field H_y at the junction of two MIM waveguides as a result of the scattering of the main mode of the left waveguide traveling toward the right.	51
3.13	Reflection coefficient of the main mode at the junction between two MIM waveguides of different insulator thicknesses.	52
4.1	Description of the modeling geometry.	62
4.2	Description of the steps taken in extracting \mathbf{S} from fields.	63
4.3	Polar plots of S_{11} and S_{22} on the complex plane—also known as Smith Charts.	64
4.4	Schematic diagram of modal propagation and graphical solution of magnitude and phase conditions on the complex plane.	69
4.5	Test of the scattering matrix description.	72
4.6	Circuit description of a lossless waveguide junction.	74
4.7	Circuit models in the limit where the right waveguide width (b') goes to zero.	80
5.1	Transition from a transmission line to a radiating antenna.	84
5.2	Theoretical radiation patterns of the half-wave dipole antenna.	85
5.3	Geometry of the Mie Theory calculations	88
5.4	Extinction efficiencies of water spheres of three different radii.	92
5.5	Scattering efficiencies of gold spheres of various different radii	93
5.6	Triangulation of a spherical surface using the basis functions developed by Rao, Wilton and Glisson.	95
5.7	Comparison of MoM simulations with the exact Mie calculations.	97
5.8	Method of Moments simulation results and the red shift observed in resonance length.	98
5.9	Yee Lattice used in finite difference frequency domain calculations.	99
5.10	Field teleportation schematic.	103

5.11	Object oriented programming approach.	104
5.12	Top view of the open-sleeve dipole geometry.	108
5.13	Lorentz fit to experimental permittivity values for Au.	110
5.14	Plot of the volumetric field intensity enhancement as a function of wavelength for different polarizations.	111
6.1	Dispersion plot of the optical properties of Au at 850 nm.	115
6.2	FDTD simulation results for a bare dipole antenna on oxide, resonance at 885 nm.	116
6.3	PMMA based Si etch trials.	119
6.4	Successful PMMA based Si etch.	120
6.5	Successful Si etch result using Ma-N resist.	120
6.6	Cross section SEM image of a thick Si line.	121
6.7	Optical microscope image of an early prototype detector.	122
6.8	Bizarre metal dosage problem which led to a dot array instead of a continuous metal film.	123
6.9	Long Si line and the antenna with sleeves on the top.	124
6.10	Optical setup used in the measurements.	125
6.11	Serial electrical connection between the sample, the lock-in and the parameter analyzer through the help of the triax-coax connector box.	126
6.12	Hysteresis in the dark current-voltage plot for a Si photo detector.	129
6.13	Effects of gating on the voltage-current relationship.	131
6.14	Photocurrent as a function of parallel (\parallel) and perpendicular (\perp) polarization.	133
6.15	Efects of contacts on photocurrent characteristics.	134
6.16	Short Si detectors with an antenna (left) and without an antenna (right).	135
6.17	Photo current as a function of light intensity for short Si detectors.	136
6.18	Circular detection element.	137
6.19	Intensity reflection coefficient from an air-oxide-Si three layer system as a function of oxide thickness.	138

સ્વ

“He who lights his taper at mine,
receives light without darkening
me.”

Thomas Jefferson

Chapter 1

Introduction

UNDERSTANDING THE properties of light, and how it interacts with matter has long been studied by various civilizations [2]. First known experiments involved glass spheres filled with water—that was how the lenses were made initially. Near the end of the first millennium, people have understood the way in which light rays bend and focus via lenses and curved mirrors. One of the first optical instruments to gain wide usage was the eyeglass. With the help of convex lenses, longsightedness could be compensated during the 13th century. Concave lenses were harder to make, and usage of spectacles for short-sightedness did not spread until after the 15th century [3].

Then came the telescopes. People were finally able to make precise observations on the heavenly bodies, and that led to a much better understanding of the universe. At one point, telescopes were so popular, that it became fashionable to grind glass to make one's own lenses to build a telescope [3].¹ The development of the microscope also took place during the same period. Biology got a big boost, and many new living organisms were discovered following the invention of the microscope.

As the quality of glass improved and better grinding methods were developed, the resolution of optical instruments advanced. Further improvements came through a better understanding of the properties of light. Newton, among his other achievements in mathematics and physics, showed that white light is composed of different colors. He

¹Similar mass popularization of technology would repeatedly occur following major breakthroughs, as it did after the invention of the transistor when people started playing with electrical circuits, or after the spread of the internet which popularized building home pages.

designed a reflective telescope system, which did not suffer from the focusing problems (chromatic aberrations) of the (refractive) lens systems, which led to his acceptance into the Royal Society.

Although spectacles, telescopes and microscopes helped one see sharper, further and smaller, it was not possible to record images permanently—the image was lost as soon as the optical instrument was moved away. Children—amused by the images in kaleidoscopes²—would have to wait until advances in chemistry led to the invention of photography, and then the motion picture, to throw their kaleidoscopes away, and instead ask to be taken to the cinema.

Principles of photography—one of the first examples of artificial light detection systems—go back to the *camera obscura*, the pinhole camera, which was very popular with painters of the time to practice their skills. When combined with a lens, and a light sensitive photographic film, the modern camera was born from the imaging principles of the camera obscura. In addition to being a technology to record images, photography became a form of art, and further acted as an ‘epistemology engine’ [5].

Eadweard Muybridge’s experiments with photographing galloping of horses—which were commissioned by Leland Stanford—led to the formation of the motion picture: the continuous recording of images in space and time. During the same period, principles of electromagnetism were set on a solid mathematical theory by James Clerk Maxwell—who, by the way, took the first color photograph. The invention and the proliferation of the telegraph, the telephone and then the radio made it possible to send texts, sounds, and images through the use of electrical signals.³ Advances in communication technologies were changing the daily lives of people. A new cultural connectivity was being weaved among the masses by the artists—‘the antennas of race’ according to Ezra Pound [6]—through their work that was being broadcast first by the radio stations and then the television.

As it became possible to send information by electromagnetic signals, the need to

²Let us note in passing that David Brewster (of the Brewster’s angle in polarization optics) was the inventor of the kaleidoscope [4].

³Visit <http://www.archive.org/details/SpotNews1937> for a superb introduction to the wire-photo technology of the 1930s. Many thanks to Zeynep Devrim Gürsel for informing me about this link.

convert the images obtained by optical systems into electricity was born. Photographs were rasterized into lines, each line was converted into an electrical waveform by the use of a photodetector (initially made out of vacuum tubes, and then semiconductor elements), the signal was then transmitted through a cable or through a radio channel and finally the procedure was reversed on the receiving side to reproduce the image remotely.

The advent of television came next. Images and sound could now be transmitted over the air. Millions started watching TV—it became a part of almost every household that could afford to have one. Meanwhile, electronics technology was improving at an unprecedented speed. ‘Smaller, faster, denser’ became the motto of the electronics industry. Increased knowledge in optics was one of the key drivers of such a rapid progress. Optical lithography systems focused images of circuit diagrams onto semiconductors coated with light sensitive films, which then were further processed to fabricate integrated circuits with millions of interacting components, at an affordable price. The word ‘computer’ acquired its current meaning [7]. During the same era, laser was invented and contact lenses entered our lives.

Proliferation of computers increased the demand to automate, and to connect more and more devices together. Research on networking of computers and on automating their connectivity eventually led to the formation of a global computer network, the Internet. This time, though, in contrast to the telegraphy or telephone networks of the previous era, information was being carried by laser light for most of the distances. Fiber optic cables were laid out under the oceans, across the continents: fiber was preferred over electrical cabling because signals could be sent much further, and because of the immense bandwidth of the optical fiber—a single fiber optic cable was sufficient to carry hundreds of thousands of telephone conversations worth of information.

Today, fiber optics form the infrastructure of many communication networks. Optical communications is gaining wide spread usage, especially in areas where high information bandwidth is needed. For instance, today’s high speed routers use fibers to connect their electrical boards together. The limited information carrying capacity of electrical wires, the high energy required to charge and discharge electrical wires while transmitting information at high speeds, synchronization problems due to different

wire lengths and the related increased complexity of design are all leading to a shift to using light for communications rather than electrons [8]. The question of whether or not to use optics for distances shorter than that between electronics boards is becoming more and more relevant. Optical communications at the chip to chip level, and even for intra-chip distances is being actively researched.

If optics is to provide a solution, several problems need to be solved [9]. First of all, there are strict energy requirements: optics should be at least as good, and even better than the corresponding electrical alternatives. As a result, very low capacitance photodetectors, intimately integrated to signal amplifying transistors, are needed to convert the information in light to electrical signals, which can then be processed by the electronics. The current CMOS technology uses transistors of a few tens of nanometers in size, and the size of transistors is projected to shrink further according to the ITRS roadmap.⁴

The size of electronics is much smaller than the wavelength of light (~ 1500 nm for fiber optics communications), whereas most optical components are required to have at least a wavelength of size in order to be functional. The size mismatch between electrical and optical components should be overcome in order to make optical communications viable at shorter distances. Recent interest in the use of metals to design optical components offers a way into designing optics at the subwavelength regime [10]. Properties of metals at optical frequencies enable those designs.

In this dissertation, we will start Chapter 2 by reviewing the optical properties of metals. Then we will describe some of the metallic waveguiding geometries that have been shown to focus light at the length scale of electronics. Of those geometries, the metal-insulator-metal (MIM) geometry is especially interesting as it allows the optical fields to be concentrated in very small volumes. The modal structure of MIM waveguides will be at our focus in Chapter 3. We will describe the necessary mathematical framework to fully analyze MIM waveguide modes, and show the necessity to include different types of modes in order to be fully able to understand scattering within those waveguides.

⁴<http://www.itrs.net/Links/2007ITRS/Home2007.htm>

Chapter 4 will be about our work in developing simple models to predict the response of optical fields in complicated waveguide networks. We will show how to connect different types of MIM waveguides together by providing the details of the design of a mode-converter which is used to focus light coming from a wavelength sized optical mode into one which is much smaller than the wavelength. Furthermore, we will develop exact circuit models for waveguide junctions and investigate their properties.

After having talked about waveguiding geometries, in Chapter 5 we will focus on designing very low capacitance photodetectors. We will use a very small of volume of semiconductor as our detector, and integrate the detector in an antenna geometry in order to increase its sensitivity. We will borrow design topologies from microwave electronics, and show how to apply them at optical frequencies.

Fabrication and measurement results will be the topic of Chapter 6. We will describe in detail our efforts at fabricating Si based antenna integrated photodetectors by electron beam lithography and subsequent clean room processing. We will describe the opto-electronic photocurrent measurement setup we built and provide our experimental results. At the end of Chapter 6 we will compare our results with those published in the nanowire literature and comment on the possible effects which we observed. Lastly, we will lay out our conclusions in Chapter 7.

Chapters 3 and 4 have been published in Physical Review B [11] and in IEEE Journal of Selected Topics in Quantum Electronics [12] respectively.

સુ

Chapter 2

Background Information

IN THIS CHAPTER we will outline some of the background information on optics with metals. We will begin by a review of the optical properties of metals at various frequency ranges via the use of the Lorentz model.

2.1 Permittivity of Metals

The Lorentz model is a simple phenomenological way of describing the optical properties of metals. It assumes the existence of non-interacting, independent oscillators (electrons in the conduction band of a metal in our case) connected to fixed points in space (ions in the lattice) by a spring of stiffness constant k . Let us call the charge of electrons, $-e$, and their mass, m as shown in Figure 2.1. Furthermore, assume that the electron motion is damped by a factor $1/\tau$ where τ is the average time between collisions of the electrons with the lattice. The dynamical motion of electrons is given by

$$m\ddot{\mathbf{r}} + \frac{m}{\tau}\dot{\mathbf{r}} + k\mathbf{r} = -e\mathbf{E}. \quad (2.1)$$

We will use the $e^{+j\omega t}$ convention throughout the remainder of this chapter. In the literature, some prefer to use $e^{-j\omega t}$ and therefore it is important to check the convention in use before quoting a result from another work. The $e^{+j\omega t}$ choice causes the time

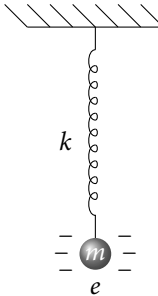


Figure 2.1 – Simple model for the electrons in the Lorentz model.

derivatives to be replaced with $j\omega$ and substitution into (2.1) gives

$$-\omega^2 mr + j\omega \frac{m}{\tau} \mathbf{r} + k\mathbf{r} = -e\mathbf{E}. \quad (2.2)$$

Now it is much easier to solve for the position, \mathbf{r} . We get

$$\mathbf{r} = \frac{(-e/m)\mathbf{E}}{k/m - \omega^2 + j\omega/\tau}. \quad (2.3)$$

In the limit of zero damping, that is as $\tau \rightarrow \infty$, the natural oscillation frequency of the mass-spring system is given by $\omega_0 = \sqrt{k/m}$. That can be seen by setting $\mathbf{E} = 0$ and $\tau = \infty$ in (2.2) and solving for the frequency which would lead to a nonzero position vector, \mathbf{r} .

Whenever a charge moves from its equilibrium position, there is a net induced dipole moment, \mathbf{p} , associated with the motion. For a single particle the dipole moment is described by $\mathbf{p} = -e\mathbf{r}$. In the case of many oscillating dipoles, if one makes the assumption that they all oscillate coherently, the total dipole moment density, \mathbf{P} , of the system is $\mathbf{P} = n\mathbf{p} = -en\mathbf{r}$ where n is the density of electrons in the lattice. Substituting the definition of \mathbf{r} from (2.3) results in

$$\mathbf{P} = \frac{(ne^2/m)\mathbf{E}}{\omega_0^2 - \omega^2 + j\omega/\tau}. \quad (2.4)$$

At this stage, it is worthwhile to investigate the oscillation frequency of a collection of charged particles of density, n , when they are displaced from their equilibrium position

by an applied electric field, E . As shown in Figure 2.2, before the application of the external field, positively charged ions and the negatively charged electrons are at an equilibrium under the influence of the Coulomb forces among them. Application of an external electric field, on the other hand, changes the equilibrium condition. Electrons move in the direction opposite to the applied field until the net force on them, which is the force due to the external field and the Coulomb attraction force from positive ions, is zero. Now, assume that the external field, E , is turned off. There is a net force on the electrons due to their separation from the ions. Under the assumption of zero damping, electrons will oscillate back and forth around their initial equilibrium state. The question is, what will be their oscillation frequency?

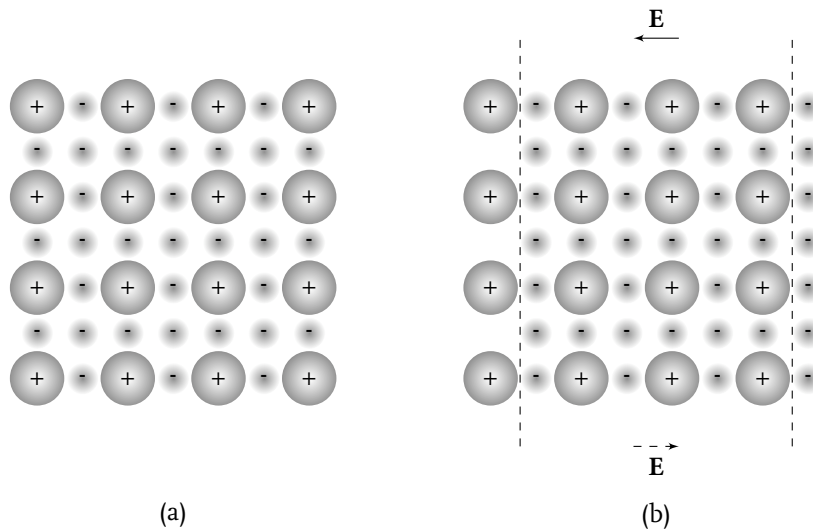


Figure 2.2 – Distribution of positively charged ions and negatively charged electrons before (a) and after (b) the application of electric field, E . Dashed arrow shows the induced field due to the movement of electrons from their equilibrium state in (a).

A typical example from electrostatics is the calculation of the electric field in between the plates of a parallel plate capacitor. The idea is to use the Gauss' Law, $\nabla \cdot \mathbf{D} = \rho$, to integrate the charge density, ρ , over a volume defined by an infinitesimally small pillbox shape which crosses both the metal and the air regions of the capacitor. Conversion of the volume integral into a surface one and noting that the field inside a metal is zero leads to the solution $\mathbf{D}_\perp = \rho$ for the normal component of the displacement field. Here,

we will make an analogy to the parallel plate case. As illustrated by the vertical dashed lines in Figure 2.2(b), separation of positive and negative charges can be modeled as an effective capacitor with a displacement vector $\mathbf{D} = \mathbf{D}_\perp = \rho = ne\mathbf{r}$. Here, \mathbf{r} is the displacement of electrons from their equilibrium position in Figure 2.2(a). Given the displacement, the electric field is $\mathbf{E} = \mathbf{D}/\epsilon_0 = (ne/\epsilon_0)\mathbf{r}$. The net force on an electron of mass m is therefore, $\mathbf{F} = m\ddot{\mathbf{r}} = -e\mathbf{E}$. Using the $e^{+j\omega t}$ convention to change the time derivatives to $j\omega$ results in

$$-m\omega^2\mathbf{r} = \frac{-ne^2}{\epsilon_0}\mathbf{r}.$$

For a nontrivial solution ($\mathbf{r} \neq 0$) to exist, the plasma oscillation frequency, which we denote by ω_p should be

$$\omega_p^2 = \frac{ne^2}{m\epsilon_0}.$$

Using the definition of ω_p^2 in (2.4) and from the definition of the displacement vector $\mathbf{D} = \epsilon_0\mathbf{E} + \mathbf{P}$, one gets the following for the relative permittivity ϵ_r

$$\begin{aligned} \mathbf{D} &= \epsilon_0\mathbf{E} + \mathbf{P} = \epsilon\mathbf{E} \\ \epsilon_r &\equiv \frac{\epsilon}{\epsilon_0} = 1 + \chi = 1 + \frac{\mathbf{P}}{\epsilon_0\mathbf{E}} \\ \epsilon_r &= 1 + \frac{\omega_p^2}{\omega_o^2 - \omega^2 + j\omega/\tau}. \end{aligned} \tag{2.5}$$

Equation (2.5) is the Lorentz model for permittivity. Electrons in the conduction band of metals act in a slightly simplified form. Because they are assumed to be free, there are no springs that tie them to the positively charged ions. Hence $\omega_o \rightarrow 0$ in the case of metals. By neglecting ω_o we get the Drude model for permittivity as

$$\epsilon_m = 1 + \frac{\omega_p^2}{-\omega^2 + j\omega/\tau}. \tag{2.6}$$

Note that at different frequency regimes, electrons behave differently. There are

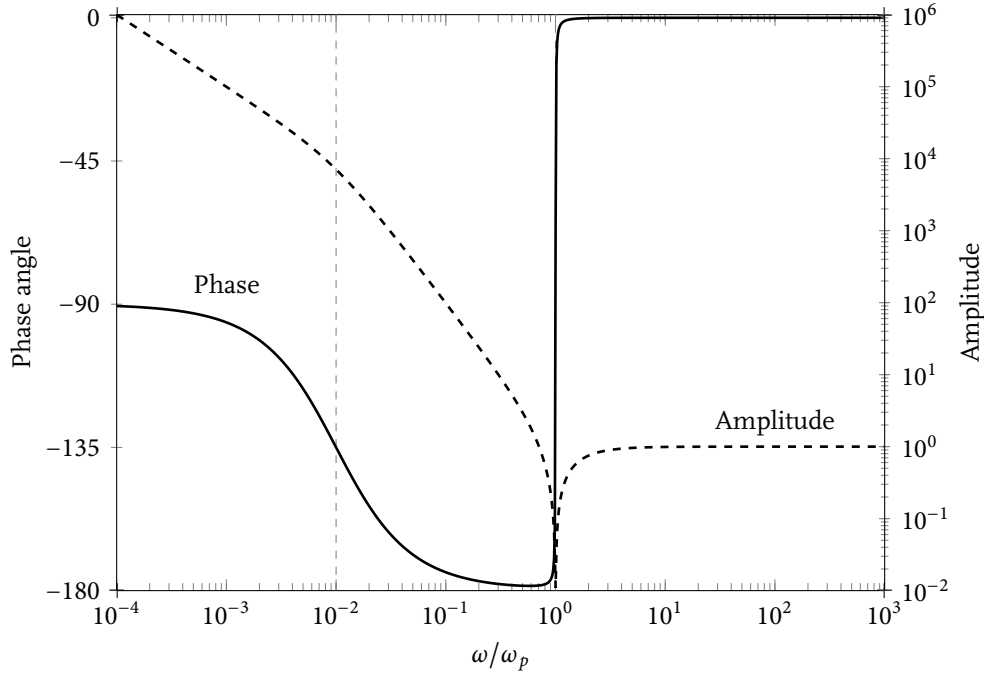


Figure 2.3 – Phase and amplitude of the permittivity for a Drude metal with $\delta = 1/\tau = 0.01\omega_p$. For $\omega < \delta$, the permittivity is a predominantly imaginary number, for $\delta < \omega < \omega_p$ it is close to being a negative real number and for $\omega > \omega_p$ the sudden phase change shows that the permittivity becomes a positive real quantity, with a magnitude close to unity.

three regimes of interest, $\omega < 1/\tau$, $1/\tau < \omega < \omega_p$ and $\omega > \omega_p$. Let's now analyze the properties of the Drude metal at these different frequency regimes.

2.1.1 Microwave Regime

In this part of the spectrum, $\omega < 1/\tau$, the driving field frequency is lower than the frequency of particle collisions. Therefore in each ‘optical’ cycle electrons go through multiple collisions as they are being accelerated by the applied field. This is the regime where electron movement is a drift motion and hence the velocity of electrons is proportional to the applied field. Simplification of the terms in (2.6) gives

$$\epsilon_m \approx \frac{\omega_p^2}{j\omega/\tau} = -j \frac{ne^2\tau}{m\epsilon_0\omega}. \quad (2.7)$$

The proportionality between velocity and the applied field can explain why the permittivity is a negative imaginary number. Firstly, because electrons have a negative charge $\mathbf{v} \propto -\mathbf{E}$. From the definition of velocity we also have $\mathbf{v} = \dot{\mathbf{r}} = j\omega\mathbf{r}$. Therefore, $\mathbf{r} \propto j\mathbf{E}$. However, since dipole moment density $\mathbf{P} = n\mathbf{p} = -en\mathbf{r}$ we have $\mathbf{P} \propto -j\mathbf{E}$. Since $\epsilon_r = 1 + \mathbf{P}/\epsilon_0\mathbf{E}$, for $|\mathbf{P}/\epsilon_0\mathbf{E}| \gg 1$, the permittivity is a large negative imaginary number. It is important to note that if the time derivatives were to be changed to $-j\omega$ due to a choice of the $e^{-j\omega t}$ convention, one would get a large, positive imaginary number for the permittivity.

For metals with a high conductivity, it is possible to lump conductivity into permittivity. From Maxwell's equations, we have $\nabla \times \mathbf{H} = \mathbf{J} + \partial_t \mathbf{D} = \sigma\mathbf{E} + j\omega\epsilon_0\mathbf{E} = j\omega\epsilon_0(1 - j\sigma/\omega\epsilon_0)\mathbf{E}$ where σ is the DC conductivity of the metal. If the DC conductivity is a large number then $\epsilon_m \approx -j\sigma/\omega\epsilon_0$ just like as in (2.7).

2.1.2 Infrared Regime

In this part of the spectrum, $1/\tau < \omega < \omega_p$, electrons can follow the driving field and they go through a negligible number of scattering events per optical cycle. The force on the electrons, and therefore their acceleration is proportional to the applied field. Let us try to guess what the sign of permittivity will be in this regime. We have $\mathbf{a} = \ddot{\mathbf{r}} \propto -\mathbf{E}$. The usual trick of converting time derivatives into $j\omega$ results in, $\mathbf{r} \propto \mathbf{E}$. Again, from the definition of dipole moment density, $\mathbf{P} \propto -\mathbf{E}$. Also for the case $1/\tau < \omega < \omega_p$ it is still true that $|\mathbf{P}/\epsilon_0\mathbf{E}| \gg 1$ and therefore permittivity is a negative real number. Of course, that can also be seen by neglecting the $1/\tau$ term in (2.6) to get

$$\epsilon_m \approx -\frac{\omega_p^2}{\omega^2}. \quad (2.8)$$

2.1.3 Ultraviolet Regime

In this regime, where $\omega > \omega_p$, individual electrons can still follow the field. Therefore $\mathbf{P} \propto -\mathbf{E}$ still holds. However, as the frequency increases, the polarizability of electrons decreases. Therefore, interaction between the driving field and the electrons decreases

as the frequency of operation increases. Above and near the plasma oscillation frequency $|P/\epsilon_0 E| \gg 1$ no longer holds. As a result, the full form for the definition of the relative permittivity, $\epsilon_r = 1 + P/\epsilon_0 E$, must be used. Because the strength of polarization is so small in this regime, permittivity becomes a positive real number and is described as

$$\epsilon_m \approx 1 - \frac{\omega_p^2}{\omega^2}.$$

Experiments have shown that time between collisions, τ , for Au and Ag is on the order of 30 fs [13]. Furthermore, the plasma oscillation frequency, ω_p , for Au is about 6×10^{15} rad/sec which translates into a free space wavelength, λ_p , of 300 nm [14]. If one defines the collision frequency as $\delta \equiv 1/\tau$, for a typical metal $0.01\omega_p < \delta < 0.1\omega_p$. In Figure 2.3 we show the phase and amplitude of the permittivity for a Drude metal with $\delta = 0.01\omega_p$.

2.2 Surface Impedance of Metals

So far, we analyzed the permittivity of metals at different frequency regimes. In this section, we will take a closer look at the way in which electromagnetic waves propagate in a homogeneous metallic medium with a permittivity ϵ_m .

The space-time dependence of plane waves in homogeneous media is given by $\exp(j\omega t - jkz)$ where k is the wave-vector associated with the field.¹ We know that $k = \omega\sqrt{\epsilon_m}/c$ where c refers to the speed of light in vacuum. The refractive index associated with metals, $n \equiv \sqrt{\epsilon_m}$, is a complex number. In order to have plane waves that decay as $z \rightarrow \infty$ we will choose $n = n' - jn''$ where n' and n'' are both non-negative real quantities and they represent the real and imaginary parts of the refractive index. Substituting the refractive index and rearranging terms gives us plane waves that propagate as $\exp(j\omega(t - n'z/c)) \exp(-n''\omega z/c)$. The second exponential term leads to the decay of the plane waves. The skin depth, κ , for fields is defined as the distance at which the

¹From now on, k will be used to represent the wave vectors—not the stiffness coefficient of springs used in the Lorentz model.

fields decay to $1/e$ of their peak value. We have $\kappa = \lambda/(2\pi n'')$.

In calculations involving the scattering of waves from metallic objects, under certain conditions it becomes possible to neglect the fields within the metallic objects and treat the scattering through the use of approximate boundary conditions. For those cases when $\kappa \ll \lambda$ and $\kappa \ll$ radius of curvature of the metal surface, the derivatives of the field components inside the metal along the normal to the surface are large compared to the tangential derivatives [15]. Therefore, the tangential fields will have a longer span in the metal than the normal components—similar to the case of plane waves propagating in a lossy medium. The field inside the metal near the surface can thus be regarded as the field of a plane wave and the tangential electric and magnetic fields can be related by

$$\mathbf{E}_t = \sqrt{\frac{\mu}{\epsilon}} \hat{n} \times \mathbf{H}_t \quad (2.9)$$

where \hat{n} is the unit vector along the outer normal to the surface. The problem of determining external electromagnetic fields can be solved without considering the fields inside the metal by the use of the boundary condition (2.9).

The surface impedance, ζ , with units of ohms (Ω), is defined for a non-magnetic material as

$$\zeta = \sqrt{\frac{\mu_0}{\epsilon}} = \frac{1}{n' - j n''} \sqrt{\frac{\mu_0}{\epsilon_0}} \approx \frac{377\Omega}{n' - j n''} = \frac{n' + j n''}{n'^2 + n''^2} 377\Omega = \zeta' + j \zeta''.$$

Since the imaginary part of the refractive index is always negative in the $e^{+j\omega t}$ convention (otherwise fields would exponentially grow, an unphysical scenario for inactive media), the imaginary part of surface impedance, ζ'' , is necessarily positive. From the definition of inductance we know that

$$V = L \frac{dI}{dt} \xrightarrow{\text{Time Harmonic Fields}} V = (+j\omega L)I.$$

Hence, a positive imaginary part can be associated with an effective inductance. From the approximation to the permittivity at infrared frequencies one can get the inductance of a metal surface as

$$L = \frac{\zeta''}{\omega} = \frac{n''/\omega}{n'^2 + n''^2} 377\Omega.$$

At infrared frequencies $\sqrt{\epsilon_m}$ is almost purely imaginary as can be seen from (2.8) and as a result $n' \approx 0$. Therefore, we can estimate the surface inductance using $n'' = \sqrt{-\epsilon_m} = \omega_p/\omega$ to be

$$L = \frac{377\Omega}{n''\omega} = \sqrt{\frac{\mu_0}{\epsilon_0}} \frac{1}{\omega_p} = \sqrt{\frac{\mu_0}{\epsilon_0}} \sqrt{\frac{m\epsilon_0}{ne^2}} = \sqrt{\frac{\mu_0 m}{ne^2}}.$$

The Lorentz model predicts a constant surface inductance. Therefore, the surface impedance is predominantly imaginary, and is linearly proportional to frequency, i.e. $\zeta = j\zeta'' = j\omega L$. We plot the surface impedance of gold as a function of frequency in Figure 2.4 using the experimental values of permittivity for gold [16]. The slope of the imaginary part of the impedance curve with respect to frequency is a constant over the infrared regime, as expected from the prediction of the Lorentz model.

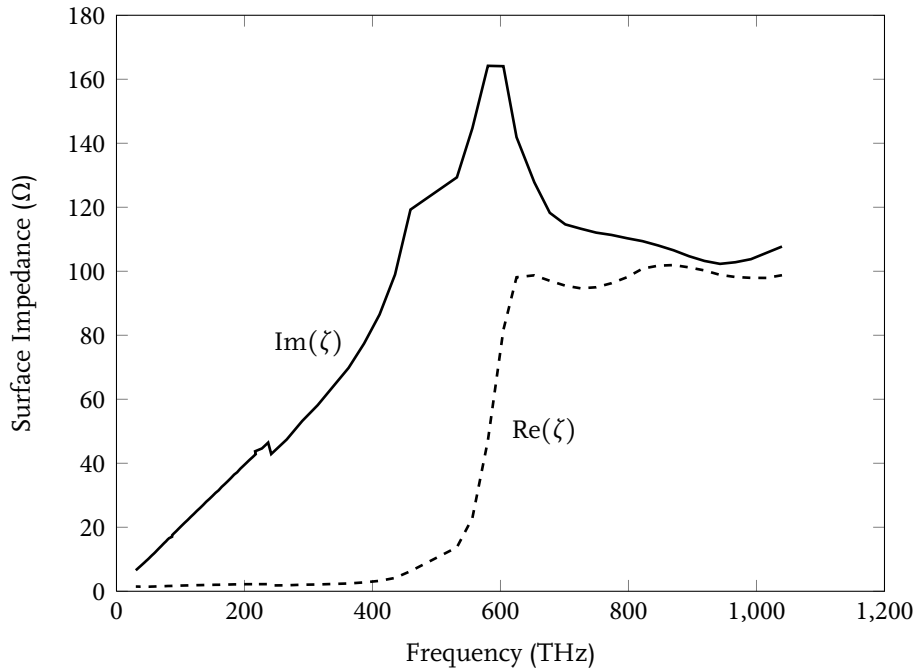


Figure 2.4 – Real and imaginary parts of the surface impedance for Au.

2.3 Metal - Insulator Waveguides

After analyzing the optical properties of metals at different frequency regimes, now is the time to investigate the basic properties of waveguides that use metals to confine light. The first structure that will be investigated is the metal-insulator (MI) waveguide. This is the simplest waveguide one can think of. Its properties were investigated in [17]. The structure is as shown in Figure 2.5.

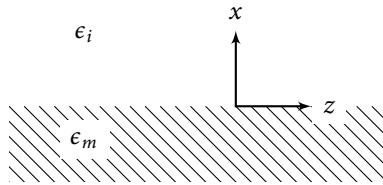


Figure 2.5 – Geometry of the surface plasmon.

In order to have a guided mode, fields should decay exponentially into the metal and insulator regions. We will assume that the mode is TM, i.e. $H_z = 0$. Due to the exponential decay of the mode from the metal-insulator boundary and the continuous nature of parallel component of electric fields, E_z should be of the form

$$E_z = E_{zo} e^{j\omega t - jkz} \begin{cases} e^{\kappa_m x} & x < 0 \\ e^{-\kappa_i x} & x > 0. \end{cases} \quad (2.10)$$

Using the vector identity $\nabla \times (\nabla \times \mathbf{A}) = \nabla(\nabla \cdot \mathbf{A}) - \nabla^2 \mathbf{A}$ and Maxwell's equations, one can write down the wave equation for the electric and magnetic fields as

$$\begin{aligned} \nabla^2 \mathbf{E} + \omega^2 \mu \epsilon \mathbf{E} &= 0 \\ \nabla^2 \mathbf{H} + \omega^2 \mu \epsilon \mathbf{H} &= 0. \end{aligned} \quad (2.11)$$

Given the assumed form for E_z in (2.10), substitution into (2.11) results in $\kappa_{m,i}^2 = k^2 - \omega^2 \mu \epsilon_0 \epsilon_{m,i}$. Using (A.5) one can get the expression for the transverse magnetic field

component as

$$H_y = j \omega \epsilon_o E_{zo} e^{j \omega t - j k z} \begin{cases} \frac{\epsilon_m \kappa_m}{k^2 - \omega^2 \mu \epsilon_o \epsilon_m} e^{\kappa_m x} & x < 0 \\ \frac{-\epsilon_i \kappa_i}{k^2 - \omega^2 \mu \epsilon_o \epsilon_i} e^{-\kappa_i x} & x > 0. \end{cases}$$

From the definition of $\kappa_{m,i}$ factors in the definition of H_y can be further simplified to get

$$H_y = j \omega \epsilon_o E_{zo} e^{j \omega t - j k z} \begin{cases} \frac{\epsilon_m}{\kappa_m} e^{\kappa_m x} & x < 0 \\ \frac{-\epsilon_i}{\kappa_i} e^{-\kappa_i x} & x > 0. \end{cases} \quad (2.12)$$

Tangential components of \mathbf{H} should be continuous. From the expression in (2.12), continuity of H_y results in $\kappa_m/\epsilon_m = -\kappa_i/\epsilon_i$. This is the dispersion equation for the MI system. It relates the wave vector k to angular frequency ω . From the definition of $\kappa_{m,i}^2$, one can get the following equation for k

$$k^2 = \frac{\omega^2}{c^2} \frac{\epsilon_i \epsilon_m}{\epsilon_i + \epsilon_m}$$

where c is the speed of light in vacuum. Here ϵ_m is the relative permittivity of the metal as given in (2.6). We can see that, at low frequencies where $|\epsilon_m| \gg 1$, $k \approx \omega/c$. Also, when $\epsilon_m \approx -\epsilon_i$, k will take its maximum value. Assuming that the insulator side is air and neglecting the imaginary part of ϵ_m to get $\epsilon_m \approx 1 - (\omega_p/\omega)^2$, the condition $\epsilon_m \approx -1$ will be true when $\omega \approx 1/\sqrt{2} \omega_p$. In Figure 2.6 we plot the real and imaginary parts of k for a Drude metal with $\delta = 1/\tau = 0.05\omega_p$.

It is worthwhile to investigate the properties of the mode of the MI waveguide, which is also sometimes called surface plasmon (SP), as the frequency of operation varies. In that respect, we plotted the skin depth of the fields into the insulator and the metal regions for a surface plasmon in Figure 2.7. As can be seen from the figure, the mode becomes unbounded at low frequencies. Around the surface plasmon frequency of $\omega \approx 1/\sqrt{2} \omega_p$, the mode gets tightly confined to the surface after which it begins to

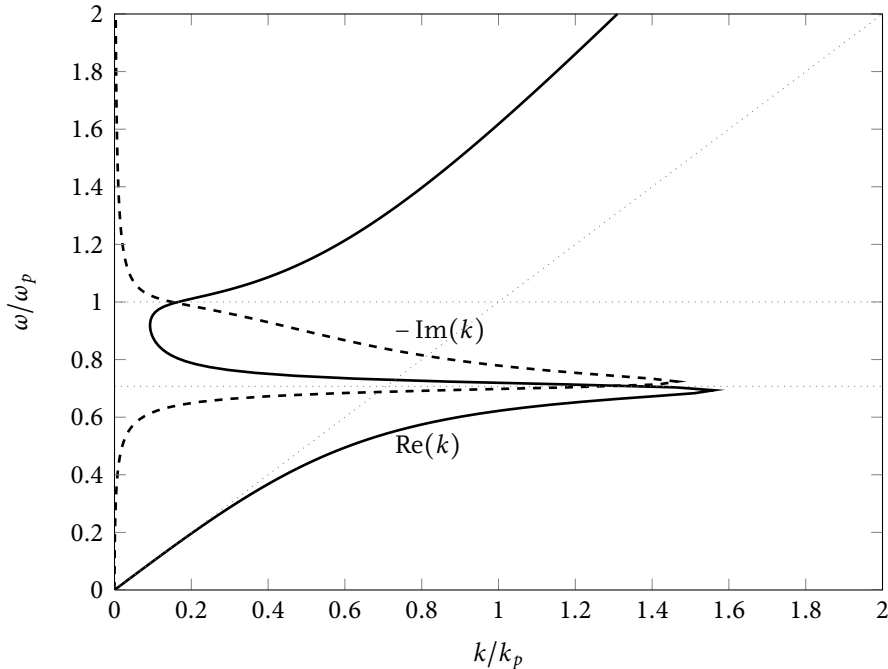


Figure 2.6 – Normalized $\omega - k$ diagram for an MI waveguide with $\delta = 1/\tau = 0.05\omega_p$. Dashed line is the negative of the imaginary part of k whereas the solid line is the real part. $k_p = \omega_p/c$. Dotted lines show $\omega = k$, $\omega = 1$ and $\omega = 1/\sqrt{2}$.

widen again. The skin depth for a plane wave hitting a metal surface is also plotted for comparison. The same information is also visualized in a density plot by Figure 2.8 where the field intensity is plotted with respect to frequency.

2.4 Metal - Insulator - Metal Waveguides

After having analyzed the MI waveguide, the next step will be to investigate the light guiding properties of the MIM configuration. Similar to the case for the MI waveguide, we will look at the TM modes of the system. Guided modes should decay as they get further apart from the wave guiding region of the system. Therefore, in general the field pattern for the longitudinal electric field is of the form

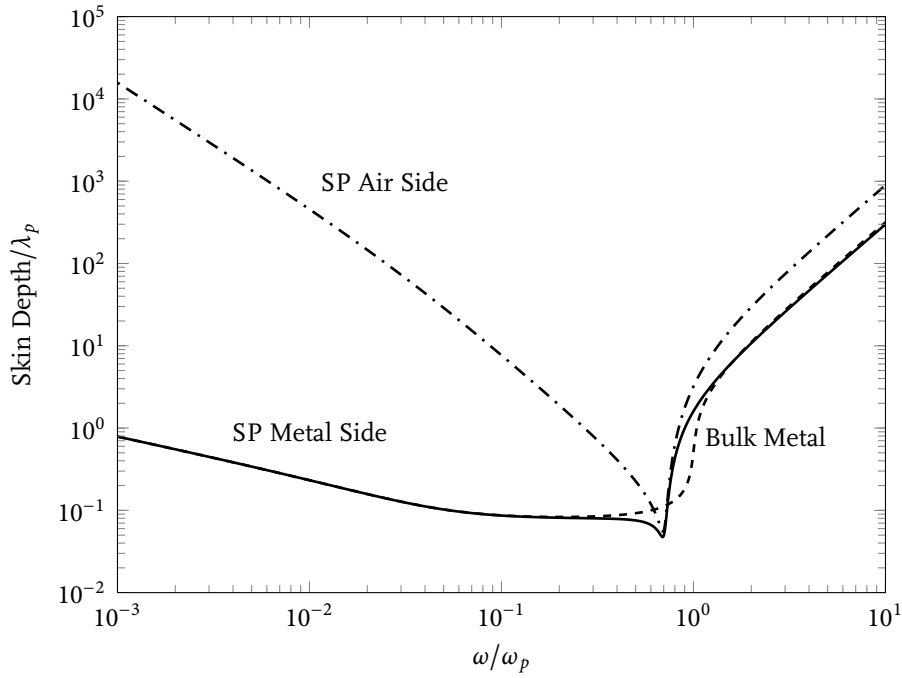


Figure 2.7 – Skin depth vs ω for the surface plasmon mode and the bulk metal for $\delta = 1/\tau = 0.05\omega_p$. $\lambda_p = 2\pi c/\omega_p$.

$$E_z = E_{zo} e^{j\omega t - jkz} \begin{cases} A_I e^{\kappa_m x} & x < 0 \\ A_{II} e^{\kappa_i x} + A_{III} e^{-\kappa_i x} & 0 < x < d \\ A_{IV} e^{-\kappa_m x} & x > d. \end{cases}$$

In order to find the transverse magnetic field, one can use (A.5) to get

$$H_y = j\omega\epsilon_0 E_{zo} e^{j\omega t - jkz} \begin{cases} \frac{\epsilon_m}{\kappa_m} A_I e^{\kappa_m x} & x < 0 \\ \frac{\epsilon_i}{\kappa_i} (A_{II} e^{\kappa_i x} - A_{III} e^{-\kappa_i x}) & 0 < x < d \\ \frac{-\epsilon_m}{\kappa_m} A_{IV} e^{-\kappa_m x} & x > d. \end{cases}$$

As can be seen, there are four unknowns: $A_I, A_{II}, A_{III}, A_{IV}$. Continuity of E_z and H_y at $x = 0$ and $x = d$ results in 4 homogeneous equations in terms of the 4 unknowns. The dispersion equation for the MIM case comes from the condition which makes the system of 4 homogeneous linear equations linearly dependent so that fields have finite

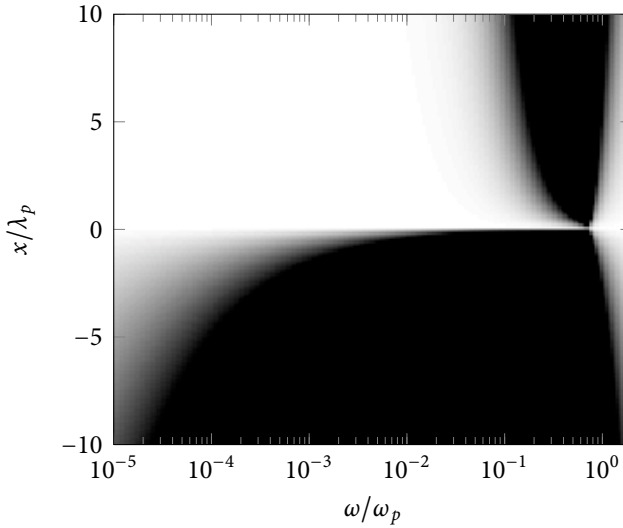


Figure 2.8 – Mode profile for an MI waveguide with $\delta = 0.05\omega_p$. $x < 0$ region is the metal, $x > 0$ is the insulator (air). $\lambda_p = 2\pi c/\omega_p$.

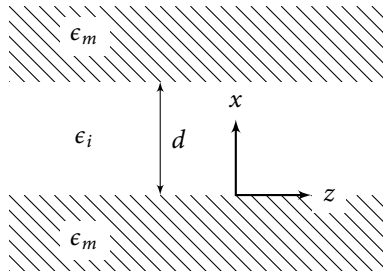


Figure 2.9 – Geometry of the metal-insulator-metal (MIM) parallel plate waveguide.

solutions as opposed to the trivial $A_i = 0$ case where $i \in \{1, \dots, 4\}$. After some algebra, it is not too difficult to obtain the dispersion relation

$$\left(\frac{1-R}{1+R}\right)^2 = e^{-2\kappa_i d} \quad \text{where } R = -\frac{\kappa_m/\epsilon_m}{\kappa_i/\epsilon_i} \text{ and } \kappa_{m,i}^2 = k^2 - \omega^2 \mu \epsilon_0 \epsilon_{m,i}. \quad (2.13)$$

Taking the square root of (2.13) results in $(1-R)/(1+R) = \pm e^{-\kappa_i d}$. Arranging terms

and substituting the definition of R gives the following two equations:

$$\begin{aligned}\frac{\epsilon_m}{\epsilon_i} \tanh\left(\frac{\kappa_i d}{2}\right) + \frac{\kappa_m}{\kappa_i} &= 0 \quad \text{and} \\ \frac{\epsilon_m}{\epsilon_i} \coth\left(\frac{\kappa_i d}{2}\right) + \frac{\kappa_m}{\kappa_i} &= 0.\end{aligned}$$

It should be emphasized that, what we have done so far is no different than the formulation for dielectric slab waveguides. We have simply redefined the slab region to be the insulator covered with metal on the sides. Also note that, because ϵ_m is a complex number, solution of the dispersion equations requires a two dimensional search over the complex plane. That is not a simple task if one is interested in finding roots at different frequency regimes for different insulator thicknesses.

This section gave only a cursory look at the modal structure of the MIM waveguide, and focused only on the main mode of the system. As we will show in the next chapter, there are other modes, which will be of particular importance when analyzing networks of MIM waveguides.

ફૂ

Chapter 3

Metal–Insulator–Metal Modes

3.1 Introduction¹

WAVEGUIDES HAVE LONG been used to controllably direct energy flow between different points in space. Understanding the way waves propagate in waveguides led to a multitude of creative designs—all the way from the pipe organ to light switches used in fiber optic communications. In optics, recently there has been a growing interest in making use of the dielectric properties of metals to guide electromagnetic energy by using sub-wavelength sized designs that work in the infrared and the visible bands of the spectrum. One of the motivations for doing photonic research using metals is to find the means to integrate electronic devices with sizes of tens of nanometers with the relatively much larger optical components—so that some of the electrons used in the communication channels between electrical circuitry can be replaced by photons for faster and cooler operation [10].

Whereas the use of metals for directing electromagnetic energy is relatively new in optics, sub-wavelength guiding of light by metals is the norm in the microwave domain. Even though the permittivity of metals can be large in magnitude at both microwave and optical frequencies, the characteristics of the permittivity are quite different in the two frequency regimes.

In the microwave regime, electrons go through multiple collisions with the ions of

¹This chapter is taken from [11]. Copyright 2009 by the American Physical Society.

the lattice during an electromagnetic cycle according to the phenomenological Drude model of electrons. Therefore, the electron movement is a drift motion where the *velocity* of electrons is proportional to the applied field strength [18, Ch. 1]. As a result, the induced dipole moment density and hence the permittivity is a large, negative² imaginary number. On the other hand, at optical frequencies below the plasma oscillation frequency, electrons go through a negligible number of collisions during an electromagnetic cycle and this time *acceleration* of electrons is proportional to the applied field strength which then results in a permittivity that can be substantially a large real negative number. Above the plasma frequency, the induced dipole moment density is very low and the permittivity is predominantly a positive real number less than one [14, Ch. 9].

The dielectric slab and the parallel plate (i.e. consisting of two parallel perfectly conducting metal plates) waveguides are the two canonical examples of waveguiding theory. If we have a layered *metal-insulator-metal* (MIM) geometry, it is possible to smoothly transition from the dielectric slab to the parallel plate waveguide by reducing the frequency of operation, and therefore varying the metallic permittivity ϵ_m .

At frequencies above the plasma frequency, the metal has a permittivity $\epsilon_m < 1$ whereas the insulator has $\epsilon_i \geq 1$. We illustrate the geometry in the inset of Figure 3.1.

The physical modes that the dielectric slab waveguide supports fall into two sets: guided modes and radiation modes [19, Ch. 1]. Guided modes consist of a countable, finite set, i.e. there is only a finite number of discrete guided modes. Radiation modes consist of a non-countable, infinite set, i.e. they form a continuum. The combination of these two sets of modes form a complete and orthogonal basis set.

Now suppose that we change our operation frequency to one which is very close to the DC limit where ϵ_m is an arbitrarily large, negative, imaginary number. In this limit, we can approximate the metal as a *perfect electric conductor* (PEC) where $|\epsilon_m| \rightarrow \infty$. Such an approximation then gives us the parallel plate waveguide of the microwave domain. Unlike the dielectric slab, the parallel plate geometry is bounded in the transverse dimension—fields are not allowed to penetrate into the PEC. There are infinitely many

²Here, we are assuming that the fields are time harmonic with $\exp(+i\omega t)$ time dependence. For $\exp(-i\omega t)$ time dependence, we get a positive imaginary value for the permittivity.

discrete modes of the parallel plate, all of which have sinusoidal shapes, and there are no continuum modes. The collection of the infinitely many discrete modes forms a complete orthogonal basis set.

In this chapter we will investigate the modal structure of the two dimensional MIM waveguide in the infrared regime where ϵ_m is primarily a large, negative real number. The geometry of the MIM waveguide is exactly the same as the one in the inset of Figure 3.1. The only difference between the parallel plate, MIM and the dielectric slab waveguides is in the numerical value of ϵ_m , which depends on the frequency of operation.

There have been numerous studies of the MIM waveguide in the literature [17, 20–36]. The fact that light can be guided within a deep subwavelength volume over a very wide range of wavelengths is one of the primary reasons why the MIM geometry has attracted so much attention. The full set of modes that the MIM waveguide supports—real and complex discrete modes as well as a continuous set of modes—has only very recently been published [36]. For other geometries, it has been shown that, in general, waveguides support real, complex and continuous sets of modes [37–41]. In this work, we will provide the detailed mathematical framework to analyze the modal structure of the MIM waveguide and emphasize how it is a hybrid between the parallel plate and the dielectric slab waveguides.

Operator theory will be the basis of the mathematical tool set with which we will analyze MIM waveguides. In Section 3.2, we will introduce the notation and make some definitions pertaining to the operators in infinite dimensional spaces. In Section 3.3 we will derive the discrete and continuum modes supported by the MIM waveguide and show that the underlying operators are pseudo-Hermitian. In Section 3.4 we will demonstrate that the modes we report form a complete basis set via example calculations using the mode-matching technique. In Section 3.5 we will discuss our results and underline some of the relevant developments in mathematics from both quantum mechanics and microwave theory with the hope of expanding our tools of analysis. Lastly, in Section 3.6 we will draw our conclusions.

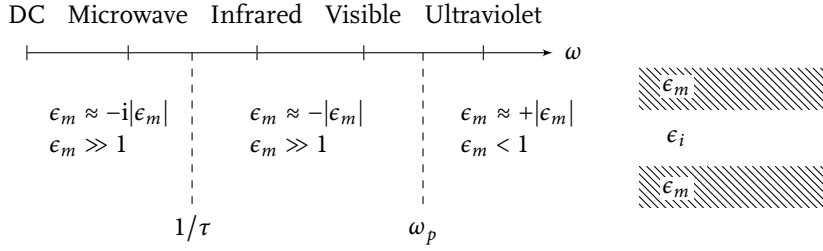


Figure 3.1 – The change in the metallic permittivity (ϵ_m) as the frequency of operation (ω) is varied leads to an evolution from the parallel plate waveguide at low frequencies to the dielectric slab waveguide at high frequencies for the two dimensional metal-insulator-metal geometry. We are assuming that ϵ_m is a Drude model metal where τ is the average time between collisions among the ions of the lattice and the free electrons, ω_p is the plasma oscillation frequency.

3.2 Some Definitions

Throughout the chapter, we will be using nomenclature from operator theory. In this section, we will define the terminology and introduce the notation which will be used in the following sections.³ The reader well versed in operator theory can directly skip to the next section.

A *linear vector space* is a space which is closed under the operations of addition and of multiplication by a scalar. We will call the elements of the space *vectors*. Spaces need not be finite dimensional—*infinite dimensional vector spaces* are also possible. For instance, the collection of all square integrable functions $f(x)$ defined on an interval $a < x < b$ forms an infinite dimensional vector space.

The *inner product* is a scalar valued function of two vectors f and g , written $\langle f | g \rangle$ with the following properties

$$\begin{aligned}\langle f | g \rangle &= \langle g | f \rangle^* \\ \langle \alpha_1 f + \alpha_2 g | h \rangle &= \alpha_1^* \langle f | h \rangle + \alpha_2^* \langle g | h \rangle \\ \langle f | f \rangle &> 0 \quad \text{if } f \neq 0.\end{aligned}$$

Here $(\cdot)^*$ denotes complex conjugation, $\alpha_{\{1,2\}}$ are arbitrary complex numbers and f, g ,

³For a more detailed coverage on vector spaces and operators, we refer the reader to [42–46]. We will use *italic* letters for scalar variables, **bold** letters for vector variables, sans-serif letters for operators and **SERIFPT** style for linear spaces

h denote arbitrary members of the linear vector space \mathcal{S} .

For the infinite dimensional vector space of square integrable functions one possible definition of the inner product is

$$\langle f|g \rangle = \int_a^b f^*(x)g(x) dx. \quad (3.1)$$

A linear vector space with an inner product is called an *inner product space*. In such spaces the *norm of a vector* f is defined as

$$\|f\| = \sqrt{\langle f|f \rangle}. \quad (3.2)$$

This is also known as the L^2 norm, to denote square integrability in the sense of Lebesgue. By using the norm of a vector space, we can define the distance between its vectors f and g as $d(f, g) = \|f - g\|$ which is always nonzero if $f \neq g$. Here, $d(f, g)$ is called the *metric*—the measure of distance between vectors—of the inner product space. Suppose that \mathcal{F} and \mathcal{G} are two subsets of the inner product space \mathcal{S} and that \mathcal{F} is also a subset of \mathcal{G} , i.e. $\mathcal{F} \subset \mathcal{G} \subset \mathcal{S}$. \mathcal{F} is said to be *dense* in \mathcal{G} , if for each $g \in \mathcal{G}$ and $\varepsilon > 0$, there exists an element $f \in \mathcal{F}$ where $d(f, g) < \varepsilon$ [45, pp. 94–95].

A vector space \mathcal{S} is *complete* if all converging sequences of vectors $f_n(x)$ converge to an element $f \in \mathcal{S}$. An inner product space which is complete when using the norm defined by (3.1)-(3.2) is called a *Hilbert space*.

An *operator* L is a mapping that assigns to a vector f in a linear vector space \mathcal{S}_1 another vector in a different vector space \mathcal{S}_2 which we denote by Lf (most often $\mathcal{S}_1 = \mathcal{S}_2$). An operator is *linear* if $L(\alpha_1 f + \alpha_2 g) = \alpha_1 Lf + \alpha_2 Lg$ for arbitrary scalars $\alpha_{\{1,2\}}$ and vectors f, g . The *domain* of an operator L is the set of vectors f for which the mapping Lf is defined. The *range* of an operator L is the set of vectors $g = Lf$ for all possible values of f in the domain of L . A linear operator is *bounded* if its domain is the entire linear space \mathcal{S} of vectors f and if there exists a single constant C such that $\|Lf\| < C\|f\|$. Otherwise the operator is *unbounded*. The differential operator is a classical example of an unbounded operator [44, pp. 93–94]. L is *positive (negative) definite* if $\langle f|Lf \rangle > 0$ ($\langle f|Lf \rangle < 0$) for all possible f . Otherwise, L is *indefinite*.

A linear bounded operator L^\dagger is said to be the *adjoint* of L if, for all f and g in \mathcal{S} the condition $\langle g|Lf \rangle = \langle L^\dagger g|f \rangle$ is satisfied. If $L = L^\dagger$ then L is said to be *self-adjoint*. If the operator L is unbounded, then the equality $\langle g|Lf \rangle = \langle L^\dagger g|f \rangle$ defines a *formal self-adjoint* [45, Sec. 3.4.1].

Suppose we have a set of orthonormal vectors $\{f_n\}$ which span the Hilbert space \mathcal{H} . Then, we can expand any vector $g \in \mathcal{H}$ as $g = \sum_n \langle f_n | g \rangle f_n$. Similarly, any linear bounded operator L acting on g results in

$$\begin{aligned} Lg &= \sum_n \langle f_n | g \rangle Lf_n = \sum_{n,m} \langle f_n | g \rangle \langle f_m | Lf_n \rangle f_m \\ &= \sum_{m,n} f_m \langle f_m | Lf_n \rangle \langle f_n | g \rangle \end{aligned}$$

where we expanded Lf_n in terms of the basis $\{f_m\}$ to get to the last line. Once we choose a complete orthonormal basis set, we can describe the action of L on any vector g by the product of an infinite dimensional matrix with elements $\langle f_m | Lf_n \rangle$ and an infinite dimensional vector with elements $\langle f_n | g \rangle$ —a generalization of regular matrix multiplication. The infinite dimensional matrix is called the *representation* of L in $\{f_n\}$. If the matrix for L is diagonal, then we call that the *spectral representation* [42, p. 110].

The spectral representation for an operator L depends on the study of the inverse of the operator $L - \lambda$, which we will denote by $(L - \lambda)^{-1}$, for all complex values of λ [42, p. 125]. Let the domain and range of L be denoted by \mathcal{D}_L and \mathcal{R}_L . The *point (discrete) spectrum* is the set of λ for which $(L - \lambda)^{-1}$ does not exist. The *continuous spectrum* is the collection of λ for which $(L - \lambda)^{-1}$ exists and is defined on a set dense in \mathcal{R}_L , but for which it is unbounded. The *residual spectrum* is the collection of λ for which $(L - \lambda)^{-1}$ exists (it may or may not be bounded), but for which it is not defined on a set dense in \mathcal{R}_L . The *spectrum* of L consists of values of λ which belong to either the point, continuous or the residual spectrum [44, p. 371], [46, p. 21]. We summarized the taxonomy of the spectrum in Figure 3.2.

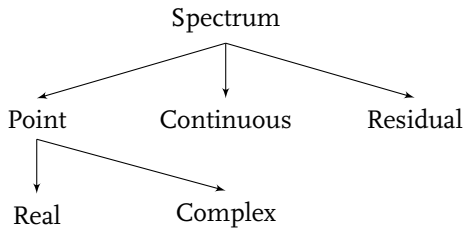


Figure 3.2 – Classification of the spectrum for an operator in a general space. Point spectrum is sometimes called the discrete spectrum.

3.3 Spectrum

After having defined the necessary terminology, in this section we will derive the modal structure (spectrum) of the MIM waveguide. We will specifically focus on the even modes of the waveguide, for which the *transverse magnetic* (TM) field component is an even function of the transverse coordinate, x . The reason why we focus on even modes is that we will be analyzing the scattering of the main, even mode of the MIM waveguide—which is also a TM mode—off of a symmetric junction with a different sized MIM waveguide. Due to the symmetry of the problem at hand, even modes will be sufficient. We could also solve for the case of the odd modes by a similar approach, but we omit that explicit solution for reasons of space. Evenness of the function is achieved by putting a fictitious *perfect electric conductor* (PEC) at the $x = 0$ plane of the waveguide, which forces the tangential electric field E_z to be an odd function, and the magnetic field H_y to be an even function of x . In other words, the modes of this fictitious waveguide with the PEC at $x = 0$ are mathematically the same as the even modes of the actual waveguide of interest, and so we will work with this hypothetical waveguide for our mathematics. The geometry is as shown in Figure 3.3. ϵ_m refers to the permittivity of the metal region and ϵ_i of the insulator region. At infrared frequencies, ϵ_m is a complex number with a large, negative real part and a relatively small imaginary part (the sign of which is determined by the time convention used, being negative for an $\exp(i\omega t)$ time dependence).

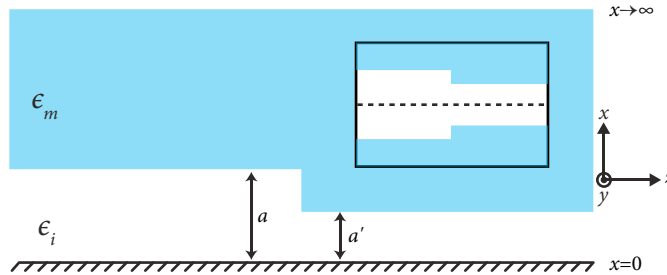


Figure 3.3 – Geometry for the even modes of the MIM waveguide. The $x = 0$ plane contains a fictitious perfect electric conductor to simplify the problem when dealing only with even TM modes of the guide. This fictitious MIM waveguide is equivalent to an actual guide with an insulator thickness of $2a$. The inset shows the equivalent symmetric junction of two MIM waveguides. The dashed line in the inset is the plane of symmetry, which is where the fictitious PEC layer is introduced.

Let us begin with Maxwell's equations for fields that have an $\exp(i\omega t)$ time dependence.

$$\begin{aligned}\nabla \times \mathbf{E}(\mathbf{r}) &= -i\omega\mu(x)\mathbf{H}(\mathbf{r}) \\ \nabla \times \mathbf{H}(\mathbf{r}) &= i\omega\epsilon(x)\mathbf{E}(\mathbf{r}).\end{aligned}\quad (3.3)$$

The MIM waveguide is a two dimensional structure which does not have any variation in the y direction. Therefore, we can eliminate all the derivatives with respect to y in Maxwell's equations. Furthermore, our study will be based on the TM modes which only have the H_y , E_x and E_z field components. Also, the uniformity of the waveguide in the z direction leads to $\exp(-ik_z z)$ as the space dependence in z by using the separation of variables technique for differential equations (k_z may, however, be a complex number). After simplifying the curl equations in (3.3), we have the following relationships between the different field components

$$\begin{aligned}i\omega\mu(x)H_y(x) &= ik_z E_x(x) + \frac{d}{dx}E_z(x) \\ ik_z H_y(x) &= i\omega\epsilon(x)E_x(x) \\ \frac{d}{dx}H_y(x) &= i\omega\epsilon(x)E_z(x).\end{aligned}\quad (3.4)$$

Using these equations we get the following differential equation for H_y

$$\left(\epsilon(x) \frac{d}{dx} \frac{1}{\epsilon(x)} \frac{d}{dx} + \omega^2 \mu(x) \epsilon(x) \right) H_y = k_z^2 H_y \quad (3.5)$$

and since $E_z(0) = 0$ by the PEC wall at $x = 0$, the boundary condition for H_y under (3.4) becomes $\frac{d}{dx} H_y(x)|_{x=0} = 0$. The equation (3.5) is in the *Sturm-Liouville* form [45, Ch. 5].

3.3.1 Point Spectrum

The standard approach [45, Ch. 5] in the calculation of the point spectrum of a Sturm-Liouville equation as in (3.5) starts with a redefinition of the space to \mathcal{L}_ϵ^2 —the set of all *weighted* Lebesgue square-integrable functions such that

$$\int |f(x)|^2 \frac{1}{\epsilon(x)} dx < \infty$$

which implies that the boundary condition at infinity should be $\lim_{x \rightarrow \infty} H_y(x) = 0$. The inner-product in \mathcal{L}_ϵ^2 , denoted by $\langle\langle \cdot | \cdot \rangle\rangle_\epsilon$, is then defined as

$$\langle\langle f | g \rangle\rangle_\epsilon = \int f^*(x) g(x) \frac{1}{\epsilon(x)} dx. \quad (3.6)$$

In order to have a *definite* metric for \mathcal{L}_ϵ^2 , the inner product should be such that $\langle\langle f | f \rangle\rangle_\epsilon > 0$ for all $f \neq 0$ so that the norm of any non-zero vector will be a positive quantity. This in turn implies that to have a definite metric, $\epsilon(x)$ should be a real and positive number for all x . Within the Hilbert space obtained by our choice of the inner product $\langle\langle \cdot | \cdot \rangle\rangle_\epsilon$, we can write (3.5) as $LH_y = k_z^2 H_y$. The operator

$$L = \epsilon(x) \frac{d}{dx} \frac{1}{\epsilon(x)} \frac{d}{dx} + \omega^2 \mu(x) \epsilon(x)$$

is self-adjoint since $\langle\langle f | Lg \rangle\rangle_\epsilon = \langle\langle Lf | g \rangle\rangle_\epsilon$ for all f and g as long as $\epsilon(x) \in \mathbb{R}$ and $\epsilon(x) > 0$. One can then easily prove that the point spectrum of L is purely real [47, p. 50]. The lossless dielectric slab waveguide, which satisfies all the criteria we mentioned, therefore has a purely real point spectrum.

Unfortunately, the arguments above fail for the MIM waveguide system since the condition $\epsilon(x) > 0$ is no longer satisfied [36]. The dielectric constants of metals can have negative real parts at some frequencies (e.g., in the infrared and visible regions), and generally also have imaginary components corresponding to loss, especially at optical frequencies. We will now separately analyze the lossy and the lossless metal cases.

Lossless Case

Since $|\text{Im}(\epsilon_m)| \ll |\text{Re}(\epsilon_m)|$ at infrared frequencies, it is worthwhile investigating the case of real, negative permittivity, i.e., $\epsilon_m = -|\epsilon_m|$. The standard Sturm-Liouville theory is not applicable in this case, because it requires the weighting function $\epsilon(x)$ to have the same sign over its entire domain of definition [47, p. 50]. However, $\epsilon_i > 0$ whereas $\epsilon_m < 0$ for the MIM waveguide, under the approximation of negligible loss. The definition of the inner-product (3.6) becomes *indefinite* in this case, since we can have $\langle\langle f|f \rangle\rangle_\epsilon \leq 0$ for some $f \neq 0$. As a result, we no longer can operate in the Hilbert space. The space of functions with an indefinite metric is called the *Krein space*. In contrast to the Hilbert space case, the spectrum of the self-adjoint operators in Krein spaces is, in general, not real [48, p. 220]. An early analysis of a real Sturm-Liouville equation with a complex point spectrum can be found in [49].

To prove that (3.5) accepts complex solutions even when $\epsilon(x) \in \mathbb{R}$, let us work in the well defined L^2 space with an inner-product as defined in (3.1). Because $\langle \cdot | \cdot \rangle$ is always definite, we are back in the Hilbert space, but L is no longer self-adjoint in L^2 . Two integrations by parts⁴ give L^\dagger as

$$L^\dagger = \frac{d}{dx} \frac{1}{\epsilon(x)} \frac{d}{dx} \epsilon(x) + \omega^2 \mu(x) \epsilon(x)$$

with boundary conditions

$$\begin{aligned} H_y(x) \Big|_{x \rightarrow \infty} &= 0 \\ \frac{d}{dx} \epsilon(x) H_y(x) \Big|_{x=0} &= 0. \end{aligned}$$

We see that $L^\dagger = \epsilon^{-1} L \epsilon$ which makes L by definition *pseudo-Hermitian* [50, 51]. It has

⁴Examples on how to calculate operator adjoints can be found in [45, pp. 150-154].

been proved that a pseudo-Hermitian operator does not have a real spectrum if \mathcal{L}_ϵ^2 is indefinite [50, Th. 3].

Alternatively, we can approach the problem by defining

$$\mathsf{L}' = \frac{d}{dx} \frac{1}{\epsilon(x)} \frac{d}{dx} + \omega^2 \mu(x)$$

and rewriting (3.5) as

$$\mathsf{L}' H_y = \frac{k_z^2}{\epsilon} H_y.$$

Using (3.1) it can be shown that L' is self-adjoint in \mathcal{L}^2 so that

$$\langle H_{y2} | \mathsf{L}' H_{y1} \rangle = \langle \mathsf{L}' H_{y2} | H_{y1} \rangle$$

which leads to the *generalized eigenvalue problem* for the self-adjoint operators L' and ϵ^{-1} as

$$\mathsf{L}' H_y = k_z^2 \epsilon^{-1} H_y$$

where k_z^2 is the eigenvalue. The point spectrum of the self-adjoint generalized eigenvalue problem will be complex only if *both* L' and ϵ^{-1} are indefinite [52, p. 38]. The indefiniteness of ϵ^{-1} is trivial because epsilon can be a positive or negative quantity now. To show that L' is indefinite, observe that by using the boundary conditions in integration by parts, one can get

$$\langle H_y | \mathsf{L}' H_y \rangle = \int_0^\infty \left(\omega^2 \mu |H_y(x)|^2 - \frac{1}{\epsilon(x)} \left| \frac{dH_y(x)}{dx} \right|^2 \right) dx$$

which can be positive or negative depending on the choice of $H_y(x) \in \mathcal{L}^2$. Therefore, L' is indefinite, and k_z^2 will accept complex values. Note that the classification of the point spectrum into the real and the complex categories is based on k_z^2 and not k_z . Hence, the set of modes with purely real and negative k_z^2 —which leads to a purely imaginary k_z —are categorized as real modes in this approach.

Lossy Case

As we mentioned earlier, ϵ_m has an imaginary part. As a result, for those cases when neglecting the imaginary part of ϵ_m is not desired, L cannot be made self-adjoint by a redefinition of the inner-product. Therefore, the point spectrum—the set of k_z^2 for which $(L - k_z^2)$ does not have an inverse—will be complex. A general classification of the spectrum for non-self-adjoint operators is still an open problem [48, p. 301], [53]. Also, completeness of the spectrum is difficult to prove. However, the MIM waveguiding problem can be shown to have a spectrum which forms a complete basis set even when L is non-self-adjoint [45, Th. 5.3, pp. 333–334].

Mode Shape

The dispersion equation that should be solved in order to find the k_z values for the modes of the MIM waveguide is derived by satisfying the continuity of tangential electric and magnetic fields at material boundaries and applying the boundary conditions as illustrated in [45, pp. 462–470] and [17, 24, 27, 31, 35, 36]. We refer the reader to Section 2.4 for the details. The eigenvectors (ψ_n) and the dispersion equation for the corresponding eigenvalues ($k_{z,n}^2$) of (3.5) for the even TM modes of the MIM waveguide are

$$\psi_n(x) = H_0 \begin{cases} \frac{\cosh(\kappa_{i,n}x)}{\cosh(\kappa_{i,n}a)} & 0 < x < a \\ e^{-\kappa_{m,n}(x-a)} & a < x < \infty \end{cases} \quad (3.7)$$

$$\tanh(\kappa_{i,n}a) = -\frac{\kappa_{m,n}/\epsilon_m}{\kappa_{i,n}/\epsilon_i} \quad (3.8)$$

$$k_{z,n}^2 = \kappa_{m,n}^2 + \omega^2 \mu \epsilon_m = \kappa_{i,n}^2 + \omega^2 \mu \epsilon_i \quad (3.9)$$

where $\text{Re}(\kappa_{m,n}) > 0$ so that $\psi_n(x)$ does not diverge and is integrable. Here n is a discrete index for the eigenvalues and the eigenfunctions. Note that we have chosen to write the modal shape in terms of the surface mode formulation of [24, Sec. 3]. Surface modes are the main propagating modes for the MIM waveguide and have hyperbolic modal shapes. It is equivalently possible to describe the modes in terms of oscillatory shapes using trigonometric functions [24]—analogous to the modes of the dielectric

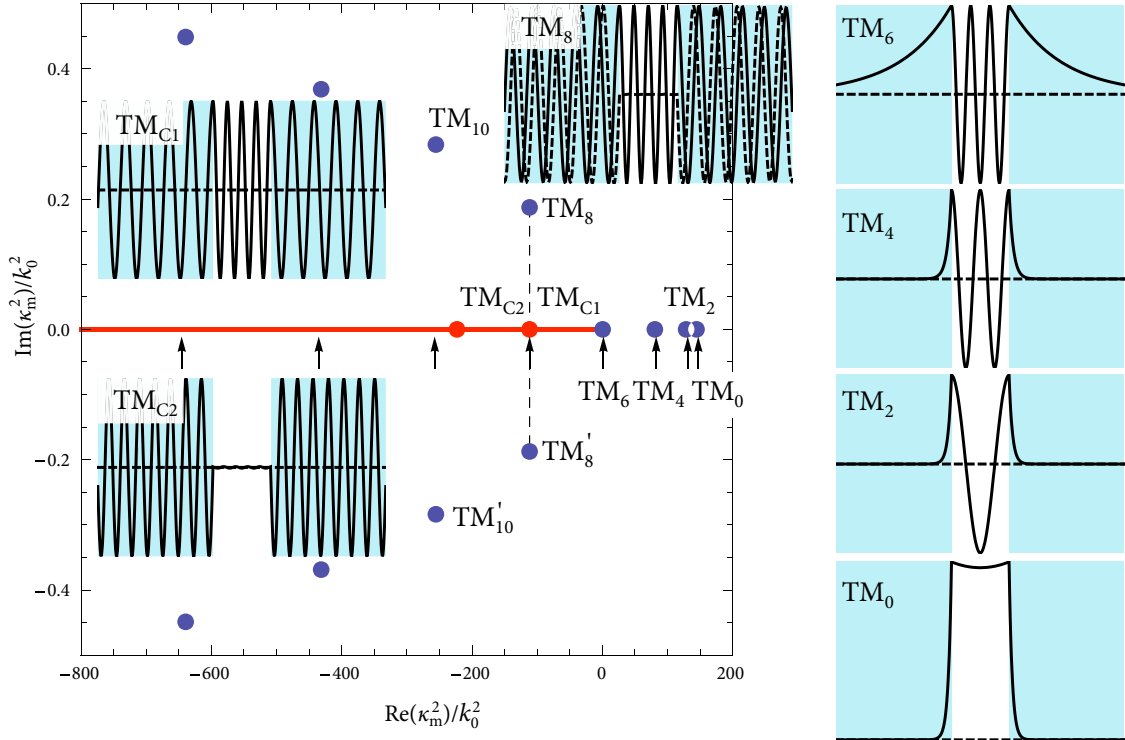


Figure 3.4 – Spectrum of the MIM waveguide for $\epsilon_m = -143.497$ and $2a = \lambda/4$ where $\lambda = 1550\text{nm}$ is the wavelength of operation. There are four real modes and an infinite number of complex modes, all denoted with the \bullet symbol. The **thick line** denotes the continuous spectrum. Due to the fact that ϵ_m is real, complex modes come in complex conjugate pairs. Insets show the H_y mode shapes in the x direction for the discrete spectrum (TM_0 through TM_8) and the continuous spectrum (TM_{C1} and TM_{C2})—solid lines in the insets are the real part of the mode, dashed lines are the imaginary part. The locations of the drawn continuous modes are shown by the \bullet symbol. Modes in the continuous spectrum are purely oscillatory in the x direction. Complex modes have a small decay, which is not visually apparent in the inset for TM_8 . Arrows (\uparrow) denote the position of the modes of a parallel plate waveguide with a separation of a —equivalent to the limiting case $h \rightarrow 0$ in Figure 3.8.

waveguide. Analytical continuation of the modal parameters $(\kappa_i, \kappa_m, k_z)$ makes the two formulations equivalent.

3.3.2 Continuous Spectrum

In this section, we will mathematically show how a continuous spectrum can exist [35, 36] in the MIM waveguide and relate it to the continuous spectrum of the dielectric slab waveguide. The utility of the continuous spectrum will be evident in the mode matching

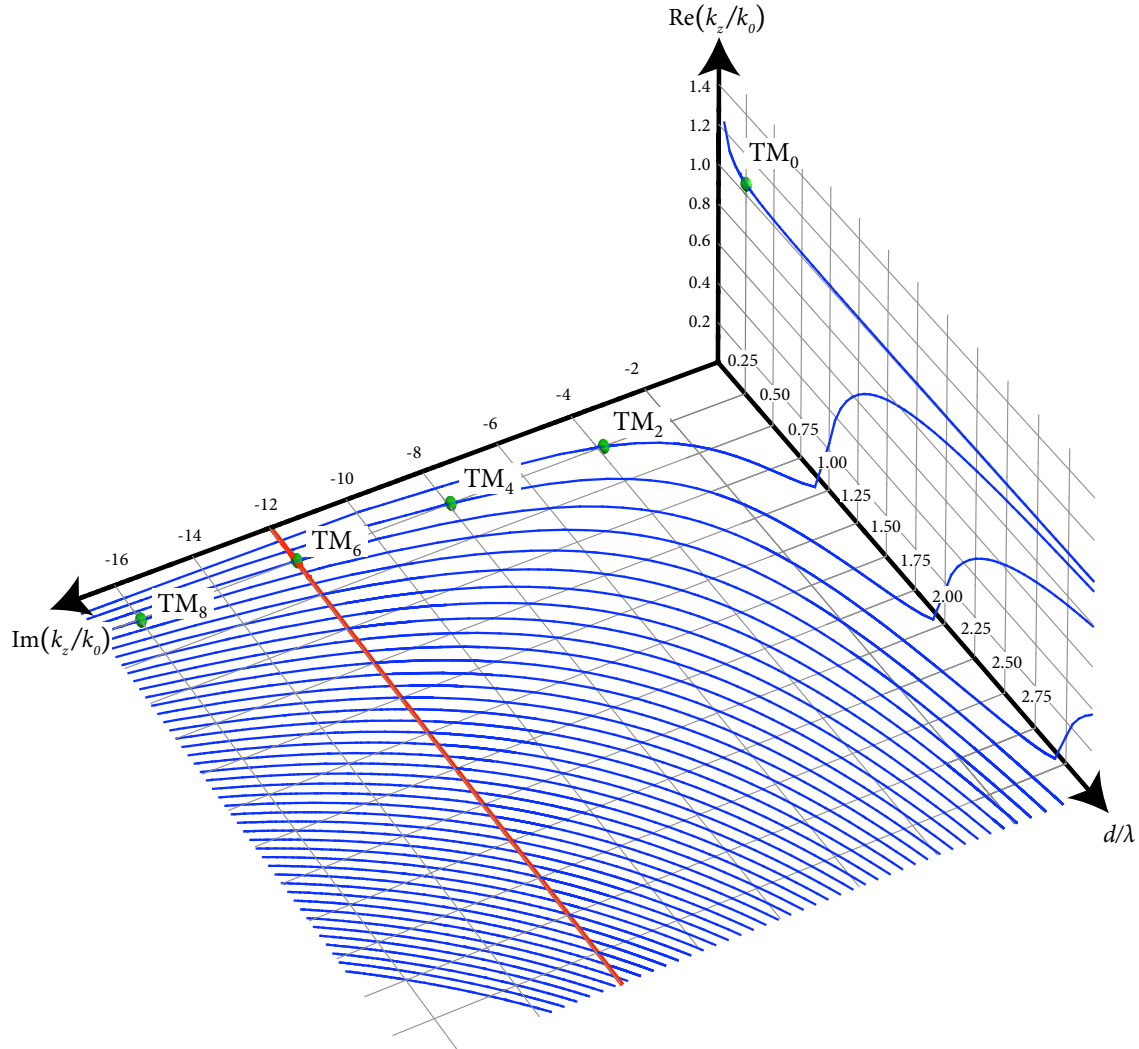


Figure 3.5 – Spectrum of the MIM waveguide as a function of $d = 2a$, $\text{Re}(k_z/k_0)$ and $\text{Im}(k_z/k_0)$ where $k_0 = 2\pi/\lambda$ is the free space wave vector. $\epsilon_m = -143.497$ is assumed, which corresponds to the real part of the permittivity of silver at a wavelength of $\lambda = 1550\text{nm}$. The thick line denotes the limit of the real spectrum. Spheres denote the point spectrum for the $d = 2a = \lambda/4$ case as also shown in Figure 3.4. It can be seen that only the lowest order mode, TM_0 , is propagating for $d = \lambda/4$ and the rest of the modes are highly evanescent.

analysis.

As clearly argued in [54, p. 16], the condition of square integrability of the modes can be replaced by the weaker condition of finiteness of the modes in their domain of definition. For the MIM waveguide, this would imply a non-zero, yet finite electromagnetic

field at infinity. These infinite-extent and, therefore, infinite energy, continuum modes (which can be normalized through the use of the Dirac delta distributions as illustrated in [55, pp. 134–135], and [56, pp. 141–148]) are integrated to realize any physically possible finite energy field configuration. In this respect, such an approach is similar to the well-known Fourier transform methods, where finite energy functions are expanded in terms of the infinite energy exponentials.

Constraining fields to be finite, instead of zero, at infinity leads to the following field profile

$$\phi_v(x) = H_0 \begin{cases} \frac{\cosh(\kappa_{i,v}x)}{\cosh(\kappa_{i,v}a)} & 0 < x < a \\ \cosh(\kappa_{m,v}(x-a)) \\ + \zeta \sinh(\kappa_{m,v}(x-a)) & a < x < \infty \end{cases} \quad (3.10)$$

$$\zeta = \frac{\kappa_{i,v}/\epsilon_i}{\kappa_{m,v}/\epsilon_m} \tanh(\kappa_{i,v}a) \quad (3.11)$$

$$k_{z,v}^2 = \kappa_{m,v}^2 + \omega^2 \mu \epsilon_m = \kappa_{i,v}^2 + \omega^2 \mu \epsilon_i \quad (3.12)$$

which is calculated very similarly to the dielectric slab example in [45, pp. 462–470]. Here v is a continuous index for different functions in the continuous spectrum. For finite ϕ_v , the arguments inside the hyperbolic functions for $x > a$ in (3.10), $\kappa_{m,v}$, should be purely imaginary which implies that $\text{Re}(\kappa_{m,v}^2) < 0$ and $\text{Im}(\kappa_{m,v}^2) = 0$. These conditions can be written in terms of $k_{z,v}$ by using (3.12) as

$$\text{Re}(k_{z,v}^2 - \omega^2 \mu \epsilon_m) < 0 \quad \text{and} \quad \text{Im}(k_{z,v}^2 - \omega^2 \mu \epsilon_m) = 0.$$

Note that when (3.8) holds true, we have $\zeta = -1$ in (3.11) which makes (3.10) and (3.7) equivalent.

3.3.3 Residual Spectrum

We saw that (3.5) is a second order differential equation which could also be written as $LH_y = k_z^2 H_y$ where L is a differential operator. In [42, p. 200] it is claimed that differential operators have an empty residual spectrum, but a proof is not provided.

In [45, p. 224], the residual spectrum is said not to occur in most of the electromagnetic applications, and in [45, p. 238] the residual spectrum is said to be empty for typical differential operators, though it is highlighted that such a fact is not a general result. For (3.5) we did not find any vectors belonging to the residual spectrum of L .

3.3.4 Orthogonality relationships

Orthogonality and completeness are two very valuable properties of modes, which make the mode matching technique, to be discussed in the next section, possible. Orthogonality of the modes for the self-adjoint, and non-self-adjoint cases are usually expressed using different definitions of the inner product. In this work, we will use the *pseudo-inner product*, $[\cdot | \cdot]$, defined as [52, p. 42]

$$[f|g] = \int_0^\infty f(x)g(x) dx.$$

It can be shown that two different eigenfunctions of L , $\psi_1(x)$ and $\psi_2(x)$, corresponding to two different eigenvalues $k_{z,1}^2$ and $k_{z,2}^2$ are pseudo-orthogonal with $\epsilon^{-1}(x)$ weight [43, p. 330], [52, p. 47].

$$[\epsilon^{-1}\psi_1|\psi_2] = 0. \quad (3.13)$$

From (3.4) it can be seen that $\epsilon^{-1}\psi_1$ is proportional to the transverse electric field component E_x of the mode. Therefore, the orthogonality condition can also be written as

$$\int_0^\infty E_{x1}(x)H_{y2}(x) dx = \int_A \mathbf{E}_1(\mathbf{r}) \times \mathbf{H}_2(\mathbf{r}) \cdot d\mathbf{A} = 0$$

which is the well known modal orthogonality condition proved by the Lorentz reciprocity theorem [57, p. 336], where A denotes the cross section of the waveguide.

One can directly verify (3.13) by integration and using $\kappa_{m,1}^2 - \kappa_{m,2}^2 = \kappa_{i,1}^2 - \kappa_{i,2}^2$ which is a result of (3.9). The following orthogonality conditions between the elements of the

point (ψ_n) and the continuous (ϕ_ν) spectrum can similarly be proved

$$\begin{aligned} [\epsilon^{-1}\psi_n|\phi_\nu] &= 0 \quad \text{for all } n \text{ and } \nu, \\ [\epsilon^{-1}\phi_\mu|\phi_\nu] &= 0 \quad \text{for } \nu \neq \mu. \end{aligned}$$

The orthogonality conditions talked about in this section can also be described in terms of the bi-orthogonal relationships between the eigenfunctions of the operators L and L^\dagger as has been done in [45, Sec. 5.3], and [58]. In [59] four examples which illustrate how to choose the weight of the inner product definition so as to have orthogonal basis functions are given.

In the following sections, we will be working with fields at the junction of two different waveguides. For notational abbreviation we will use the following convention

$$\begin{aligned} e_{\{L,R\}}^{(i)} &= E_{x,i}^{\{L,R\}} \\ h_{\{L,R\}}^{(i)} &= H_{y,i}^{\{L,R\}} \end{aligned}$$

where $\{L, R\}$ is used to denote the modes of the left and right side of the junction, which leads to the following orthogonality condition

$$\left[e_{\{L,R\}}^{(i)} | h_{\{L,R\}}^{(j)} \right] = \delta_{ij} \Omega_{\{L,R\}} \quad (3.14)$$

where δ_{ij} is the Kronecker delta function and Ω is the overlap integral of the electric and magnetic transverse fields.

After the classification and analysis of the MIM waveguide modes, we will now visualize different parts of its spectrum by finding the zeros of the respective dispersion equations through the use of the argument principle method as explained in Appendix B. We will use the adjectives in Table 3.1 to further differentiate between the modes.

Leaky modes are not normalizable and are not part of the spectrum. *Proper* modes can be normalized by the usual integration and they form the point spectrum. *Improper* modes can be normalized by using the Dirac delta functions, $\delta(x)$. They form the continuous spectrum. *Forward* modes have a positive phase velocity, whereas the *backward* modes have a negative phase velocity. We decide on the sign of $\text{Re}(k_z)$ based

Table 3.1 – Adjectives

<i>Signifier</i>	<i>Signified</i>
Leaky	$\text{Re}(\kappa_m) < 0$
Proper	$\text{Re}(\kappa_m) > 0$
Improper	$\text{Re}(\kappa_m) = 0$
Forward	$\text{Re}(k_z) > 0$
Backward	$\text{Re}(k_z) < 0$

on $\text{Im}(k_z)$: By definition, all modes are propagating in the $+z$ direction. Therefore, in the limit $z \rightarrow \infty$, the fields should go to zero. Such a behavior is possible only if $\text{Im}(k_z)$ is negative, since the fields have an $\exp(-ik_z z)$ dependence. The argument principle method gives us the κ_m value for the modes. By using (3.9) we get the k_z^2 value. We then calculate $(k_z^2)^{1/2}$ and choose the root which satisfies $\text{Im}(k_z) < 0$. Different definitions of forward and backward modes—including the ones we use—are analyzed in [60]. The definition we use for the leaky modes is the same as the one used in [19, Sec. 1.5].

In Figure 3.4 the spectrum of an idealized lossless silver-like MIM waveguide is shown on the plane of κ_m^2 for $\epsilon_m = -143.497$ which is the real part of the permittivity of silver at a wavelength λ of 1550 nm [16, 61]. There are four real modes for $2a = \lambda/4$ — $\text{TM}_0, \text{TM}_2, \text{TM}_4, \text{TM}_6$ —indexed according to the number of zero crossings in H_y . There is also an infinite number of complex modes, which are those with eight and more zero crossings in the insulator region. These modes have a κ_m with a positive real part that is rather small compared to the imaginary part—this can also be deduced from the scale of the imaginary axis of Figure 3.4. The continuous spectrum is illustrated by the thick line which corresponds to $\text{Re}(\kappa_m^2) < 0$ and $\text{Im}(\kappa_m^2) = 0$. This line is also the branch cut of the square root function that is used to get κ_m from κ_m^2 .

The field profiles of the modes in the insulator region, as shown in the insets of Figure 3.4, look quite similar to the field profile of the even modes of a parallel plate waveguide with a plate separation of $2a$. The even modes of a parallel plate waveguide have $\kappa_{i,n}^2 = -n^2\pi^2/a^2$. We plotted the corresponding $\kappa_{m,n}^2$ values on Figure 3.4 by using (3.9). It can be seen that such a description gives a quite good estimate of the location of the modes on the complex κ_m^2 plane.

$\kappa_m^2 = 0$ is the bifurcation point for the point spectrum when ϵ_m is purely real. For

positive κ_m^2 , the point spectrum has real modes, whereas for negative κ_m^2 , the point spectrum splits into two branches that are complex conjugates of one another. $\kappa_m^2 = 0$ corresponds to $k_z^2 = \epsilon_m k_0^2$ which then implies $k_z = -i\sqrt{|\epsilon_m|}k_0$ —bounded modes should have $\text{Im}(k_z) < 0$. In Figure 3.5 the point spectrum is visualized as a function of the insulator thickness $d = 2a$ of the MIM waveguide and the real and imaginary parts of k_z for the same ϵ_m as in Figure 3.4. The thick line in Figure 3.5 denotes the limit of the real point spectrum which is the bifurcation point of the modes. For $\text{Im}(k_z) < -\sqrt{|\epsilon_m|}k_0$ there are no real modes. The point spectrum for the $d = 2a = \lambda/4$ case of Figure 3.4 is also highlighted with spheres in Figure 3.5. For the sake of clarity, we only drew one branch of modes after the bifurcation. Due to the scale of the axes in Figure 3.5, the quite small real part of k_z for the complex modes after the bifurcation line is not visibly discernible, but is numerically there.

In Figure 3.6 the spectrum is plotted this time on the κ_m plane with the same set of parameters as used in Figure 3.4. The two branches after the bifurcation form the forward and backward proper, complex modes. Leaky modes which are not part of the spectrum, but nevertheless are solutions to (3.8)-(3.9) are also shown. When loss is introduced to the metal, the spectrum moves on the complex plane as illustrated in Figure 3.7. Forward, proper, complex modes of Figure 3.6 turn into leaky modes by migrating into the third quadrant of the complex κ_m plane.

In Table 3.2 we provide the numerical values of κ_m/k_0 , where $k_0 = 2\pi/\lambda$, for the modes in the point spectrum as labeled in Figure 3.4. The upper line in each row is the value for the $\epsilon_m \in \mathbb{R}$ case, the lower line is for the $\epsilon_m \in \mathbb{C}$ case. The effect of loss is greatest on the TM_6 mode.

3.4 Mode-Matching

In this section, we will make use of the spectrum of the MIM waveguide to calculate the scattering at the junction of two guides with different cross sections. We will use the mode matching technique [62] commonly used in the microwave and the optical domains [63–66].

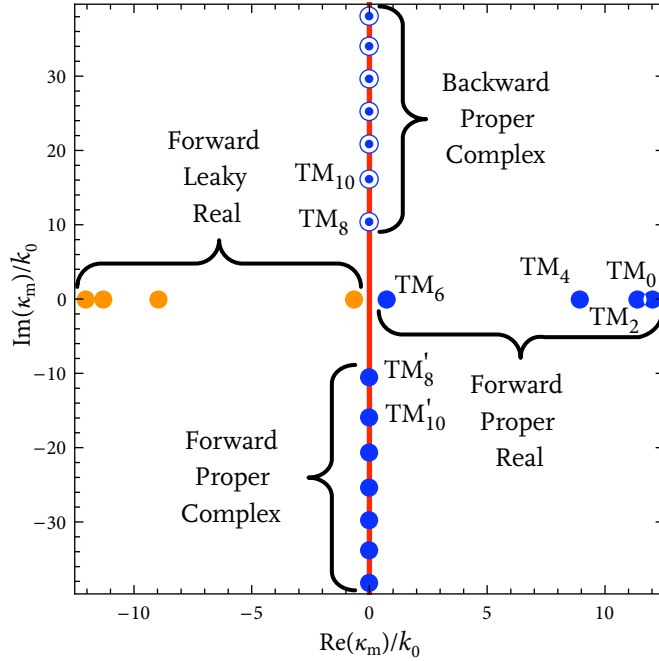


Figure 3.6 – Visualization of the spectrum on the κ_m plane. All parameters are the same as in Figure 3.4. **Proper** and **leaky** modes are shown for forward, ●, and backward, ○, modes. The **thick line** is the continuous spectrum. The complex modes have a small, yet non-zero, positive real part—which is what makes them proper modes, unlike the continuous part of the spectrum which is improper. Thus complex modes and the continuous spectrum do not intersect.

Table 3.2 – κ_m/k_0 values for the modes labeled in Figure 3.4

TM ₀	12.02521374394057	+	i 0.0
	12.03170325421919	+	i 0.39535643587620
TM ₂	11.34454132059978	+	i 0.0
	11.35226216175467	+	i 0.41892103144838
TM ₄	8.98087712606770	+	i 0.0
	8.99644754875734	+	i 0.52888321538511
TM ₆	0.7136870643968289	+	i 0.0
	2.247924588647662	+	i 2.124681976891650
TM ₈	0.00887301858491	+	i 10.55951095636977
	0.45907739584359	+	i 10.56851955358188

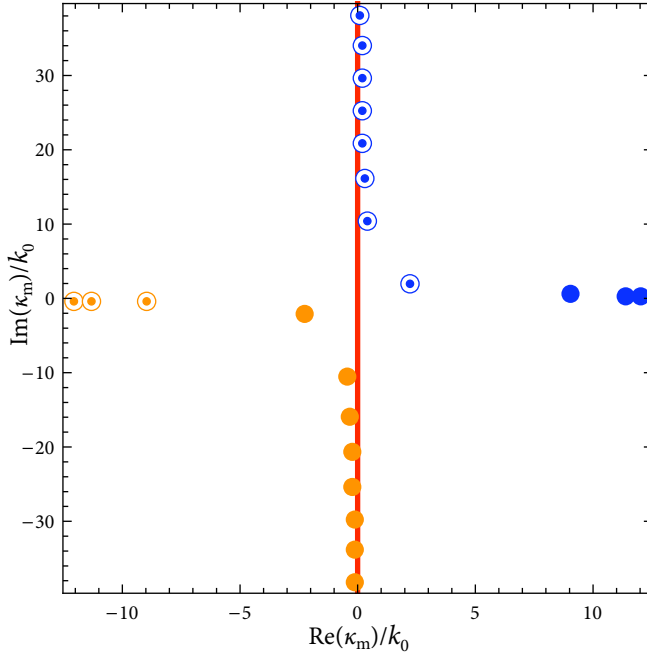


Figure 3.7 – Effects of loss on the spectrum. All parameters are the same as in Figure 3.6 except $\epsilon_m = -143.497 - i9.517$. Comparison with Figure 3.6 shows that the forward, proper, complex modes on the fourth quadrant have moved to the third quadrant and thus became leaky modes.

3.4.1 Birth of the Discretuum

The presence of a continuous spectrum leads to the formation of integral equations when the mode-matching method is applied [55, Ch. 5]. The integral equation is then expanded using an orthogonal basis set—not necessarily that of the modes—to solve the scattering problem.

Another way to approach the scattering problem is to limit the transverse coordinates by a PEC wall. This approach has the effect of discretizing the continuum part of the spectrum [54, pp. 38–41], [48, pp. 204–205]—turning it into a *discretuum*⁵. To limit parasitic reflections from the PEC walls, absorbing layers can be positioned before the PEC termination [63, Ch. 3]. In [68, Sec. 3.2b], a detailed analysis of how the continuous spectrum appears from a discrete collection can be found. We will use a PEC wall to discretize the continuous spectrum. Also, we will not use any perfectly matched layers to limit parasitic reflections since the metallic sections with permittivity ϵ_m effectively

⁵Here, we borrow the terminology from [67] for our *détournement*.

absorb the fields away from the junction.

The geometry is as shown in Figure 3.8. For the left waveguide the dispersion equation for modes becomes

$$\tanh(\kappa_{i,n}a) = -\frac{\kappa_{m,n}/\epsilon_m}{\kappa_{i,n}/\epsilon_i} \tanh(\kappa_{m,n}h) \quad (3.15)$$

which asymptotes to (3.8) as $h \rightarrow \infty$. The transverse magnetic field shape is

$$\psi_n(x) = H_0 \begin{cases} \frac{\cosh(\kappa_{i,n}x)}{\cosh(\kappa_{i,n}a)} & 0 < x < a \\ \frac{\cosh(\kappa_{m,n}(x-a-h))}{\cosh(\kappa_{m,n}h)} & a < x < a+h. \end{cases} \quad (3.16)$$

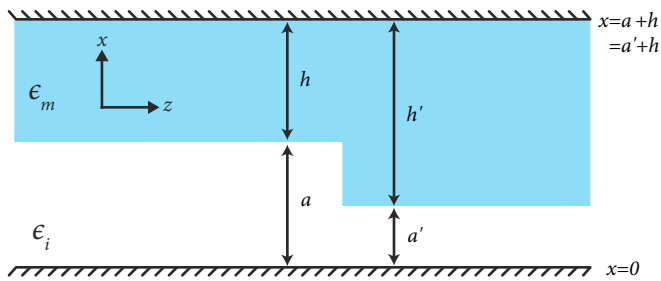


Figure 3.8 – Geometry for mode matching. $x = a + h$ plane of Figure 3.8 is terminated by a perfect electric conductor which leads to a discretization of the continuous spectrum.

In Figure 3.9 we show the effects of positioning a PEC wall at the top of the lossy MIM waveguide. The point spectrum is almost the same as in the case without a PEC wall at the top. The continuous spectrum is discretized, and shows an anti-crossing behavior (the repulsion between modes which couple to each other) similar to the one observed in coupled waveguide systems. One way to understand the anti-crossing is to get rid of the PEC walls by the method of images to come up with an infinite lattice of parallel MIM waveguides each separated from each other by a distance $2(a + h)$. We observed that the perturbations to the discretuum decrease as we increase h , as expected from coupled mode theory. Also, the magnitude of anti-crossing behavior in the discretuum depends on the distance to the nearest mode in the point spectrum. The closer the point spectrum gets to the continuous spectrum, the larger the anti-crossing effect is. We should note that the modes of the PEC terminated MIM waveguide are equivalent

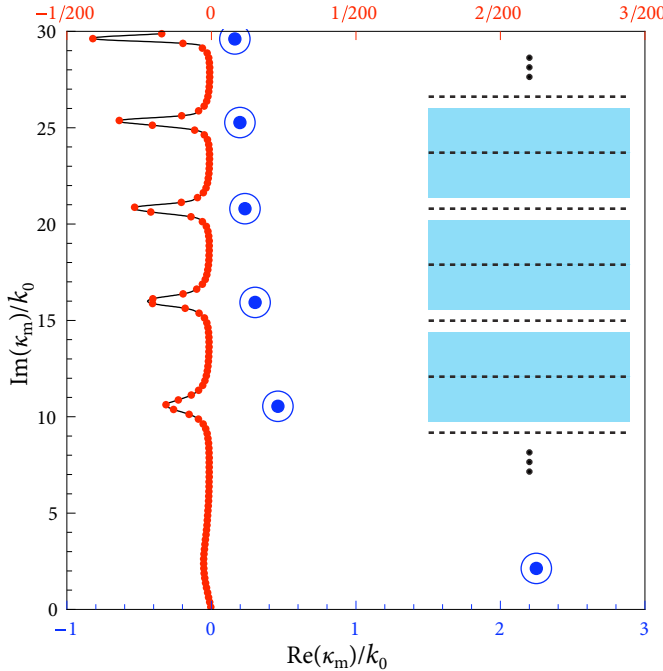


Figure 3.9 – Effects of termination of the metal by a PEC wall—as in Figure 3.8—on the spectrum. $\epsilon_m = -143.497 - i9.517$, $\epsilon_i = 1.0$, $2a = \lambda/4$, $h = 2\lambda$, $k_0 = 2\pi/\lambda$, $\lambda = 1550\text{nm}$. The spectrum looks very similar to Figure 3.7. In order to highlight the discretization of the continuum, we show a zoomed portion of the κ_m plane. The complex modes and the discretuum show anti-crossing behavior. We use two different axes for the real part of κ_m . The scale on the bottom refers to the complex modes, \circlearrowleft , whereas the one on the top refers to the discretuum, \bullet . The inset shows a portion of the infinite lattice created by the repeated application of image reflection off of the PEC boundaries. Dashed lines in the inset signify the locations of zero tangential electric field, where a PEC termination can be applied. In separate calculations not shown in this figure, we observe that as h is increased, the magnitude of the anti-crossing behavior of the continuum decreases as a result of decreased coupling between adjacent MIM waveguides.

to the even modes of a one-dimensional metallic photonic crystal at the center of the Brillouin zone as described in [36, Sec. 4]. More information on the evolution of the modes and their dependence on material properties can be found there.

3.4.2 Are the modes complete?

Before we attempt the calculation of the scattering properties of modes at waveguide junctions, we will first investigate the completeness properties of the set of modes we have at our disposal—the point and the continuous parts of the spectrum. The way

we will test completeness is to expand the main mode of an MIM waveguide of a given thickness in terms of the modes of the MIM waveguide with a different thickness.

Suppose that we are working with the geometry depicted in Figure 3.8. Let us expand the k^{th} mode on the right hand side of the junction in terms of the modes on the left as

$$e_R^{(k)}(x) = \sum_{m=1}^L A_{km} e_L^{(m)}(x).$$

In order to find A_{km} we *test* the above equation (i.e. discretize the equation by the use of integration of both sides by a given function) with $h_L^{(n)}$ and use (3.14) to get

$$A_{kn} = \frac{\left[e_R^{(k)} \middle| h_L^{(n)} \right]}{\Omega_L^{(n)}}.$$

Very similarly, we get the following for the magnetic fields

$$h_R^{(k)}(x) = \sum_{m=1}^L \frac{\left[e_L^{(m)} \middle| h_R^{(k)} \right]}{\Omega_L^{(m)}} h_L^{(m)}(x). \quad (3.17)$$

What is the error in this expansion? We can get a measure of it by writing it as

$$e_R^{(k)}(x) - \sum_{m=1}^L \frac{\left[e_R^{(k)} \middle| h_L^{(m)} \right]}{\Omega_L^{(m)}} e_L^{(m)}(x).$$

Calculating the pseudo-inner product of the above expression with $h_R^{(k)}$ and then dividing it by $\Omega_R^{(k)}$ gives an error estimate as

$$\left| 1 - \sum_{m=1}^L \frac{\left[e_R^{(k)} \middle| h_L^{(m)} \right] \left[e_L^{(m)} \middle| h_R^{(k)} \right]}{\Omega_L^{(m)} \Omega_R^{(k)}} \right|.$$

Calculating the error based on the magnetic field expansion results in the same expression.

In [69–74] the importance of the complex modes has been demonstrated. In Figure

3.10 we show the importance of the continuous spectrum. As shown in Figure 3.10(a) without the continuous spectrum, the field expansion converges, but to a field profile which is not the same as the desired profile of the right junction. On the other hand, inclusion of the continuous spectrum through the discretization of the continuum by a PEC wall leads to the correct field profile as illustrated in Figure 3.10(b). It can be observed that the expansion based on the point spectrum only quite nicely fits the field profile of the right waveguide in the insulating region of the left waveguide ($x/\lambda < 0.125$); however, in the metal region ($x/\lambda > 0.125$) the expansion fails. The point spectrum of the left waveguide has an exponentially decaying field profile for $x/\lambda > 0.125$ which turns out to be insufficient for the expansion of an arbitrary field profile in the metal. The continuous spectrum, with its non-decaying field profile, makes field expansion in the metal region possible.

3.4.3 Field Stitching

Now that we know how to treat the continuous spectrum and are confident that the collection of the point and the continuous spectrum results in a complete basis set, we can proceed with the mode-matching formalism. We will begin by assuming that the p^{th} mode of the left waveguide propagates toward the right, scatters and creates the following set of fields at the right and left sides of the junction, which by the continuity of the tangential magnetic and electric fields, are set equal

$$\sum_{m=1}^{\infty} (\delta_{mp} + R_{mp}) h_L^{(m)}(x) = \sum_{k=1}^{\infty} T_{kp} h_R^{(k)}(x) \quad (3.18)$$

$$\sum_{m=1}^{\infty} (\delta_{mp} - R_{mp}) e_L^{(m)}(x) = \sum_{k=1}^{\infty} T_{kp} e_R^{(k)}(x). \quad (3.19)$$

Here R_{mp} is the reflection coefficient of the m^{th} mode of the left waveguide in response to an incoming field in the p^{th} mode. Similarly, T_{kp} is the transmission coefficient of the k^{th} mode of the right waveguide. Note that we chose R_{mp} to denote the reflection coefficient for the transverse magnetic fields, which automatically results in $-R_{mp}$ as the reflection coefficient for the transverse electric fields.

In [75], it is shown that the testing of the above equations should be done by the

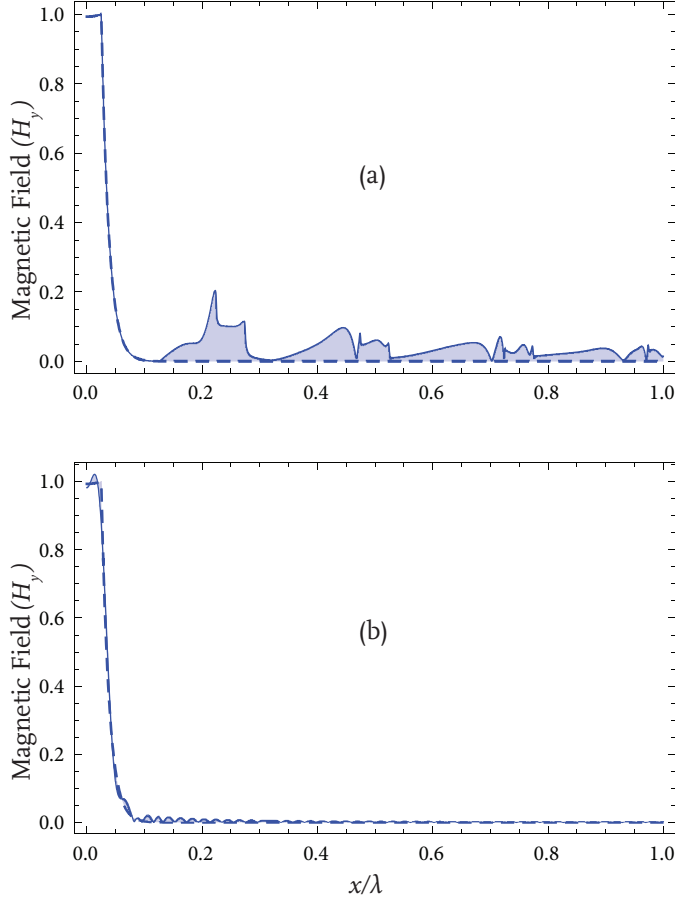


Figure 3.10 – Effects of the continuous spectrum on mode expansion. $\epsilon_m = -143.497 - i9.517$. The main mode of the right waveguide, $h_R^{(1)}(x)$, with $2a' = \lambda/20$ is expanded in terms of the modes of the left waveguide, $h_L^{(m)}(x)$, with $2a = \lambda/4$. The dashed lines show the magnitude of the magnetic field profile of the main mode of the right waveguide. The solid line shows the result of the expansion of (3.17). Shaded regions show the error from the use of a particular expansion, i.e., the difference between the expansion and the actual right waveguide mode. Due to symmetry, only half of the full modal profile is plotted. (a) Open waveguide of Figure 3.3, expansion made using the point spectrum only. (b) PEC terminated MIM waveguide of Figure 3.8, with $a + h = a' + h' = \lambda$, expansion made using the discretuum and the point spectrum.

magnetic field of the larger waveguide for enforcing electric field continuity (3.19) and by the electric field of the smaller waveguide to enforce the magnetic field continuity (3.18). Although that analysis was specifically done for waveguides with perfect metals ($|\epsilon_m| \rightarrow \infty$), we still use that strategy so that the formulation limits to the correct one should the metals be made perfect.

For those cases where $a < a'$, we will take the pseudo-inner product of (3.18) with $e_L^{(n)}$ and of (3.19) with $h_R^{(n)}$. Furthermore, assuming there are L modes on the left and R modes on the right, we get

$$\begin{aligned} \sum_{m=1}^L (\delta_{mp} + R_{mp}) \Omega_L^{(m)} \delta_{mn} &= \sum_{k=1}^R T_{kp} [e_L^{(n)} | h_R^{(k)}] \\ \sum_{m=1}^L (\delta_{mp} - R_{mp}) [e_L^{(m)} | h_R^{(n)}] &= \sum_{k=1}^R T_{kp} \Omega_R^{(k)} \delta_{kn} \end{aligned}$$

with the help of (3.14). When $a > a'$ by using $e_R^{(n)}$ and $h_L^{(n)}$ to test (3.18) and (3.19) respectively, we arrive at the following set of equations

$$\begin{aligned} \sum_{m=1}^L (\delta_{mp} + R_{mp}) [e_R^{(n)} | h_L^{(m)}] &= \sum_{k=1}^R T_{kp} \Omega_R^{(k)} \delta_{kn} \\ \sum_{m=1}^L (\delta_{mp} - R_{mp}) \Omega_L^{(m)} \delta_{mn} &= \sum_{k=1}^R T_{kp} [e_R^{(k)} | h_L^{(n)}]. \end{aligned}$$

These are linear matrix equations with R_{mp} and T_{kp} as the unknowns. After calculating the inner products, the set of equations can be inverted to give the reflection and transmission coefficients for the modes.

In Figure 3.11, we compare the mode-matching method with the *finite-difference frequency-domain* (**FDFD**) technique [76]. In [12] scattering at MIM junctions was investigated using **FDFD**. It takes relatively few modes for the mode-matching calculations to converge. Without the continuous spectrum, the mode matching results converge to the wrong result. Inclusion of the continuous spectrum decreases the error to around 2%, which is probably due to the space discretization of **FDFD** simulations as well as the method used in the de-embedding of the scattering coefficients from fields. As is also evident from Figure 3.11 the utility of the single mode ($L = R = 1$) mode-matching calculations increases as the dimensions of the waveguides decrease. The single mode approximation is closely related to the simplified impedance model investigated in [12] where it was shown that for deep subwavelength structures impedance models are a good approximation. In Figure 3.11 we also show the effect of neglecting the backward modes in the mode-matching calculations for the $2a = 0.1\lambda$ case. Backward modes

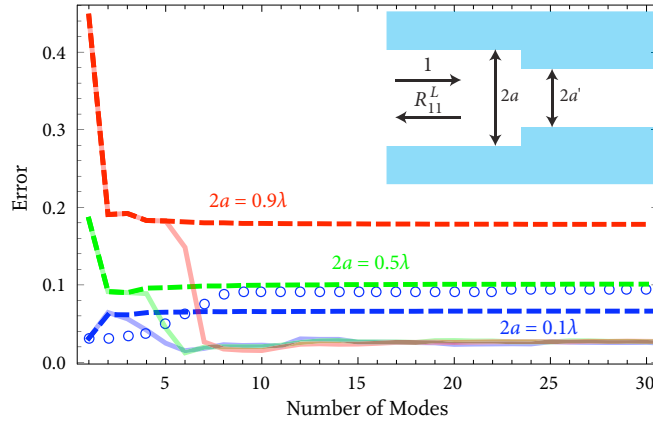


Figure 3.11 – Convergence study of the reflection coefficient, R_{11}^L , of the main mode of the left waveguide traveling toward the right waveguide for $2a = 0.9\lambda$, $2a = 0.5\lambda$ and $2a = 0.1\lambda$. $a'/a = 0.4$ and $\epsilon_m = -143.497 - i9.517$ for all cases. Dashed lines are for calculations including the point spectrum only. Solid lines are those with both the point and the continuous spectrum. Empty circles denote the calculations done with the *forward* point spectrum and the continuous spectrum for the $2a = 0.1\lambda$ case only. Error is defined as $|(R_{11}^{L,\text{MM}} - R_{11}^{L,\text{FD}})/R_{11}^{L,\text{FD}}|$ where MM stands for mode-matching and FD for finite-difference frequency-domain calculations. The inset shows the junction geometry.

are important in this sub-wavelength geometry; however, for the wider geometries of the $2a = 0.5\lambda$ and $2a = 0.9\lambda$ cases we did not observe any increase in the error when backward modes were neglected in the mode-matching calculations.

Analysis of the convergence of the field expansions on both sides of a junction is an important criterion for assessing the validity of the mode-matching technique [77–80]. In Figure 3.12 we show the magnetic field profile at the junction of two MIM waveguides. As is evident from the figure, convergence of the fields on both sides of the junction is obtained only when the continuous spectrum is also taken into consideration. Otherwise, the fields just on the left and just on the right of the junction do not agree with one another, showing one or both calculations to be in error. The clear conclusion from this numerical illustration is that the point spectrum on its own is not sufficient to describe the behavior of the waveguide junctions. Inclusion of the continuous spectrum is essential.

In Figure 3.13 we visualize the scattering coefficient of the main mode of the MIM waveguide. We do the calculations in two different ways, one using FDFD, and the other using the mode-matching technique with the point and the continuous spectrum.

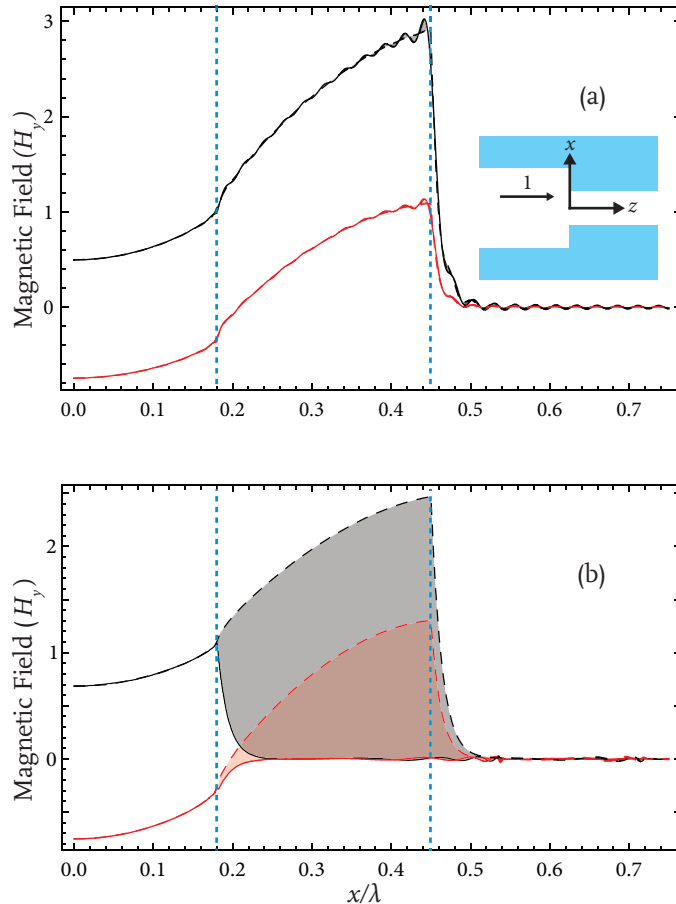


Figure 3.12 – Magnetic field H_y at the junction of two MIM waveguides as a result of the scattering of the main mode of the left waveguide traveling toward the right—the inset shows the schematic of the geometry. The left waveguide has $2a = 0.9\lambda$, the right waveguide has $2a' = 0.36\lambda$ so that $a'/a = 0.4$ as in Figure 3.11. $a + h = a' + h' = 3\lambda/4$. Fields on the left of the junction are dashed, fields on the right are shown with solid lines for both the **real** and the **imaginary** part of the magnetic field profile. The difference between the left and right fields is shaded. Due to symmetry, only half of the field profile is plotted. Vertical dotted lines at $x = 0.18\lambda$ and $x = 0.45\lambda$ denote the end of the insulator region for the right and the left side of the junction respectively. (a) Mode-matching calculations using the point and the continuous spectrum—60 modes in total—showing good agreement between the fields just on the left and just on the right of the junction. (b) Mode-matching calculations using the point spectrum only—100 modes in total—showing clear disagreement between the calculated fields just on the left and just on the right of the junction.

When applying mode-matching, we use the $a > a'$ formulation for R_{11}^L calculations and the $a < a'$ one for R_{11}^R . There is a very good match between the results of the two techniques, verifying the applicability of the mode-matching method.

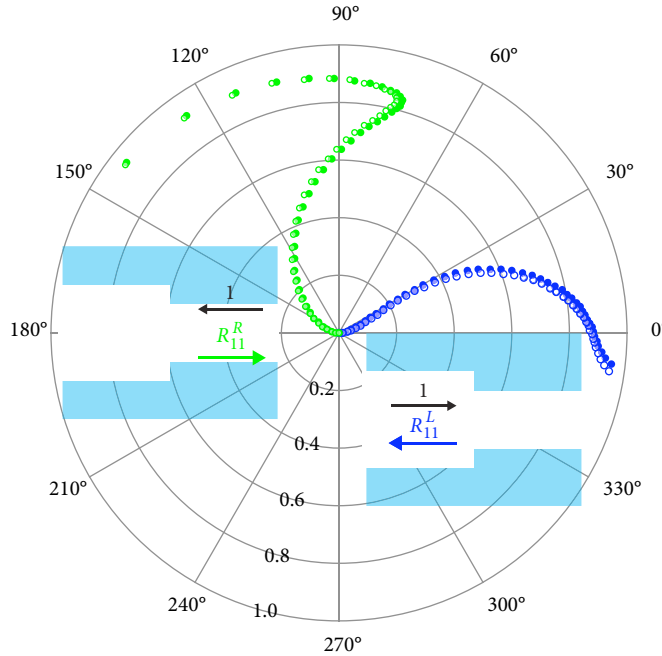


Figure 3.13 – Reflection coefficient of the main mode at the junction between two MIM waveguides of different insulator thicknesses, plotted on the complex plane within the unit circle. Both waveguides have $\epsilon_m = -143.497 - i9.517$ and $\epsilon_i = 1.0$. Filled circles, \bullet , are FDFD results, empty circles, \circ , are mode-matching results. The left waveguide thickness is fixed at $2a = 0.9\lambda$. The right waveguide thickness varies from $2a' = \{0.02\lambda, 0.04\lambda, \dots, 0.9\lambda\}$. The origin is the zero reflection point that corresponds to $a = a'$. As a' decreases progressively toward zero, we move progressively along the curves away from the origin. The **first set of curves**, R_{11}^L , are for the case when the *mode of the left waveguide*, traveling from left to right, is scattered by the junction. The **second set of curves**, R_{11}^R , are for the case when the main *mode of the right waveguide*, traveling from right to left, is scattered by the junction. Insets illustrate the respective cases. Details about the FDFD calculations can be found in [12].

3.5 Discussion

We will begin this section by a comparative study of the modal structures for the parallel plate, the dielectric slab and the MIM waveguides. Our aim will be to frame the MIM case as a bridge between the dielectric slab and the parallel plate waveguides.

The 2D symmetric dielectric slab waveguide—where the cladding and the core are composed of lossless, positive permittivities—has no proper complex modes [57, p. 718] as expected from the regular Sturm-Liouville theory. The dispersion equation for the

dielectric slab waveguide—which is the same as (3.8)—does have complex roots. However, all of those complex roots correspond to leaky modes that are not a part of the spectrum.

The point spectrum of the dielectric slab consists of real propagating modes with pure exponential decay in the cladding region and with positive power flux in the direction of propagation, z . The number of modes in the point spectrum is a finite quantity. The cutoff condition for the point spectrum is obtained by the equality $\kappa_m^2 = 0$. The continuous spectrum of the dielectric slab starts just below the cutoff condition for the point spectrum where $\kappa_m^2 < 0$. In this range, the modes extend to infinity in the transverse direction, but they remain bounded. We can divide the continuous spectrum into two sections based on the sign⁶ of $k_z^2 = \kappa_m^2 + \omega^2\mu_0\epsilon_m = \kappa_m^2 + \omega^2\mu_0|\epsilon_m|$. The section where $k_z^2 > 0$ is called the *radiative part* whereas the section $k_z^2 < 0$ is called the *reactive part* of the continuous spectrum [55, pp. 128–132], [19, pp. 19–28]. For both the radiative and the reactive parts of the continuous spectrum, the transverse field profiles of the modes are sinusoidal standing wave patterns. As the sinusoidal variation in the transverse direction ($\kappa_m = i|\kappa_m|$) becomes more rapid, the sinusoidal variation in the propagation direction (k_z) decreases. The jump from the radiative to the reactive part occurs when the sinusoidal variation in z goes to zero: $k_z = 0, \kappa_m/k_0 = i\sqrt{|\epsilon_m|}$. In the reactive part, the variation in x is so rapid that, modes decay as they propagate in z . The radiative part is often visualized in the mind’s eye by plane waves that originate in the cladding region far away from the core, propagate at an angle towards the core, reflect off of the core and propagate away from it. The interference pattern between the incoming and the outgoing plane waves leads to a standing wave pattern in the transverse direction and a propagating plane wave in the positive z direction. The reactive part is harder to think about in terms of plane wave propagation since in this part of the continuous spectrum k_z is purely imaginary and, therefore, the modes are decaying in the positive z direction. The plane wave picture is often extended to the reactive range by allowing for the possibility for the plane waves to come at an ‘imaginary’ angle of incidence.

The spectrum of the parallel-plate waveguide with PEC boundaries is less nuanced

⁶Here, we are assuming that we are operating at a frequency well above the plasma frequency, ω_p , where $\epsilon_m = |\epsilon_m| < 1$ so that the MIM geometry describes a conventional dielectric slab waveguide as illustrated in the introduction section.

than that of the dielectric slab case. There is no continuous part of the spectrum. All modes belong to the point spectrum and form a discrete basis set. There are infinitely many discrete modes supported by the parallel-plate waveguide. Finitely many of them are propagating modes and carry a positive energy flux in the z direction. The remaining ones do not carry any energy and are called *evanescent*.

The spectrum of the MIM waveguide is a hybrid of the dielectric slab and the parallel-plate waveguides' spectra. The MIM waveguide has both the point and the continuous spectra. Let us start with the continuous spectrum first.

In Section III we have shown that the continuous spectrum of the lossless MIM waveguide exists for all $k_z^2 < \omega^2 \mu \epsilon_m$ which is equivalent to $k_z^2 < -\omega^2 \mu |\epsilon_m|$ since ϵ_m is a large negative number for the MIM case. We see that the continuous spectrum of the MIM waveguide is purely reactive and can be thought of as composed of plane waves coming at an imaginary angle through the metal and reflecting off of the insulator region. Equivalently, at a more fundamental level, they are the solutions of the wave equation with the condition that the fields be finite and non-zero at infinity.

The point spectrum of the MIM waveguide has infinitely many members, similar to the parallel-plate case. Indeed, one can think of the point spectra of the MIM and the parallel-plate waveguides as analytical continuations of each other as illustrated in [22] for the main TM_0 mode of the MIM and the TEM mode of the parallel-plate waveguides. Consequently, the main TM_0 mode of the MIM waveguide can be thought of as the symmetrical coupling of the two surface plasmon modes at the top and the bottom metal-insulator interfaces [81].

There are no evanescent discrete modes in the dielectric slab waveguide, but the MIM waveguide supports them. As illustrated in Figure 3.5 there are infinitely many discrete modes for any given insulator thickness. Finitely many of those are real modes ($k_z^2 \in \mathbb{R}$), the remaining ones are complex ($k_z^2 \in \mathbb{C}$). Of the real modes, only those with $k_z \in \mathbb{R}$ carry any power flux. These observations are strictly true only for the case $\epsilon_m \in \mathbb{R}$. When there is loss in the system, all modes do carry small, yet finite, amount of power.

We have verified these claims by calculating the power flux as

$$\begin{aligned} P &= \frac{1}{2} \operatorname{Re} \left(\int E_x(x) H_y^*(x) dx \right) \\ &= \frac{1}{2} |H_0|^2 \times \operatorname{Re} \left\{ \frac{k_z}{\omega \epsilon_m \operatorname{Re}(\kappa_m)} \frac{1}{\sinh(\kappa_{i\mathbb{R}} d)/\kappa_{i\mathbb{R}} + \sin(\kappa_{i\mathbb{I}} d)/\kappa_{i\mathbb{I}}} + \frac{k_z}{\omega \epsilon_i} \frac{\sinh(\kappa_{i\mathbb{R}} d)/\kappa_{i\mathbb{R}} + \sin(\kappa_{i\mathbb{I}} d)/\kappa_{i\mathbb{I}}}{\cosh(\kappa_{i\mathbb{R}} d) + \cos(\kappa_{i\mathbb{I}} d)} \right\} \end{aligned}$$

using (3.4), (3.7) and $\kappa_i = \kappa_{i\mathbb{R}} + i\kappa_{i\mathbb{I}}$ for different modes in the point spectrum. For waveguide junctions, it has been argued that neglecting complex mode pairs on either side of a waveguide junction leads to a discontinuity in the reactive energy stored at the junctions [72]. A similar argument can also be made for the highly evanescent continuous modes of the MIM geometry. Real and complex bound modes are exponentially decaying in the metal region. At the junction between two MIM waveguides, the smaller waveguide's discrete bound modes cannot account for the field leakage into—and therefore reactive energy storage in—the metal region due their exponential decay. The continuous modes which extend infinitely into the metal region make it possible to account for the leakage into metal regions.

We have shown the necessity to take into account the full modal structure of the MIM waveguide by the calculations we presented in Section IV. Here, we should note that, when we did mode-matching calculations for the lossless MIM geometry, we occasionally observed convergence problems while we were trying to reproduce the FDFD results. However, when we included loss, all our calculations converged and we did reproduce the lossy FDFD results as we have illustrated in Figure 3.13. The matrix that one needs to invert to solve the mode-matching equations has a higher condition number in the lossless case compared to the lossy one. That may explain the difficulties we faced.

In the remainder of this section, we will draw some connections between optics and other branches of science with the hope of expanding the analogical toolset we use for analysis—as exemplified in [82].

The one dimensional Schrödinger equation and the electromagnetic wave equations in layered media are closely related. Both are in the Sturm-Liouville form and one can map the dispersion equation for the TE mode of a dielectric slab waveguide to the dispersion equation for the modes of a finite potential well [83, p. 11]. Furthermore, if one

allows for the finite potential well to have different effective masses in the well and the barrier regions, then a mapping to the TM mode dispersion equation (3.8) also becomes possible. In [84–86] exact closed form analytical solutions for the modes of a single, finite quantum well are developed. These solutions can be mapped to the transverse electric modes of the **MIM** or the dielectric slab waveguides and perhaps with some labor could be expanded to the TM case as well. Effects of discontinuities in quantum well potentials are shown to lead to changes in the reflection spectrum of the wells in [87]. It is intriguing to ask whether such studies could be useful in optics for the investigation of the effects of material interfaces. Recently, it was shown that non-hermitian potentials in the Schrödinger equation can have purely real spectra due to the certain symmetries of the Hamiltonian of the system [88]. Pseudo-hermiticity, which we have touched upon in Section III, has been shown to play an important role in the interpretation of these systems [89]. In [90] a parallel plate waveguide with impedance boundary conditions was analyzed by the help of the definition of an inner product which reveals some hidden symmetries [91, 92] of the system. The operator theoretic findings summarized in [88] can have implications for the analysis of waveguides.

Lastly, in the microwave literature, the unique definition—if there is any—of the impedance of an arbitrary waveguide mode is an active area of research. The causal waveguide impedance definition of [93] seems to formulate a unifying framework to merge different interpretations together. It seems worthwhile to ask what the TM_0 mode impedance of an **MIM** waveguide would be for a causal definition of the impedance given the Kramers-Kronig relationships for waveguide modes as investigated in [94].

3.6 Conclusion

In this chapter we investigated the even TM modes that the **MIM** waveguide supports. We based our analysis in the language of operators and used methods developed for Sturm-Liouville systems to expand the results reported in [36]. The mathematical structure of the odd modes are very similar to the even ones and can be derived in a similar manner. These findings were in accordance with [39] where it was shown that in general, open structures will have complex and continuous spectra.

After the investigation of the modes, we showed their utility and relevance by the mode-matching method. We investigated the problem of modal scattering at the symmetric junction of two MIM waveguides with different cross sections [12] and successfully applied the mode-matching technique to predict the modal reflection coefficients calculated by full-field simulations. Lastly, we commented on some of the possible links between the quantum mechanics, optics and microwave literature and considered possible research directions.

The knowledge of the set of orthogonal modes which form a complete basis for a given geometry leads to a much more simplified algebra and speeds up calculations. The results of this paper are valuable for electromagnetic scattering calculations involving the MIM geometry. Our results would also help in the analysis of optics experiments involving MIM waveguides [95–97]. Furthermore, the results reported are also useful for analyzing plasmonic quantum optics [98–101] and Casimir effect devices [102, 103].

The analysis made in this chapter can be generalized for other related geometries involving metals at optical frequencies [104–107]. The rich set of modes available in the MIM geometry suggests that modal investigation of arbitrary three-dimensional nanometallic waveguides—which are thought to replace the electrical interconnects on future computing devices—will require novel means of deducing their discrete and continuous spectra.

ફુ

Chapter 4

Circuit Theory for MIM Waveguides

4.1 Introduction¹

MODELING ELECTROMAGNETIC WAVE propagation using transmission lines has been one of the most important achievements of microwave network theory [108]. The concept of impedance [109] and understanding the effects of waveguide discontinuities in terms of lumped circuit elements were crucial in this respect.

Recent interest in the use of metals to design optical components opened up the possibility of guiding light in sub-wavelength structures. The optical properties of metals at infrared and visible wavelengths enable these designs. It is hoped that the size mismatch between modern electronic components with critical dimensions on the order of tens of nanometers and the micrometer scaled optical devices will be bridged by the use of nano-metallic structures [10]. Even though the properties of metals are quite different at optical wavelengths compared to the microwave, designs that are qualitatively similar to their low frequency counterparts have been demonstrated at optical frequencies [110]. It is intriguing to ask whether methods from microwaves can be applied to this new generation of nano-metallic structures to come up with concise descriptions of components that can lead to a simplified approach to the design of functional systems composed of many interacting parts.

Transmission lines and lumped element circuit descriptions have been shown to be

¹This chapter is taken from [12]. Copyright 2008 by IEEE.

useful concepts for optical components [76, 111–115]. In this chapter we will focus on the two dimensional *metal-insulator-metal* (MIM) waveguide (here we will use this term “MIM” to apply only to waveguides at optical or infrared frequencies, as distinct from “parallel plate” waveguides, which are mechanically similar structures but used in the microwave or radio-frequency regime). MIM waveguides have been extensively studied [17, 27, 116] in the literature. It has also been shown that the main *transverse magnetic* (TM) mode of an MIM waveguide continuously changes to that of the *transverse electromagnetic* (TEM) mode of a parallel-plate waveguide with *perfect electric conductor* (PEC) boundaries as the frequency of operation is decreased [22]. Our work will investigate the symmetric junctions of MIM waveguides. It is possible to find examples of analysis for various junction geometries including MIM waveguide to free space [30], one MIM waveguide to two MIM waveguides [117], MIM waveguide bends [76, 118], dielectric slab waveguide to MIM waveguide [119], PEC parallel plate waveguide to PEC parallel plate waveguide [120], surface plasmon to surface plasmon [66, 121], and MIM waveguide to MIM waveguide [122]. In [123] junctions made by micro gratings on metallic wires are modeled as Brag mirrors. [124] reviews the numerical methods of analysis for nano-metallic structures.

In this chapter, in Section 4.2, we will characterize the modal reflection and transmission from MIM junctions using the scattering matrix approach, a commonly used method in microwave network theory. Then, in Section 4.3, to test our characterization we will design a cascade connection of MIM junctions to couple the mode of a wavelength sized MIM waveguide to that of a sub-wavelength one with zero reflection. Lastly, in Section 4.4, we will represent the scattering matrix of MIM junctions in terms of an equivalent lumped circuit model and discuss the physical significance of its elements. Throughout our analysis, we will compare MIM waveguides to PEC parallel plate waveguides and comment on the similarities and the differences between the two. We will draw our conclusions in Section 4.5.

4.2 Scattering Matrix Description of Junctions

In this section we will focus on the geometry as shown in Figure 4.1. We are considering MIM waveguides, consisting of two layers of metal separated by an insulating dielectric layer. The metals are presumed to be thick in the vertical (x) direction in Figure 4.1, and to extend arbitrarily far in the directions in and out of the page. We are considering the modes of propagation in the horizontal (z) directions. We are particularly interested in what happens at the symmetric interfaces between two (or more) such MIM waveguides with different dielectric thicknesses. Figure 4.1 shows the interface between two such guides. b will denote the insulator thickness for the left waveguide and b' will be used for right waveguide's insulator thickness. We will assume that the insulating region is free space with a permittivity $\epsilon_i = 1$. For our simulations, the metal is silver with a permittivity of $\epsilon_m = -143.497 - i9.517$ [16, 61], though similar general results are expected for other metals such as aluminum or gold. We will use $e^{+i\omega t}$ for the time dependence of electromagnetic fields where ω is the angular frequency. The wavelength of operation is fixed at $\lambda = 1550\text{nm}$, in the L band of optical telecommunications. The main mode of the system is an even TM mode (here by TM we mean that the magnetic field, H_y , is in the direction out of the plane of the paper in Figure 4.1). Due to the symmetry of the junction only even TM modes can be excited using an incident wave that is itself a TM wave that is an even function with respect to the center of the guide. We therefore have only three field components: H_y , E_x and E_z .

Using the dispersion equation for even modes of the MIM waveguide [116] it can be shown that only a single even propagating mode can exist for $b < 0.97\lambda$ for our choice of ϵ_m , ϵ_i and λ . The condition for the PEC parallel plate waveguide is similar, where only a single even propagation mode exists for $b < 1.0\lambda$. When there is only one propagating mode, far away from the waveguide junction the fields can be written in terms of that main mode of the system since all higher order modes will have an exponential decay much faster compared to the main propagating mode. Under such circumstances, the effects of the waveguide junction on the propagating modes can be described using the single mode *scattering matrix* (S) formalism [125]. In the terminology of the scattering matrix, the forward and backward mode amplitudes are considered to scatter from one

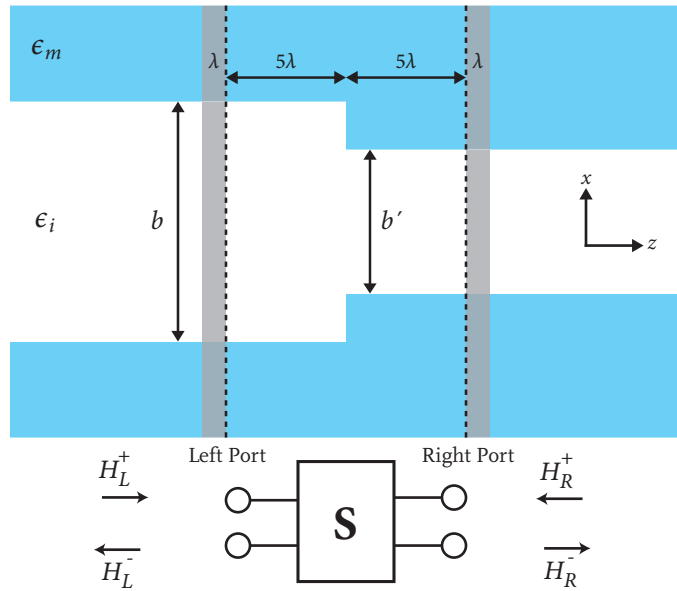


Figure 4.1 – Description of the modeling geometry. Dashed lines represent the location of the left and right ports of the overall scattering matrix \mathbf{S} that describes this junction (schematically shown in the bottom part of the figure). Gray areas on the left and right of the ports are the regions in the simulation space used to extract the reflection coefficients S_{11} and S_{22} .

“port” to another. Here we can think of the ports as being the left and right port planes shown in Figure 4.1. These ports are sufficiently far to the left and right of the junction that the fields have settled down again to being the propagating modes of the guides (nearer to the interface, there will in general be other field behavior, including various near-field components that decay rapidly with distance).

If we can deduce the scattering matrix for such a junction, then we can have a very simple way of modeling the behavior of structures containing such junctions, as is already well known in the modeling of microwave guides. The elements of the scattering matrix, S_{11} , S_{12} , S_{21} , S_{22} , are complex numbers which describe the phase and magnitude of the reflection and transmission of the main modes. Thus, in general there are 8 independent real numbers in \mathbf{S} . However, under certain conditions the number of independent parameters can be reduced. First of all, if the system is composed of reciprocal media (i.e. symmetric permittivity and permeability tensors) then using the Lorentz reciprocity theorem it can be shown that $S_{12} = S_{21}$. Note that this equality implies a

certain normalization of the modes [125, eq. (5.11) and (5.40)], specifically

$$\oint_A \mathbf{E}_L \times \mathbf{H}_L \cdot d\mathbf{A} = \oint_A \mathbf{E}_R \times \mathbf{H}_R \cdot d\mathbf{A} = 1 \quad (4.1)$$

where $\mathbf{E}_{\{L,R\}}$ and $\mathbf{H}_{\{L,R\}}$ denote the electric (\mathbf{E}) and magnetic (\mathbf{H}) components of the main propagating modes on the left (L) and the right (R) of the waveguide junction. \mathbf{A} is the cross section of the waveguides perpendicular to the direction of propagation. Also note that for lossless systems \mathbf{S} is a unitary matrix [125] (though in general in this chapter we will be considering systems with loss). As a result, using reciprocity it is possible to describe a lossy junction using six real numbers, two for each of S_{11} , S_{12} , and S_{22} . When there is no loss we only need three real numbers due to the unitarity of \mathbf{S} .

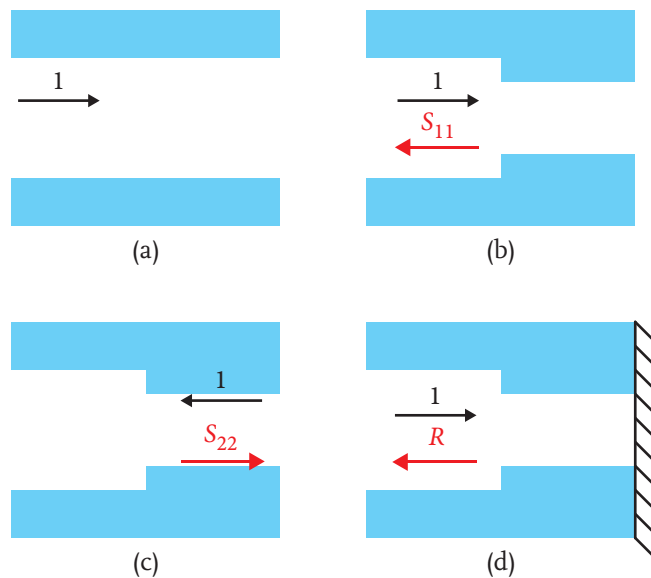


Figure 4.2 – Description of the steps taken in extracting \mathbf{S} from fields. (a) Calibration simulations with uniform insulator widths of b and b' , which give the wave vector k and the values of the incoming fields at the left, $H_L^+ \Psi_L(x)$, and right ports, $H_R^+ \Psi_R(x)$. (b) Field impinging from the left side, which leads to S_{11} . (c) Field impinging from the right side, which leads to S_{22} . (d) Simulation domain is terminated by a perfect electric conductor at the right input port plane. S_{12} is extracted from the reflection coefficient R using the previously calculated S_{11} and S_{22} .

The scattering matrix description based on the propagation of the modes can be mapped to an equivalent transmission line with propagating voltage and current waves.

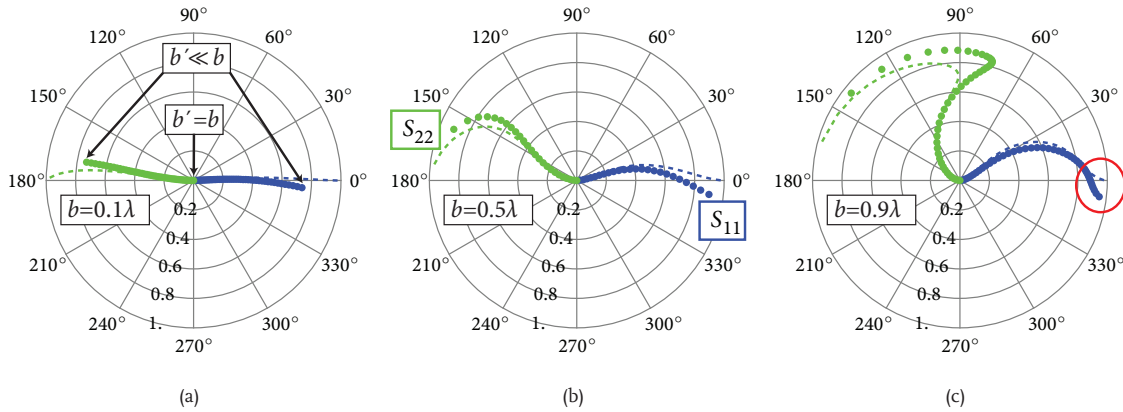


Figure 4.3 – Polar plot of S_{11} (●, plots heading out to the right half of the diagram) and S_{22} (●, plots heading out towards the left half of the diagram) on the complex plane, which is called the Smith chart in the microwave literature. Circles are used for the MIM case, dashed lines are used for the PEC case. Each subplot is for a fixed left waveguide thickness b with a varying right waveguide thickness b' . In all three subplots the origin is the zero reflection point which corresponds to $b' = b$. As b' decreases progressively towards zero, we move progressively along the curves away from the origin. The end points of the dashed curves on the unit circle correspond to $b' = 0$. In all three cases, the wavelength of light is fixed at $\lambda = 1550\text{nm}$. (a) $b = 0.1\lambda$. (b) $b = 0.5\lambda$. (c) $b = 0.9\lambda$.

The voltage, V , on the transmission line is defined as proportional to the transverse electric field of the mode and the current, I , is defined as proportional to the transverse magnetic field. The first condition on the proportionality factors is that the average power is given by $\text{Re}(VI^*/2)$ as in a circuit. The second condition on the proportionality factors is that V/I of an incident wave on the transmission line should be the characteristic impedance of the mode [126, p. 532]. We know that no unique definition of the characteristic impedance can be made for non-TEM modes as shown in [127, p. 66] and [128, pp. 226-228]. However, the normalization condition (4.1) on the modes, which gives us symmetric scattering matrices, automatically leads to transmission lines with characteristic impedance of unity, independent of the modal properties. A discussion and proof of this point is given in [125], [129, pp. 186-188] and [130, p. 171].

After that brief introduction to the theory of scattering matrices, now we will describe the method we used to extract the elements of \mathbf{S} from the electromagnetic fields in such waveguide junctions. We solved Maxwell's equations using the *finite-difference frequency-domain* (FDFD) method [76]. In the vicinity of the waveguide junction, higher

order modes will be excited. We initially chose the left and right ports of our junction sufficiently (5λ) away from the physical junction where the amplitudes of the higher order modes are negligible. In the following we will formulate \mathbf{S} in terms of the transverse magnetic field component H_y . We will use $\Psi_L(x)$ to denote the main mode of the left waveguide and $\Psi_R(x)$ for the right waveguide.

The scattering matrix relates the amplitudes and phases of the modes that arrive at the left and right ports, H_L^+ , H_R^+ to the amplitudes and phases of the modes that propagate away from the ports, H_L^- and H_R^- . Formally we can write

$$\begin{pmatrix} H_L^- \\ H_R^- \end{pmatrix} = \begin{pmatrix} S_{11} & S_{12} \\ S_{21} & S_{22} \end{pmatrix} \begin{pmatrix} H_L^+ \\ H_R^+ \end{pmatrix}. \quad (4.2)$$

In order to extract \mathbf{S} we need to know the fields that arrive at the left and right ports from our numerical sources in the simulation domain. To do that we do two calibration simulations (one for the left waveguide, another for the right waveguide) without any discontinuities, as shown in Figure 4.2(a), and record the fields. This gives us the required $H_{\{L,R\}}^+ \Psi_{\{L,R\}}(x)$ in addition to the propagation vectors, $k_{\{L,R\}}$, of the two main modes for guides of insulator thicknesses b and b' respectively. Then we do two more simulations where we send the mode from the left and from the right waveguide to the discontinuity as schematically shown in Figure 4.2(b)-(c). From the results of the simulation in Figure 4.2(b), for the fields to the left of the left port, $H_L(x, z)$, we get

$$\begin{aligned} H_L(x, z) &= [H_L^+ e^{-ik_L z} + H_L^- e^{+ik_L z}] \Psi_L(x) \\ &= [H_L^+ (e^{-ik_L z} + S_{11} e^{+ik_L z})] \Psi_L(x) \end{aligned}$$

where the location of the left port determines the origin for z and in (4.2) we used the fact that $H_R^+ = 0$ for the simulation depicted in Figure 4.2(b). Simple algebra gives

$$S_{11} = \frac{H_L(x, z)}{H_L^+ \Psi_L(x)} e^{-ik_L z} - e^{-2ik_L z}.$$

Ideally, S_{11} should be independent of the coordinates x and z . However, due to finite reflections from the perfectly matched layers (PML) at the boundaries of our simulation

domain, we do get some small variations in S_{11} . To mitigate these effects, we extract the complex valued S_{11} at various locations in our simulation domain shown with the gray area on the left of the junction in Figure 4.1, and average the results. Very similarly, we also extract S_{22} from the results of the simulation of Figure 4.2(c).

In order to extract S_{12} , we terminate our simulation domain at the plane of the right port with a perfect electric conductor. Such a termination results in zero tangential electric fields and therefore gives -1 for the reflection coefficient of the transverse electric field, E_x , and $+1$ for the magnetic field, H_y . Thus, at the right port we get $H_R^- = H_R^+$. Using this equality in (4.2) gives

$$\begin{pmatrix} H_L^- \\ H_R^- \end{pmatrix} = \begin{pmatrix} S_{11} & S_{12} \\ S_{21} & S_{22} \end{pmatrix} \begin{pmatrix} H_L^+ \\ H_R^+ \end{pmatrix}. \quad (4.3)$$

We call the reflection coefficient from the junction in Figure 4.2(d), R . We extract R using the same method as we used in the extraction of S_{11} . From the definition

$$R = \frac{H_L^-}{H_L^+}$$

and using (4.3) one gets

$$R = S_{11} + \frac{S_{12}S_{21}}{1 - S_{22}} = S_{11} + \frac{S_{12}^2}{1 - S_{22}} \quad (4.4)$$

where in the last equality we used the fact that $S_{21} = S_{12}$. From the knowledge of R , S_{11} and S_{22} one can easily invert (4.4) to calculate S_{12} .

After we calculate \mathbf{S} for the ports defined in Figure 4.1, we shift both the left and right reference planes back to the exact location of the junction using

$$\mathbf{S}_J = \begin{pmatrix} e^{ik_L \ell_L} & 0 \\ 0 & e^{ik_R \ell_R} \end{pmatrix} \mathbf{S} \begin{pmatrix} e^{-ik_L \ell_L} & 0 \\ 0 & e^{-ik_R \ell_R} \end{pmatrix}$$

where $\ell_L = \ell_R = 5\lambda$ as defined in Figure 4.1 and \mathbf{S}_J is the effective scattering matrix for the case where the left and right ports are projected back to coincide with the junction

plane [125]. For the sake of notational abbreviation, from this point on we will use \mathbf{S} to imply \mathbf{S}_J . Note that this effective scattering matrix is defined just for the algebraic convenience of having a scattering matrix associated directly with the position of the interface. The fields near to the interface are not in fact just describable by these single main modes because of various near field effects of higher order modes.

We fixed the frequency of operation at $\lambda = 1550\text{nm}$ and calculated \mathbf{S} for various right waveguide thicknesses (b') while keeping the width of the left waveguide (b) constant. In Figure 4.3 three sets of results are shown for $b = \{0.1\lambda, 0.5\lambda, 0.9\lambda\}$. The outermost circle in the plots is the unit circle in the complex plane, and the real and imaginary parts of the reflection coefficients are plotted for different $\{b, b'\}$ pairs. We also plotted S_{11} and S_{22} as a function of b' for the PEC case using the well known mode-matching technique [62] for the same set of b . We verified our mode matching approach by FDFD which gave the same results. The reason we did mode-matching calculations was to verify the PEC parallel plate waveguide results in the literature, as well as to check our numerical extraction of \mathbf{S} in a numerically independent manner. Making the metals perfect turns the MIM waveguide into the PEC parallel plate waveguide. It can be seen that the shapes of curves for the PEC parallel plate and MIM waveguides are qualitatively similar. Also note that the polar plot of the reflection coefficients is nothing other than the Smith chart of the microwave theory [131, p. 48], which we will use in the next section.

4.3 Cascade Connection of Junctions

Now that we have a methodology to characterize MIM junctions, in this section we will test the utility of the scattering matrix description by numerically simulating mode propagation through a cascade connection of junctions and comparing the results with the predictions of the scattering matrix formalism. First let us define the building blocks that will be used throughout the rest of this section.

When different scattering matrices are cascaded, the overall scattering matrix for

the system is not the product of the individual scattering matrices. For cascade connections, the *transfer matrix*, \mathbf{T} , leads to a much simpler formulation [130, pp. 181-182]. \mathbf{S} has $\{H_L^+, H_R^+\}$ and $\{H_L^-, H_R^-\}$ as an input-output pair, whereas \mathbf{T} has $\{H_R^-, H_R^+\}$ and $\{H_L^+, H_L^-\}$ respectively. Given one representation, one can easily compute the other through simple algebraic manipulations.

$$\begin{pmatrix} H_L^+ \\ H_L^- \end{pmatrix} = \begin{pmatrix} T_{11} & T_{12} \\ T_{21} & T_{22} \end{pmatrix} \begin{pmatrix} H_R^- \\ H_R^+ \end{pmatrix}$$

$$T_{11} = \frac{1}{S_{21}} \quad T_{12} = -\frac{S_{22}}{S_{21}} \quad . \quad (4.5)$$

$$T_{21} = \frac{S_{11}}{S_{21}} \quad T_{22} = S_{12} - \frac{S_{11}S_{22}}{S_{21}}$$

In order to have $H_L^- = 0$, one should have $T_{21}H_R^- + T_{22}H_R^+ = 0$, which can be cast in terms of the scattering parameters using (4.5) as

$$S_{11}H_R^- = (S_{11}S_{22} - S_{12}S_{21})H_R^+. \quad (4.6)$$

4.3.1 Conditions for Zero Reflection

Lossy Case

Let us investigate the case when two junctions characterized by two different scattering matrices, ${}^L\mathbf{S}$ and ${}^R\mathbf{S}$, are separated by a center waveguide of length ℓ as shown in Figure 4.4(a). Suppose that we adjust our excitation amplitude such that the mode that propagates toward the right junction at its input plane, which is the junction plane, has unit strength. That choice of normalization leads to $H_C^- = e^{ik_C\ell}$ and $H_C^+ = {}^R\mathbf{S}_{11}e^{-ik_C\ell}$ where k_C is the wave vector of the center waveguide. With these definitions, the condition for

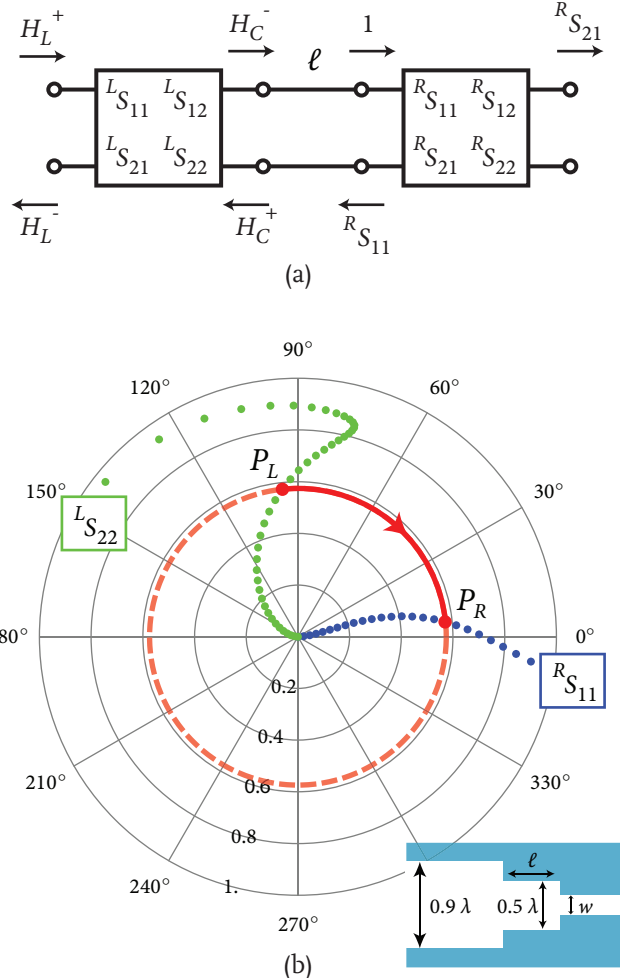


Figure 4.4 – (a) Schematic diagram of modal propagation. The left and right junctions are shown as boxes with an S matrix description. The center waveguide is shown as a transmission line of length ℓ . The source that creates the fields is normalized such that the mode that propagates to the right has a unit magnitude at the input of the right junction. (b) Graphical solution of (4.9) and (4.10) on the complex plane. Point P_L is the location of the left junction on the ${}^L S_{22}$ curve where $b = 0.9\lambda$ and $b' = 0.5\lambda$. Point P_R is the location of the right junction on the ${}^R S_{11}$ curve where $b = 0.5\lambda$ and $b' = 0.16\lambda$.

zero reflection, (4.6), for the left junction can be written as

$$\begin{aligned} {}^L S_{11} H_C^- &= ({}^L S_{11} {}^L S_{22} - {}^L S_{12} {}^L S_{21}) H_C^+ \\ {}^L S_{11} e^{ik_C \ell} &= ({}^L S_{11} {}^L S_{22} - {}^L S_{12} {}^L S_{21}) {}^R S_{11} e^{-ik_C \ell} \\ e^{-2ik_C \ell} &= \frac{{}^L S_{11} / {}^R S_{11}}{{}^L S_{11} {}^L S_{22} - {}^L S_{12} {}^L S_{21}}. \end{aligned}$$

Now, let us simplify the above equality. For reciprocal media, $S_{12} = S_{21}$, we can write

$$e^{-2ik_C\ell} = \frac{^L S_{11} / ^R S_{11}}{^L S_{11} ^L S_{22} - ^L S_{21}^2}. \quad (4.7)$$

Lossless Case

If the system is lossless, then the scattering matrix should be unitary ($SS^\dagger = \mathbf{1}$) which implies the following three conditions

$$\begin{aligned} |S_{11}|^2 &= |S_{22}|^2 = 1 - |S_{12}|^2 \\ \frac{S_{12}}{S_{21}^*} &= -\frac{S_{22}}{S_{11}^*}. \end{aligned} \quad (4.8)$$

Using (4.7) and (4.8) after some algebra the zero reflection condition becomes

$$|^L S_{22}| = |^R S_{11}| \quad (\text{magnitude condition}) \quad (4.9)$$

$$\angle ^L S_{22} + \angle ^R S_{11} = 2k_C\ell + 2\pi n \quad (\text{phase condition}). \quad (4.10)$$

where n is any integer value, superscripts R and L denote right and left respectively. “ \angle ” is used to represent the argument of a complex number. What this means is that, to match a left waveguide to a right waveguide, one should choose a center waveguide width which satisfies the magnitude condition, and decide on the length of the center waveguide based on the phase condition.

As a corollary, suppose that the left and right waveguides are the same and are on the order of a wavelength in dimension. Further suppose that the center waveguide has a deep sub-wavelength size, i.e. it has an insulator width much smaller than the wavelength and the surrounding left and right waveguides' insulator widths. Due to the symmetry of the system, the magnitude condition is automatically satisfied. One only needs to choose a specific length for the center section to do the matching. Such a geometry can be interesting for sensing applications, where interaction with strongly concentrated fields is desired. Similar observations were made in the language of Fabry-Perot resonances for the limiting case when the right and left waveguides' insulator thicknesses go to infinity [30].

Once a matching left, center and right waveguide triplet is found, the procedure can be recursively repeated to cascade more junctions without getting any reflection at the leftmost waveguide.

4.3.2 Mode Converter Design

Now that we have the conditions (4.7) and (4.9)-(4.10) for zero reflection, we can test their validity. Condition (4.7) is more general and is applicable to the lossy case. We did a series of simulations in which we extracted \mathbf{S} for a hypothetical loss-less metal with a real, negative permittivity $\epsilon_m = -143.497$. The results were very similar to the case in Figure 4.3 where the loss was included. That led us to suspect that the conditions for the lossless reciprocal junctions, (4.9) and (4.10), would be essentially sufficient in the design of a mode converter that converts the mode of a wavelength sized MIM waveguide ($b = 0.9\lambda$) to that of a sub-wavelength one with no reflection.

In our design we choose the left waveguide width to be 0.9λ and the center waveguide width to be 0.5λ as shown in the inset in Figure 4.4(b). The parameters that we need are the insulator width of the right waveguide, w , and the length of the center waveguide, ℓ .

The width of the right waveguide can be chosen by satisfying (4.9). In Figure 4.4(b) P_L is the location of the $b = 0.9\lambda$ to $b' = 0.5\lambda$ junction on the ${}^L S_{22}$ curve. To satisfy (4.9) we need to have $|{}^L S_{22}| = |{}^R S_{11}|$. The solution can be graphically found by drawing a circle in the complex plane with a radius $|P_L|$ centered at the origin and finding its intersection with the ${}^R S_{11}$ curve. The intersection point is denoted by P_R . P_R corresponds to a right waveguide thickness of 0.16λ . The phase condition (4.10) is then easily calculated from the phases of the scattering coefficients, $\angle P_L$ and $\angle P_R$. After some simplification through the use of the numerical value for k_C one gets $\ell/\lambda = 0.1377 + 0.4861n$, where n is any positive integer.

To check our design, we numerically simulated the structure shown in the inset of Figure 4.5 using FDFD and looked at the amount of power reflected back as a function of the center waveguide length ℓ . We also calculated the power reflection coefficient through the use of the transfer matrix formalism in which we multiplied the transfer

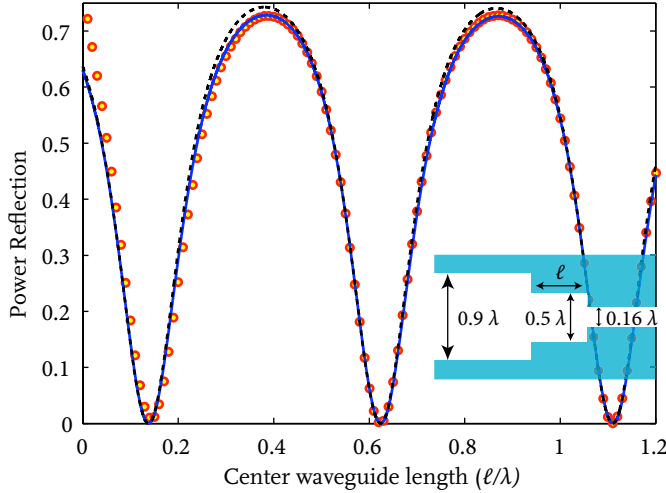


Figure 4.5 – Test of the scattering matrix description. Horizontal axis is the length of the center waveguide normalized to λ . Vertical axis is the power reflection coefficient. FDFD simulation results (●), transfer matrix calculations using lossy junctions (solid line) and lossless junctions (dashed line) are also plotted. Transfer matrix calculations do take into account the loss in the center waveguide for both cases. As the junctions get very close to each other ($< 0.1\lambda$) transfer matrix model begins to break down due to higher order modal interactions.

matrices for the right junction, \mathbf{T}_R , a center waveguide of length ℓ , \mathbf{T}_C , and the left junction, \mathbf{T}_L , to get the overall transfer matrix $\mathbf{T} = \mathbf{T}_L \mathbf{T}_C \mathbf{T}_R$, and plotted $|T_{21}/T_{11}|^2$ of \mathbf{T} as a function of ℓ/λ . We did the calculations for two different sets of $\{\mathbf{T}_R, \mathbf{T}_L\}$: one in which we used the scattering matrices for the lossy junctions and another for the lossless junctions. The center waveguide of length ℓ had loss in both cases i.e. $k_C = (1.03 - i9.45 \times 10^{-4})2\pi/\lambda$.

Figure 4.5 verifies that lossless junction models are quite effective at modeling the waveguide discontinuities and the prediction of the length of the center guide for zero reflection reached by their use, $\ell/\lambda = 0.1377 + 0.4861n$ is very accurate. The lossy junction model on the other hand gives results essentially indistinguishable from the simulation results as long as the two junctions are not very close to each other ($< 0.1\lambda$). When the junctions get very close, the coupling of higher order non-propagating modes becomes important and the single mode modeling we employed in the construction of scattering matrices breaks down. For such closely spaced junctions, the whole structure should be treated as a single unit and its characteristics should be extracted by the

techniques described in Section 4.2.

Lastly, (4.9)-(4.10) reproduces the well known quarter wave ($\lambda/4$) impedance matching formula used at *radio frequencies (RF)* [130, Sec. 5.6] where one uses

$$\begin{aligned}-^L S_{11} &= {}^L S_{22} = (Z_{0C} - Z_{0L})/(Z_{0C} + Z_{0L}) \\ -^R S_{11} &= {}^R S_{22} = (Z_{0R} - Z_{0C})/(Z_{0R} + Z_{0C}).\end{aligned}\quad (4.11)$$

In the equation above $Z_{0\{L,C,R\}}$ denotes the characteristic impedance of the left, center and right RF transmission line. Solution of (4.9)-(4.10) with (4.11) and either the condition $Z_{0R} > Z_{0C} > Z_{0L}$ or $Z_{0R} < Z_{0C} < Z_{0L}$ gives

$$Z_{0C} = \sqrt{Z_{0L}Z_{0R}} \quad \text{and} \quad \ell = \frac{\lambda}{4} + n\frac{\lambda}{2} \quad (4.12)$$

where n is any positive integer. Recently, a power transmission of 86% for a waveguide converter designed using (4.12) was demonstrated [122].

4.4 Circuit Model for the Waveguide Junction

So far, we have characterized the MIM junctions and with that characterization designed a waveguide matching section by the use of the scattering matrices. Another important approach in microwave waveguide modeling is the use of equivalent circuit models, which can give an intuitive picture of the system as well as allowing the use of circuit simulators for design.

Here we relate the scattering matrix and circuit models, and show simplified circuit models that can characterize the MIM waveguide interfaces. Since we only have single propagating modes in the guides we consider, we can also use equivalent transmission lines to describe the propagation between interfaces. Taking these circuit and transmission line approaches together, we can then model a broad range of MIM systems in circuit models.

There is no unique way to describe \mathbf{S} using lumped circuit elements [132, p. 316]. To choose one circuit out of the infinite possible set that could correspond to the same

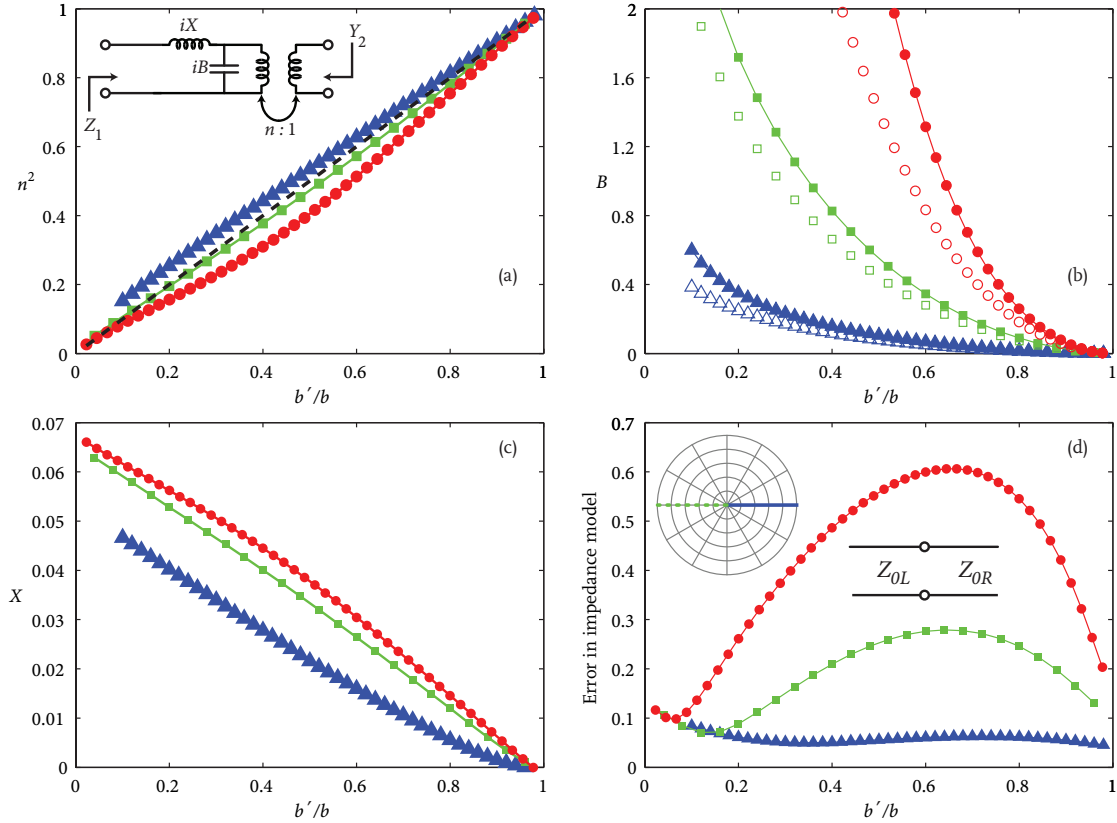


Figure 4.6 – Circuit description of the lossless ($\epsilon_m = -143.497$) waveguide junction for $b = 0.1\lambda$ (\blacktriangle), $b = 0.5\lambda$ (\blacksquare), $b = 0.9\lambda$ (\bullet) (a) Square of the turns ratio, n^2 , which is equivalent to the impedance ratio at the terminals of the transformer. Dashed line is the PEC result described by (4.14). Inset shows the circuit diagram. (b) Susceptance, B , for the MIM (\blacktriangle , \blacksquare , \bullet) and the PEC (\triangle , \square , \circ) case. B for the PEC case plotted by the use of (4.13). (c) Reactance, X , of the MIM waveguide. $X = 0$ for the PEC parallel plate waveguide. (d) Error in S_{11} defined as $|(S_{11} - S'_{11})/S_{11}|$ where S_{11} is the exact solution, $-S'_{11} = (Z_{0R} - Z_{0L})/(Z_{0R} + Z_{0L})$ is the characteristic impedance model approximation. Inset on the upper left corner shows the implication of the characteristic impedance model on the Smith Chart where S_{11} (solid line in the inset) and S_{22} (dashed line in the inset) have a π phase shift. Compare with Figure 4.3. The error is around 5 percent for $b = 0.1\lambda$ where the π phase shift condition is approximately satisfied. As the dimensions increase so does the error.

S, we will first look at the well studied PEC case. After reproducing the PEC results, we will then add another term to the PEC parallel plate waveguide model to account for the properties of metals at optical frequencies. We will compare the lumped circuit representation with the characteristic impedance models in the literature. At the end of the section we will justify our choice of the additional circuit element, while we give

a physical explanation for the circuit.

4.4.1 Exact Model

We will begin our analysis with the PEC case. The solution to the scattering problem for the junction of two PEC parallel plate waveguides was developed and experimentally verified [133]. It consists of a capacitor with susceptance B and a transformer with a turns ratio of $n : 1$. The susceptance and the turns ratio are described in terms of the geometry of the junction. The susceptance value is given by

$$B = \frac{2b}{\lambda} \left\{ \log \left[\left(\frac{1 - \alpha^2}{4\alpha} \right) \left(\frac{1 + \alpha}{1 - \alpha} \right)^{\frac{1}{2}(\alpha+1/\alpha)} \right] + 2 \frac{A + A' + 2C}{AA' - C^2} + \left(\frac{b}{4\lambda} \right)^2 \left(\frac{1 - \alpha}{1 + \alpha} \right)^{4\alpha} \left(\frac{5\alpha^2 - 1}{1 - \alpha^2} + \frac{4}{3} \frac{\alpha^2 C}{A} \right)^2 \right\} \quad (4.13)$$

where $\alpha = b'/b$ and

$$\begin{aligned} A &= \left(\frac{1 + \alpha}{1 - \alpha} \right)^{2\alpha} \frac{1 + \sqrt{1 - \left(\frac{b}{\lambda} \right)^2}}{1 - \sqrt{1 - \left(\frac{b}{\lambda} \right)^2}} - \frac{1 + 3\alpha^2}{1 - \alpha^2} \\ A' &= \left(\frac{1 + \alpha}{1 - \alpha} \right)^{\frac{2}{\alpha}} \frac{1 + \sqrt{1 - \left(\frac{b'}{\lambda} \right)^2}}{1 - \sqrt{1 - \left(\frac{b'}{\lambda} \right)^2}} + \frac{3 + \alpha^2}{1 - \alpha^2} \\ C &= \left(\frac{4\alpha}{1 - \alpha^2} \right)^2. \end{aligned}$$

The square of the turns ratio of the transformer is equal to

$$n^2 = \frac{b'}{b}. \quad (4.14)$$

It is worthwhile remembering that the primary-secondary turns ratio of the transformer, $n : 1$, is also the ratio of the voltages at its terminals. From the conservation of power, currents have the inverse ratio and as a result the impedance ratio at the transformer

terminals is $n^2 : 1$.

The derivation of the circuit elements for the PEC case can be found in [134], [135] and [129]. The technique used is to find an approximate analytic solution to the static limit of the scattering problem, and then to use the approximate solution as a basis for further calculations with the variational principle [134, p. 107].

Note that for the PEC case, only two parameters, B and n , are sufficient to describe the junction even though in general three parameters are required for a lossless reciprocal system. The non-dispersive nature of the main mode of PEC parallel plate waveguides leads to a further symmetry in the junction which reduces the number of circuit parameters required.²

At optical frequencies where the modes are strongly dispersive, a third circuit element is needed in order to be able to fit the elements of \mathbf{S} exactly. For that reason we have an inductor term with a reactance X . A schematic of the circuit diagram is shown in the inset of Figure 4.6(a). The PEC parallel plate waveguide circuit is the same, with $X = 0$. The normalization that we defined in (4.1) leads to transmission lines with a unit characteristic impedance on both sides of the junction. From transmission line theory we get the following equalities in terms of the equivalent impedance looking from the left side of the circuit, Z_1 , and the equivalent admittance looking from the right side, Y_2

$$-S_{11} = \frac{Z_1 - 1}{Z_1 + 1} \quad \text{and} \quad -S_{22} = \frac{1 - Y_2}{1 + Y_2} \quad (4.15)$$

where

$$\begin{aligned} Z_1 &= iX + \frac{1}{iB + \frac{1}{n^2}} \\ Y_2 &= \left(\frac{1}{1 + iX} + iB \right) n^2. \end{aligned} \quad (4.16)$$

²One way to check this is by observing the failure of [134, p. 103, eq. (14)] for modes with k values that depend on b which implies that more than two parameters are required. Conversely, numerically calculating the determinant of the impedance matrix [125, p. 216], \mathbf{Z} , as suggested in [133, Ch. 3, p. 119] shows that indeed only two parameters are sufficient for the PEC case. We also verified using FDFD that (4.13) and (4.14) very precisely represent the PEC junction.

The reason why we have negative signs in front of S_{11} and S_{22} in (4.15) is because we defined \mathbf{S} based on the transverse magnetic component of the main mode, H_y . However, the norm in circuit parametrization is to use the voltage reflection and transmission coefficients, which correspond to a scattering matrix description for the transverse electric component, E_x . Just as in transmission line theory where the reflection coefficient for voltage is the negative of that of the current, the same relationship also holds exactly between the reflection coefficients of E_x and H_y .

We can calculate Z_1 and Y_2 from \mathbf{S} via (4.15)

$$Z_1 = \frac{1 - S_{11}}{1 + S_{11}} \quad , \quad Y_2 = \frac{1 + S_{22}}{1 - S_{22}}. \quad (4.17)$$

Rewriting (4.16) in terms of its real and imaginary parts gives

$$\begin{aligned} Z_1 &= \frac{\frac{1}{n^2}}{B^2 + \frac{1}{n^4}} + i \left(X - \frac{B}{B^2 + \frac{1}{n^4}} \right) \\ Y_2 &= \frac{n^2}{1 + X^2} + i \left(n^2 B - \frac{n^2 X}{1 + X^2} \right). \end{aligned} \quad (4.18)$$

Now let the real and imaginary parts of Z_1 and Y_2 be denoted as $Z_R = \text{Re}(Z_1)$, $Z_I = \text{Im}(Z_1)$, $Y_R = \text{Re}(Y_2)$ and $Y_I = \text{Im}(Y_2)$. Using (4.18) we get

$$\begin{aligned} Z_1 &= Z_R + iZ_I = Z_R + i(X - Bn^2 Z_R) \\ Y_2 &= Y_R + iY_I = Y_R + i(Bn^2 - XY_R) \end{aligned}$$

and we therefore have

$$\begin{aligned} Z_I &= X - Bn^2 Z_R \\ Y_I &= Bn^2 - XY_R. \end{aligned} \quad (4.19)$$

Inverting (4.19) gives

$$Bn^2 = \frac{Y_I + Y_R Z_I}{1 - Y_R Z_R} \quad \text{and} \quad X = \frac{Z_I + Z_R Y_I}{1 - Y_R Z_R}. \quad (4.20)$$

Once we know Bn^2 and X , we can calculate n^2 using (4.18) as

$$n^2 = Y_R(1 + X^2) = Z_R [1 + (Bn^2)^2]. \quad (4.21)$$

Using equations (4.17), (4.20) and (4.21) one can calculate the circuit parameters from S_{11} and S_{22} . In Figure 4.6(a)-(c) we plotted n^2 , B and X as a function of b'/b for the three different fixed b values of 0.1λ , 0.5λ and 0.9λ . Due to the negligible effect of loss on junction characteristics, Figure 4.3 and Figure 4.6(a)-(c) carry the same information, shown in different formats. It can be seen that the PEC circuit description and the MIM circuit description lead to parameters which qualitatively have similar behaviors.

4.4.2 Simplified Model

Until now, the specific normalization we imposed on the modes (4.1) mapped the modal propagation of waves into equivalent transmission lines of unit characteristic impedance. In this section we will investigate the applicability of another characteristic impedance definition for the MIM junctions. The definition we use for the characteristic impedance of an MIM waveguide of insulator thickness b is [76]

$$Z_0 = b \frac{k}{\omega \epsilon_i}. \quad (4.22)$$

Note that, this new definition is a mere rescaling of what we mean by voltage and current of the equivalent transmission line, and such a redefinition does not change S_{11} and S_{22} but breaks the symmetry of \mathbf{S} and therefore $S_{12} \neq S_{21}$ [130, pp. 199-200, prb. 4.15].

From transmission line theory one can calculate the current reflection coefficients of the junction of two transmission lines with different characteristic impedances on the right, Z_{0R} , and on the left, Z_{0L} , as

$$-S_{11} = S_{22} = \frac{Z_{0R} - Z_{0L}}{Z_{0R} + Z_{0L}}. \quad (4.23)$$

The simplified characteristic impedance model based on (4.22) and (4.23) implies a π phase shift between S_{11} and S_{22} . We schematically plotted (4.23) on the Smith chart as

an inset in Figure 4.6(d). Comparison of the inset and Figure 4.3 shows that the π phase shift condition is more and more satisfied as the waveguide dimensions are decreased to sub-wavelength dimensions. Figure 4.6(d) also supports this observation; error in the approximate reflection coefficients of (4.23) decreases as the waveguide dimensions become deep sub-wavelength. The characteristic impedance model is valid and useful when the structure is small in comparison with the wavelength, so that the quasi-static approximation holds.

4.4.3 Interpretation of Circuit Models

In the PEC limit where there is no dispersion in the main modes, the ratio of characteristic impedances Z_{0R}/Z_{0L} as defined in (4.22) limits to n^2 (4.14). Therefore, the transformer in the exact model can be associated with the different characteristic impedances on the two sides of the junction.

As the dimensions of the PEC parallel plate junction are scaled up, the importance of the susceptance term, B , increases. This is a sign of the increased influence of the higher-order modes on the junction characteristics. B signifies the effect of the higher order non-propagating modes, excited in the vicinity of the junction, on the main propagating modes. B for MIM waveguide is higher than that of PEC parallel plate waveguide with the same insulator dimensions. We observed that using $b_s = \alpha b$, $b'_s = \alpha b'$ as the left and right waveguide insulator thickness in (4.13) for $\alpha = \{1.08, 1.2, 1.4\}$ corresponding to the $b = \{0.9\lambda, 0.5\lambda, 0.1\lambda\}$ cases gave good fits to the MIM waveguide solutions plotted in Figure 4.6(b). The dispersive nature of the MIM waveguide mode and the finite penetration of fields into the metal regions, which leads to a larger effective insulator thickness, can explain the differences in B for the MIM case [76].

The MIM junction, with its predominantly negative ϵ_m at infrared frequencies, requires an additional circuit term, an inductor with reactance X , to fully describe the junction scattering characteristics (S) using circuit terminology. We can qualitatively justify the existence of X by investigating the properties of S_{11} in the limit $b' \rightarrow 0$. We see that for the PEC case, S_{11} limits to +1 as highlighted in Figure 4.3(c). This is in line with the fact that $B \rightarrow \infty$ and $n \rightarrow 0$ as $b' \rightarrow 0$ which leaves us with a short circuit for

the PEC case (Figure 4.7). On the other hand, for the MIM case S_{11} limits to a value with magnitude close to unity, but with a non-zero phase in the fourth quadrant of the complex plane. In order to have this behavior, the limit of X should be non-zero since both the MIM and PEC cases have the same limits for B and n . From Figure 4.6(c) we can see that indeed X limits to a non-zero value as $b' \rightarrow 0$.

It is possible to associate an effective surface reactance $X_s = i\omega L_e$ with planar metal surfaces where L_e is the kinetic electronic inductance that electrons experience according to the Drude model [136].³

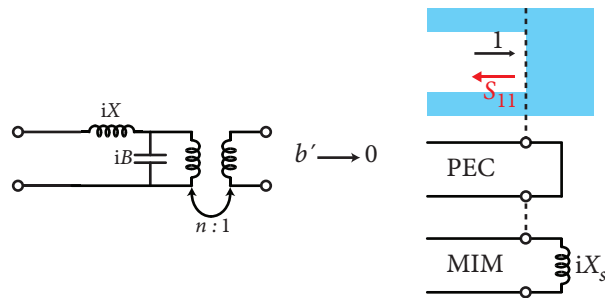


Figure 4.7 – Circuit models in the limit where the right waveguide width (b') goes to zero. For the PEC parallel plate waveguide, the reflection coefficient for currents is unity. For the MIM waveguide, the reflection coefficient has a small negative phase as is evident from Figure 4.3(c). Surface reactance of metals at optical frequencies has an inductive character. Investigation of the limit $b' \rightarrow 0$ leads us to associate the inductor in our circuit model with the normalized surface reactance of the vertical metal surfaces at the MIM junction of total length $b - b'$ as shown in Figure 4.1.

In Figure 4.7 we schematically describe the $b' \rightarrow 0$ limit for the PEC and MIM junctions. From the circuit model we see that

$$\begin{aligned} {}^{\text{PEC}} S_{11} &= \frac{1 - 0}{1 + 0} = 1 \\ {}^{\text{MIM}} S_{11} &= \frac{1 - iX'_s}{1 + iX'_s} \cong 1 - i2X'_s \end{aligned}$$

where $X'_s \ll 1$ represents the surface reactance term normalized with respect to the left waveguide's characteristic impedance. In order to have a consistent description of the junction, we should have $X = X'_s$ when $b' = 0$. This limiting behavior allows us to associate X with the effective normalized surface reactance of the perpendicular

³Note that [136] uses the $e^{-i\omega t}$ convention which leads to $X_s = -i\omega L_e$.

metal section of height $b - b'$ at the junction. A back-of-the-envelope calculation with $X_s \approx b\sqrt{\mu_0/\epsilon_m}$ and Z_{0L} as defined in (4.22) gives⁴ $X'_s \approx X_s/Z_{0L} \approx \{0.082, 0.081, 0.074\}$ for the $b' \rightarrow 0$ limit of $b = \{0.9\lambda, 0.5\lambda, 0.1\lambda\}$ cases. Comparing these values to the corresponding X values in Figure 4.6(c) shows that this calculation correctly predicts the order of magnitude of X'_s .

Our association of the circuit elements of the junction with physically more familiar concepts does not necessarily make any of the calculations easier. One still needs to do full wave simulations to extract the highly coupled B , X and n^2 parameters. Furthermore, our analysis was based on a variation of the geometry while keeping the frequency of operation fixed. Due to the highly dispersive nature of the refractive index of metals at optical frequencies, we expect that a frequency based analysis near the resonance points of material dispersion characteristics will lead to the observation of interesting phenomena at junction geometries. Such studies can be the subject matter of future investigations. Nevertheless, we believe that the lumped circuit model at 1550 nm is valuable in developing a more intuitive understanding of modal scattering at MIM junctions, and it allows a circuit-based analysis of complex systems of guides.

4.5 Conclusion

In this chapter we investigated the properties of infrared light propagation in MIM waveguides at 1550 nm by concentrating on the symmetric junctions between waveguides of different dimensions. We applied techniques widely used in the microwave literature to characterize the MIM junctions. We used a numerical method to extract the scattering matrices of junctions of different geometries from full field solutions. We validated our characterization by designing a mode converter that concentrates light from an MIM waveguide of wavelength sized dimension to one of sub-wavelength dimension with zero reflection.

We parametrized the scattering matrix of the MIM junction in terms of lumped circuit elements to come up with a more physical picture of the junction properties. The

⁴ $\sqrt{\mu_0/\epsilon_m}$ (where μ_0 is the permeability of free space) is the surface impedance of a metallic half space which is also equal to the intrinsic impedance of the metallic medium [137].

circuit representation of the junction helps us associate the effects of geometry, material properties and wave propagation in terms of a simple network of a capacitor, inductor and a transformer. The scattering matrix description of junctions can be used to design optical circuitry with complex functionality using tools of circuit analysis [138, 139]. It is conceivable to build a library of junction geometries associated with their scattering matrices for different waveguides including three dimensional nano-metallic ones [140]. Such a library, indexed according to modal scattering and propagation properties, would be invaluable in the design of integrated optical circuits composed of many interacting components.

Chapter 5

Fundamentals of Antennas

5.1 Introduction

RESEARCH IN electromagnetic radiators bloomed during the Second World War era. Great sums were spent on organizing scientific research towards winning the war. Among the many different military applications of science—from nuclear weapons to cryptography—the microwave theory led to an especially useful tool: radar. The MIT Radiation Lab was the center of research activity. After the war ended, a 28 volume treatise on microwave theory was published, called *MIT Radiation Laboratory Series*. The series covered a wide range of topics. Of special interest to us in this chapter is volume 12, *Microwave Antenna Theory and Design* [141].

In the previous chapters, we have seen how to analyze waveguiding geometries based on the modes that they support. This chapter will focus on radiating structures, namely antennas. We will outline the basics of antenna theory and then talk about methods of analyzing antennas to be used at optical frequencies. We will begin by going through the antenna theory for perfect metals—a good approximation for microwave frequencies. Then, we will look at antennas as scatterers and will analyze them using analytical and numerical methods. Lastly, we will describe the intricacies of designing an integrated antenna/detector structure.

5.2 Basics of Antenna Theory

In chapters three and four, we have talked about the details of modal propagation in waveguides. In this section, we will make use of some of our results, and have a qualitative look at the radiation problem.

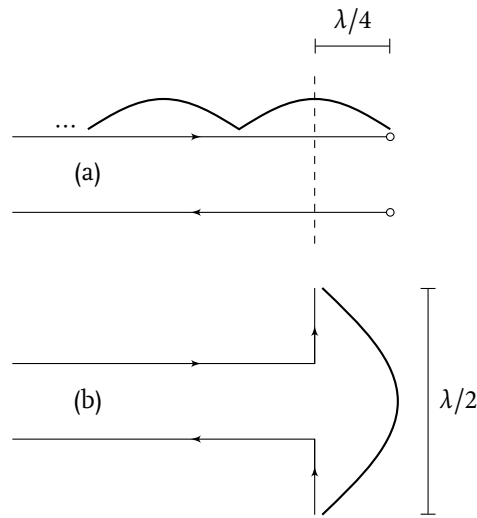


Figure 5.1 – Transition from a transmission line to a radiating antenna. Arrows denote the direction of current.

If Figure 5.1(a) we show a sketch of a transmission line with an open circuit termination. At the plane of termination, current will be zero and the voltage value will be a maximum, leading to a current reflection coefficient of -1 and a voltage reflection coefficient of $+1$. Further away from the plane of termination, due to the interference of incoming and reflected waves, a sinusoidal current pattern will form.

If we bend the ends of transmission line right at the point where the current is a first maximum, we arrive at the canonical $\lambda/2$ dipole antenna. In Figure 5.1(b) we show the equivalent current pattern of the half wave dipole. Each arm of the half wave dipole is of length $\lambda/4$, and the current maximizes at the center of the dipole.

We can calculate the far-field radiation pattern of a half wave dipole by integrating the current at a given spherical direction (θ, ϕ) . Due to the azimuthal symmetry, there

will not be any ϕ dependence. In the θ direction it can be shown that [142, p. 167]

$$E_\theta \propto \frac{\cos[(kL/2)\cos(\theta)] - \cos(kL/2)}{\sin(\theta)}$$

where k is the wave vector of the fundamental mode of the transmission line. $kL = \pi$ is the first resonance point, and the radiation pattern for that case is plotted in Figure 5.2.

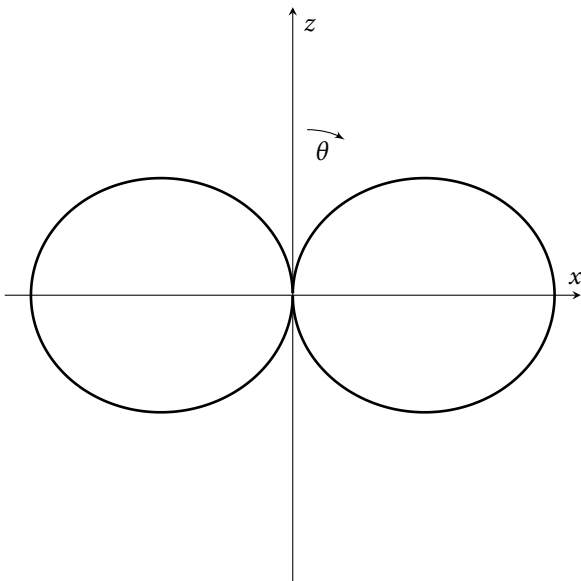


Figure 5.2 – Theoretical radiation patterns of the half-wave dipole antenna.

The first resonance point of the antenna is intimately related to the feeding transmission line. If the transmission line main mode is free of dispersion—i.e. the first mode has a TEM like character—then, the total physical length of the antenna will be half the free space wavelength, $\lambda/2$. However, when there is dispersion, i.e. wavelength within the waveguide is *shorter* than the free space wavelength, then, a resonance will be observed for lengths shorter than $\lambda/2$. Or, equivalently, for a fixed total length, resonance frequency will decrease, i.e. redshift.

In the following sections, we will substantiate the qualitative picture drawn above with more quantitative calculations. It should be noted, however, that what we have shown so far neglects the details of the coupling from the transmission line to the radiating antenna element. We have made simplifying assumptions about the nature of the modal propagation—which may or may not hold true. For instance, antenna

impedances are usually defined with respect to a TEM mode propagating within a transmission line connected to the radiating structure. In the optical domain, the validity of such an approximation should be carefully studied. Furthermore, antenna impedance depends on the way that the antenna is connected to the waveguiding geometry even for radiowave frequency antennas [143, p. 39]—certainly, similar effects will be importance at the optical frequencies. In [143, Appendix III], various different analytical formulations of the dipole antenna impedance are provided. However, as pointed out in [143, Appendix III, p. 466]

From a practical point of view the antenna impedance is the input impedance measured several half-wavelengths away from the antenna, so that the voltage and current on the line are those due to the incident and reflected TEM modes.

The above observation hints that a unique antenna impedance definition would be associated with the waveguide with which the antenna is supposed to be working with. For the dipole antenna case, most of the models assume a coaxial cable connected at the center feed point of the dipole. However, it is not certain whether or not the same antenna models would be useful if, say, a microstrip waveguide were to be used to excite the antenna. Likewise, generalization to optical frequencies requires one to figure out (a) what the best wave guiding mechanism to use for the application of interest is, and (b) given the waveguide geometry and the fundamental mode that is supported by it, how the interactions between the main mode and radiating elements can be concisely represented through the use of circuit models. Further justification for these thoughts can be found in [141, p. 38]

Microwave lines are, in fact, generally so designed that they can support free propagation of only one mode. Nevertheless, though a single mode is incident on the antenna, the antenna itself excites other modes, in addition to giving rise to a reflected wave in the incident mode. It is only at points so far from the antenna that the other modes have been attenuated to negligible amplitudes that a waveguide is equivalent to a two-wire line.

Therefore, during the rest of the chapter, we will treat antennas as scatterers and look at their interaction with electromagnetic waves propagating in modes of the free-space, i.e. plane waves. We will focus our attention on the free-space problem, but it is

worthwhile underlining the importance of coming up with concise representations of antenna-waveguide coupling geometries so as to be able to couple light energy into devices designed to work in plasmonic waveguides as in [144].

5.3 Antennas as Scatterers

Due to the duality of Maxwell's equations, antennas can be treated either as receiving or radiating structures and the two descriptions are closely related to each other. Because of our interest in using optical antennas to design improved photo-detector systems, from now on we will treat the antennas in the receiving case¹ and in this section we will provide some of the techniques for analyzing electromagnetic scatterers of various types.

5.3.1 Mie Theory

Exact calculation of the scattering of electromagnetic waves by a sphere was one of the important theoretical challenges of classical physics of the early 20th century. Gustav Mie²—who was interested in the scattering properties of gold colloidal particles in water—was one of the first people to solve the problem [14, p. 82]. Therefore we will use his name in this section for our analysis of one of the few exactly solvable three dimensional scattering problems: the scattering of a plane wave by a sphere. In order to be consistent with other literature on the topic, we will use the $\exp(-i\omega t)$ convention.

The geometry that we will investigate is as shown in Figure 5.3. The incident plane wave is polarized in the \hat{x} direction. We will start by expanding the plane wave in the *vector* spherical harmonics. The vector spherical harmonics are closely related to the

¹On the other hand, if we were to be interested in using antennas in a waveguide geometry, then it would make more sense to treat the antennas as radiating elements which couple the mode(s) of a given waveguide to those of the free-space modes. For instance, it would be far more effective to calculate the radiation pattern of an antenna-waveguide geometry if one looks at the radiated fields rather than sending plane waves at various directions individually and calculating their coupling efficiency into the main mode of the waveguide geometry.

²See [145] for a brief biography of Mie.

scalar spherical harmonics defined as

$$\psi_{emn} = \cos(m\phi)P_n^m(\cos\theta)z_n(kr)$$

for the even, hence the subscript ‘e’, case and

$$\psi_{omn} = \sin(m\phi)P_n^m(\cos\theta)z_n(kr)$$

for the odd, hence the subscript ‘o’, case. Here z_n denotes an appropriate combination of the linearly independent solutions of the radial part of the wave equation $(\nabla^2 + k^2)\psi = 0$ —namely, spherical Bessel functions of the first and the second kinds. P_n^m are the Legendre functions of the first kind.

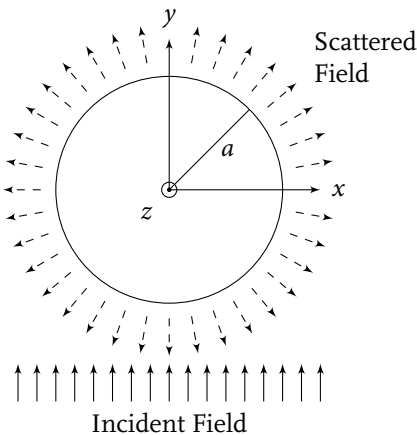


Figure 5.3 – Geometry of the Mie Theory calculations

The vectorial spherical harmonics are generated from the scalar ones via the following definitions

$$\mathbf{M}_{emn} = \nabla \times (\mathbf{r}\psi_{emn})$$

$$\mathbf{N}_{emn} = \frac{\nabla \times \mathbf{M}_{emn}}{k}$$

$$\mathbf{M}_{omn} = \nabla \times (\mathbf{r}\psi_{omn})$$

$$\mathbf{N}_{omn} = \frac{\nabla \times \mathbf{M}_{omn}}{k}.$$

It is possible to expand any field configuration that has zero divergence (i.e. one which does not have any sources in it) in terms of the vectorial spherical harmonics. Of particular interest is the expansion of a plane wave. Suppose we have a plane wave polarized in x direction, propagating towards a spherical dielectric object. The symmetry of the

geometry leads us to use the spherical coordinate system. However, we are also required to be able to expand a plane wave in terms of vector spherical harmonics in order to fully take advantage of the symmetries. We have

$$\mathbf{E}_i = E_0 \exp(ikr \cos \theta) \hat{x} = E_0 \sum_{n=1}^{\infty} i^n \frac{2n+1}{n(n+1)} (\mathbf{M}_{o1n} - i\mathbf{N}_{e1n})$$

and by using $\nabla \times \mathbf{E} = -\partial \mathbf{B}/\partial t = i\omega\mu\mathbf{H}$ we get

$$\mathbf{H}_i = -\frac{k}{\omega\mu} E_0 \sum_{n=1}^{\infty} i^n \frac{2n+1}{n(n+1)} (\mathbf{M}_{e1n} + i\mathbf{N}_{o1n})$$

for the electric and the magnetic fields. Detailed derivations of these equations can be found at [14, Sec. 4.2].

Scattered fields can also be written as a superposition of the vector spherical harmonics. We will have

$$\begin{aligned} \mathbf{E}_s &= \sum_{n=1}^{\infty} E_n (ia_n \mathbf{N}'_{e1n} - b_n \mathbf{M}'_{o1n}) \\ \mathbf{H}_s &= \frac{k}{\omega\mu} \sum_{n=1}^{\infty} E_n (ib_n \mathbf{N}'_{o1n} + a_n \mathbf{M}'_{e1n}) \end{aligned}$$

where the prime ('') denotes that the radial part of the scattered fields are Hankel functions, i.e. spherical Bessel functions of the *third* kind, whereas the unprimed vector spherical harmonics have radial parts which are composed of the spherical Bessel functions of the *first* kind. In the expressions above $E_n = i^n(2n+1)/[n(n+1)]$.

Once we know what the scattered fields—or, equivalently what the coefficients a_n and b_n are—we can define the scattering cross section of the sphere, C_{sca} , as

$$C_{\text{sca}} = \frac{W_{\text{sca}}}{I_i} = \frac{2\pi}{k^2} \sum_{n=1}^{\infty} (2n+1)(|a_n|^2 + |b_n|^2).$$

Here, W_{sca} is the total power flux due to scattered fields through a sphere of radius $r > a$ defined as

$$W_{\text{sca}} = \frac{1}{2} \operatorname{Re} \int_0^{2\pi} d\phi \int_0^{\pi} d\theta r^2 \sin(\theta) \mathbf{E}_s \times \mathbf{H}_s^*$$

and I_i is the intensity of the incoming plane wave

$$I_i = \frac{1}{2} \frac{k}{\omega \mu \epsilon} E_0^2.$$

Finally, the *scattering efficiency*, Q_{sca} , is defined as

$$Q_{\text{sca}} = \frac{C_{\text{sca}}}{\pi a^2},$$

and it relates to the amount of scattering that the sphere causes, normalized with respect to its geometrical cross section area.

Total fields outside of the sphere are

$$\mathbf{E} = \mathbf{E}_i + \mathbf{E}_{\text{sca}}$$

$$\mathbf{H} = \mathbf{H}_i + \mathbf{H}_{\text{sca}}.$$

Therefore the Poynting vector is

$$\mathbf{S} = \frac{1}{2} \operatorname{Re}[\mathbf{E} \times \mathbf{H}^*] = \mathbf{S}_i + \mathbf{S}_{\text{sca}} + \mathbf{S}_{\text{ext}}.$$

Total power absorbed, W_{abs} , in a closed volume A is

$$W_{\text{abs}} = - \int_A \mathbf{S} \cdot \hat{\mathbf{r}} dA$$

where $\hat{\mathbf{r}}$ is the normal to the surface A . If $W_{\text{abs}} > 0$ power is absorbed in the volume.

From the definition of \mathbf{S} we get

$$\begin{aligned} W_{\text{abs}} &= - \int_A \mathbf{S}_i \cdot \hat{\mathbf{r}} dA - \int_A \mathbf{S}_{\text{sca}} \cdot \hat{\mathbf{r}} dA - \int_A \mathbf{S}_{\text{ext}} \cdot \hat{\mathbf{r}} dA \\ &= W_i - W_{\text{sca}} + W_{\text{ext}}. \end{aligned}$$

The reason for the sign difference of the W_{sca} term is the fact that scattered fields by construction propagate away from the scatterer. We will assume that the scatterer is surrounded by a medium with no absorption, therefore $W_i = 0$. Hence, we arrive at the

equality

$$W_{\text{ext}} = W_{\text{sca}} + W_{\text{abs}}$$

which defines the extinction cross section and extinction efficiency as

$$C_{\text{ext}} = \frac{W_{\text{ext}}}{I_i} = \frac{2\pi}{k^2} \sum_{n=1}^{\infty} (2n+1) \operatorname{Re}(a_n + b_n)$$

where W_{ext} is defined as,

$$W_{\text{ext}} = \frac{1}{2} \operatorname{Re} \int_0^{2\pi} d\phi \int_0^{\pi} d\theta r^2 \sin(\theta) [\mathbf{E}_i \times \mathbf{H}_s^* + \mathbf{E}_s \times \mathbf{H}_i^*]$$

and finally we have,

$$Q_{\text{ext}} = \frac{C_{\text{ext}}}{\pi a^2}.$$

By applying the boundary conditions, that is, the continuity of the tangential magnetic (H_θ, H_ϕ) and electric (E_θ, E_ϕ) fields, the coefficients a_n and b_n can be found for arbitrary dielectric spheres. In Figure 5.4, we plot Q_{ext} as a function of $1/\lambda$ for three different sizes of spheres made out of water. We use the frequency dependent refractive index of water from [146]. Our aim here is to check our calculation routines by comparing them against results obtained by others. Comparison of Figure 5.4 with [14, Fig. 4.6, p. 105] validates our calculations.

Now, we can investigate the applicability of another boundary condition, namely, the *surface impedance boundary condition*, for spheres made out of metals—gold in our case.

The surface impedance boundary condition relates the tangential fields on surfaces via the condition

$$\mathbf{E}_{\parallel} = Z_s \hat{n} \times \mathbf{H}_{\parallel}. \quad (5.1)$$

Here, \parallel denotes tangential field components and \hat{n} is the surface normal of the sphere. Z_s is called the surface impedance associated with a metal, defined as

$$Z_s = \sqrt{\frac{\mu_0}{\epsilon_m}}$$

where μ_0 is the permeability of vacuum and ϵ_m is the refractive index of the metal.

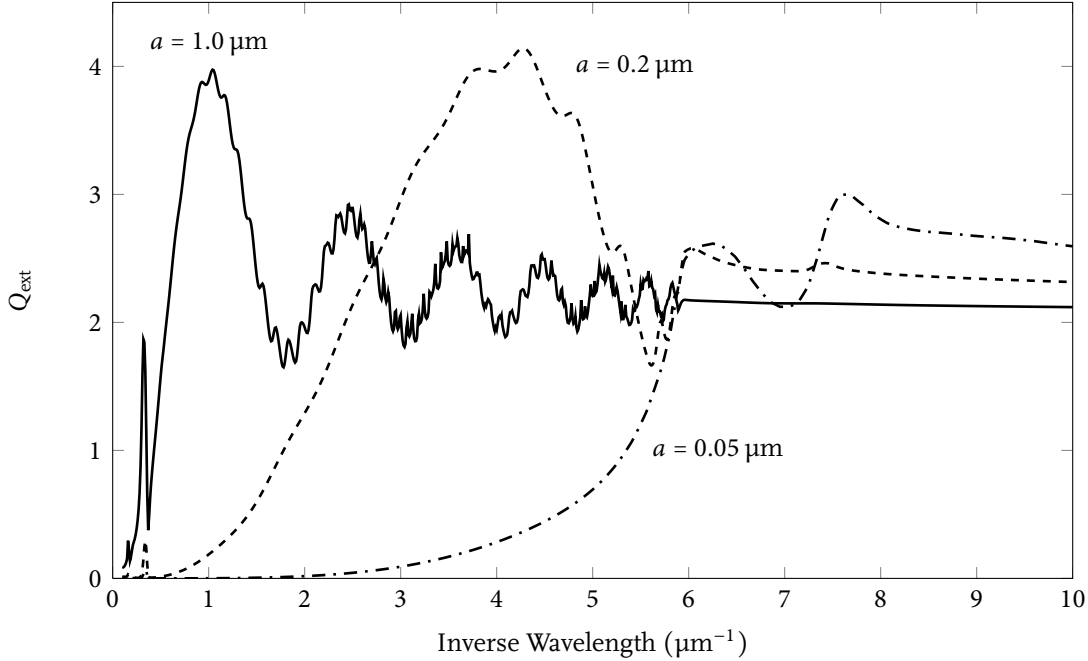


Figure 5.4 – Extinction efficiencies of water spheres of three different radii.

Using (5.1), and the definitions of the incident and the scattered fields, one can deduce the values for a_n and b_n as

$$a_n = \frac{j_n(ka) - i \frac{Z_0}{Z_s} \frac{[kaj_n(ka)]'}{ka}}{h_n(ka) - i \frac{Z_0}{Z_s} \frac{[kah_n(ka)]'}{ka}}$$

$$b_n = \frac{j_n(ka) - i \frac{Z_s}{Z_0} \frac{[kaj_n(ka)]'}{ka}}{h_n(ka) - i \frac{Z_s}{Z_0} \frac{[kah_n(ka)]'}{ka}}$$

where the term $[kaj_n(ka)]'$ is a shorthand notation for

$$\left. \frac{d}{d\rho} \{ \rho j_n(\rho) \} \right|_{\rho=ka}$$

and h_n are the spherical Bessel function of the third kind, i.e. Hankel functions. Similar

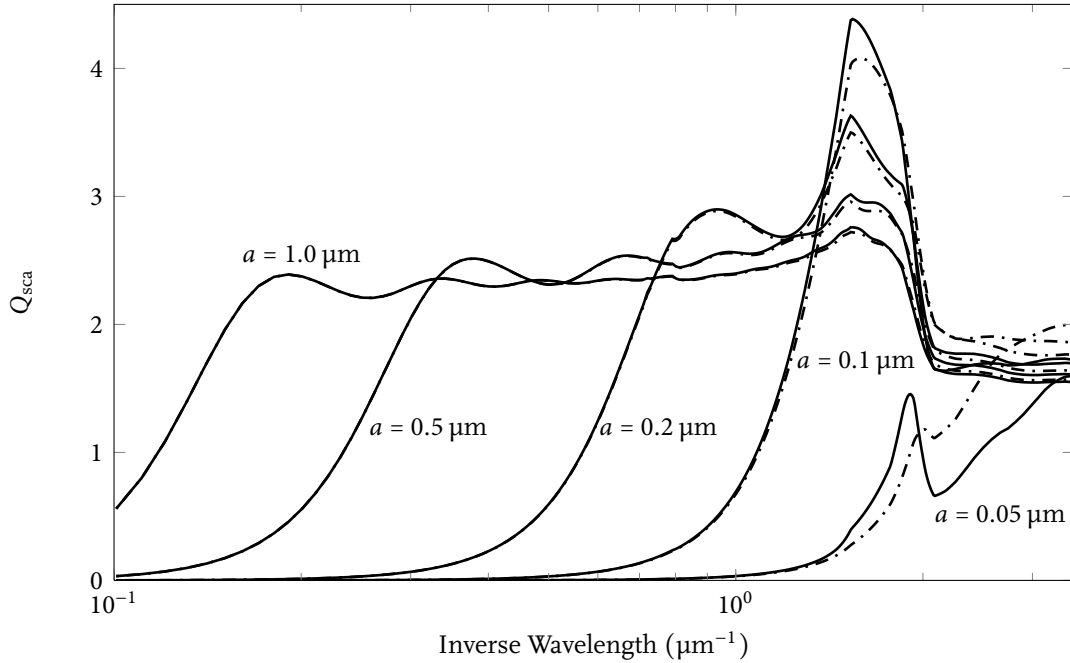


Figure 5.5 – Scattering efficiencies of gold spheres of various different radii. Solid lines are the exact Mie solutions, dot-dashed lines are the solutions obtained through the use of the impedance boundary conditions.

conclusions for scattering by impedance spheres are also reported in [147, p. 476].

We have solved the scattering of a plane wave from gold spheres of various dimensions using both the full Mie solution and also using the surface impedance boundary condition solution. The full solution allows the fields to exist within the gold spheres, whereas the surface impedance calculations neglect the fields within the sphere and approximate the effects of the material by a boundary condition given in (5.1). From Figure 5.5 we can see that there is perfect agreement between the two approaches as long as the radius of the sphere is larger than the penetration depth of the fields into the metal [148]. As the frequency is increased—inverse wavelength is increased—electromagnetic fields penetrate more and more into the metal due to a decrease in the permittivity of metals. As a result, the two approaches begin to deviate from each other. However, in the infrared region, the surface impedance approximation works sufficiently well. Now, we will make use of this observation to analyze scatterers other than spheres by discretizing an integral equation for electromagnetic fields and we will call this technique the

method of moments.

5.3.2 Method of Moments

So far, we have only investigated spherical shapes and were able to analytically calculate the scattering of fields. A natural question to ask at this stage—one which we will answer soon—is what to do in case the scatterer of interest is one which has little or no symmetries in its shape, an arbitrary geometry in general.

It is possible to describe scattering by an arbitrary shaped object through integral equations derived from Maxwell's equations. In antenna theory, two specific equations are often emphasized: the *electric field integral equation* (EFIE) and the *magnetic field integral equation* (MFIE). In this section, we will specifically focus on the EFIE.

If we have a scatterer surface S —which may be open or closed—and an incident electric field \mathbf{E}_i impinges upon the scatterer, surface currents will be formed such that

- for perfect electric conductors, the tangential electric field will be zero on the surface,
- for surfaces with a finite surface impedance, the surface currents will form to satisfy the surface impedance boundary condition (5.1).

Once we know the surface currents on S , then the scattered fields can be calculated through the use of the vector potential \mathbf{A} and the scalar potential ϕ via

$$\begin{aligned}\mathbf{E}_s &= -\frac{\partial \mathbf{A}}{\partial t} - \nabla \phi \\ &= -j\omega \mathbf{A} - \nabla \phi \quad \text{where we have} \\ \mathbf{A}(\mathbf{r}) &= \frac{\mu}{4\pi} \int_S \mathbf{J} \frac{e^{-jkR}}{R} dS' \\ \phi(\mathbf{r}) &= \frac{1}{4\pi\epsilon} \int_S \sigma \frac{e^{-jkR}}{R} dS'.\end{aligned}\tag{5.2}$$

In the expressions above, $R = |\mathbf{r} - \mathbf{r}'|$ where \mathbf{r} is the observation point and \mathbf{r}' is a source point on S . σ is the charge density on S which can be found through the use of the

continuity equation

$$\nabla_S \cdot \mathbf{J} = -j\omega\sigma$$

on S denoted by the subscript on ∇_S . Note that we have reverted back to the $\exp(j\omega t)$ time convention in this section.

One can define an integro-differential equation based on the unknown surface current \mathbf{J} by the application of (5.1) which results in

$$\begin{aligned} \mathbf{E}_{\parallel} &= Z_S \hat{n} \times \mathbf{H} \\ \mathbf{E}_{i,\parallel} + \mathbf{E}_{s,\parallel} &= Z_S \mathbf{J} \\ \mathbf{E}_{i,\parallel} + (-j\omega\mathbf{A} - \nabla\phi)_{\parallel} &= Z_S \mathbf{J} \quad \text{equivalently} \\ \mathbf{E}_{i,\parallel} &= (j\omega\mathbf{A} + \nabla\phi)_{\parallel} + Z_S \mathbf{J}. \end{aligned} \quad (5.3)$$

Equations (5.2)-(5.3) are called the EFIE. After the formulation of the EFIE, the equation is solved on the surface S where $R \rightarrow 0$. There are different ways of solving the equation; the one which we will pursue is based on the approach developed by Rao, Wilton and Glisson [149], which we will explain now.

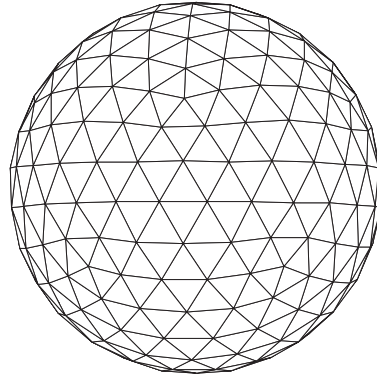


Figure 5.6 – Triangulation of a spherical surface using the basis functions developed by Rao, Wilton and Glisson.

The main idea in [149] is to come up with a local set of basis functions that can be used to meaningfully map S . The basis functions are composed of triangles, and each side of the triangle corresponds to a current element which is proportional to the length of the edge (but normalized with respect to the total area of the each triangle).

Figure 5.6 shows an example triangulation for a sphere. For more details about the basis functions, please see [149]. Once the basis functions are defined, then (5.3) is discretized using the basis functions, necessary overlap integrals are calculated, and finally as a result the equation is converted into a linear matrix equation the solution of which leads to the surface currents. This technique of converting an integral equation into a series of coupled linear equations through the use of a set of basis functions and their overlap integrals is called *the method of moments* (MoM).

In [149], equations are provided only for the PEC surfaces. The perfect electric conductor is equivalent to the $Z_s = 0$ surface impedance. We generalized the formulation in [149] for arbitrary Z_s and to check our formulation, we simulated the scattering off of spheres with different radii and with surface impedances of gold.³ In Figure 5.7 we plot our results. As can be seen from the figure, the agreement is pretty good over a wide range of frequencies. However, the EFIE method is plagued with divergences at natural frequencies of closed scatterers [150]. We can see that the agreement between the exact result and the method of moments solution deteriorates above a certain frequency based on the dimensions of the sphere.

After having simulated the scattering off of spheres, we then looked into the scattering properties of thin sheets of rectangular patches of zero thickness. Our aim was to simulate a dipole antenna and understand its resonance properties for the case when the dipole element is not very narrow. In Figure 5.8, we show the results for scattered energy off of a rectangular patch of width 189 nm and of length 650 nm. For the perfect electric conductor case, the first resonance is around $\lambda = 1500$ nm which is expected from classical antenna theory—we would expect a resonance at $\lambda/2$ length, and due to the rather large width of the patch (189 nm) the resonance has shifted. When we include the surface impedance associated with gold into our scattering calculations, we see that the resonance has shifted to lower wavelengths, $\lambda \approx 2 \mu\text{m}$.

The MoM simulations do not require much computational power and the MoM technique is a good tool to get a qualitative understanding of the properties of antennas at optical frequencies. However, the fact that arbitrary dielectric structures cannot be simulated and the divergence problems associated with natural frequencies of closed

³Data from [16] was used to calculate the surface of impedance of gold at different wavelengths.

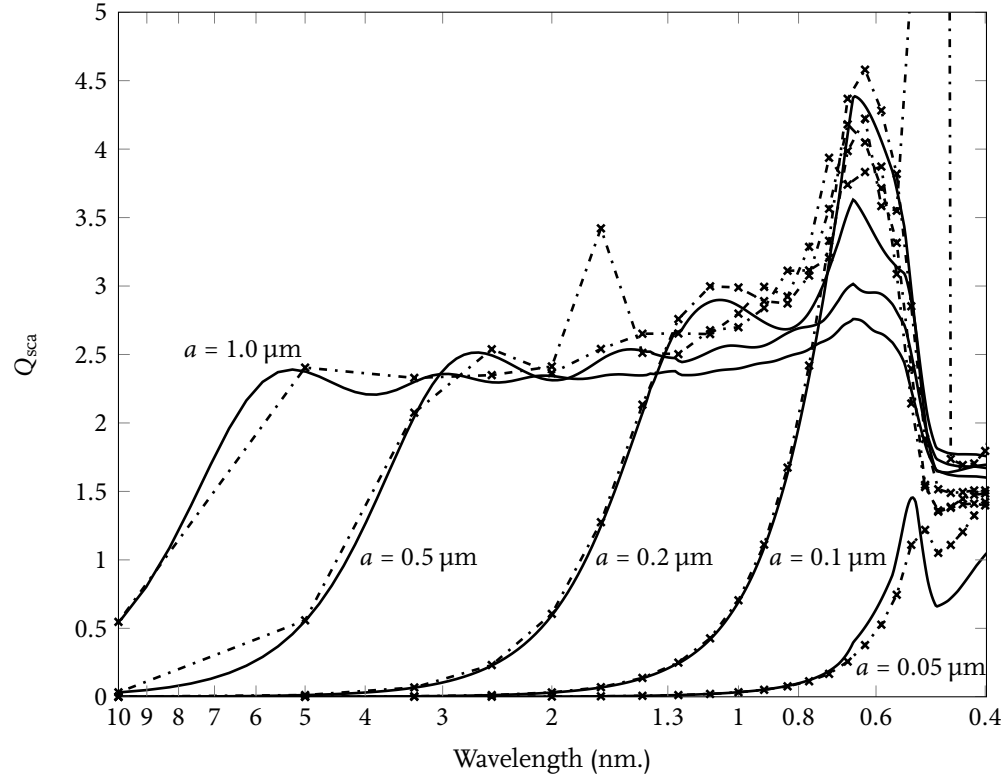


Figure 5.7 – Comparison of MoM simulations with the exact Mie calculations. Solid lines denote the exact Mie solution using the full field formulation, crosses denote the method of moments calculations.

structures cast a shadow on the the amount of trust one can have from the results obtained through the MoM. Furthermore, if the scatterer of interest is in the vicinity of a layered medium, then the MoM formulation requires the calculation of the necessary Green's function of the layered system—a non-trivial computation.

Is there a simpler, more general method that can tell us how electromagnetic waves scatter off of arbitrary geometries without having to make questionable assumptions about their properties? One possible answer to the question lies in the domain of methods dubbed with the prefix *finite-difference*, one of which we will investigate next.

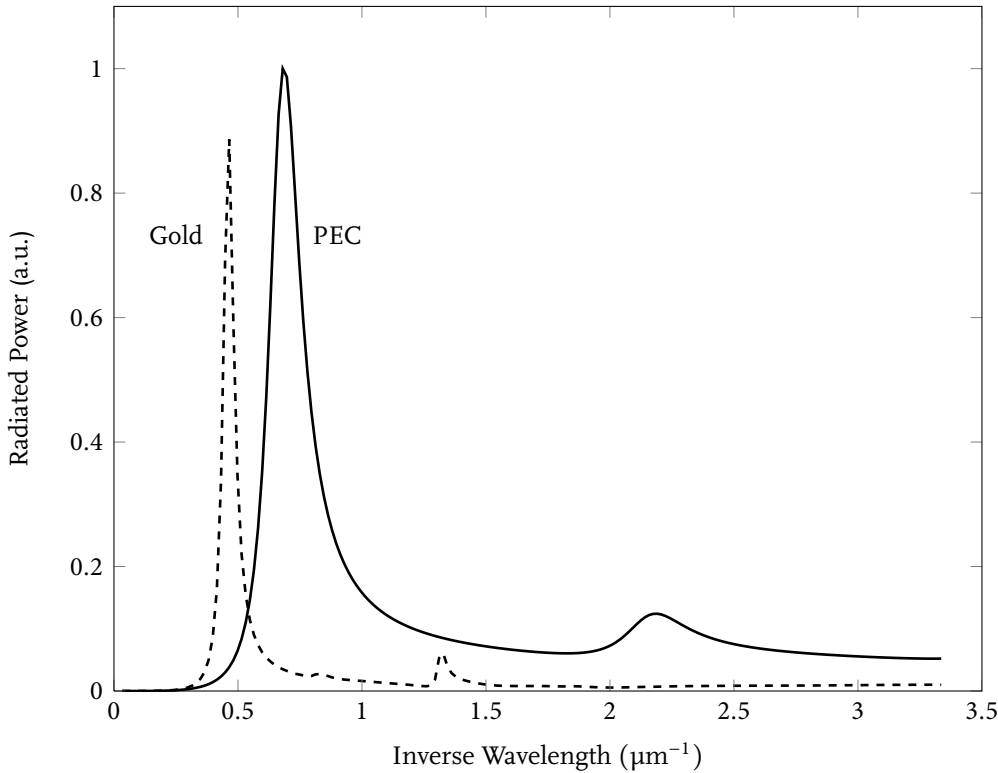


Figure 5.8 – Method of Moments simulation results and the red shift observed in resonance length.

5.3.3 Finite-Difference Time-Domain

Up until now, the techniques we have introduced for the calculation of the scattering of electromagnetic waves had certain limitations: Mie scattering only applies to spherical geometries, and the method of moments cannot be used in cases where the surface impedance approximation fails. In this section, we will introduce the finite-difference time-domain (**FDTD**) technique, which will enable us to analyze structures with arbitrary shapes and dielectric properties under various light illumination conditions.

The main idea behind **FDTD** is to discretize space and time. Space is discretized into little cubes. Each cube will have six fields associated with itself—three for the electric and another three for the magnetic fields. We will step discretely in time, and at each time step, we will update the fields in every cube. Update of the fields in a given cube will depend on the field history of the cube and the field history of the surrounding cubes. Furthermore, the way we update the fields of the cubes will depend on the type

of the cube: a cube which represents a lossless dielectric will update its fields differently than another one which represents a metal.

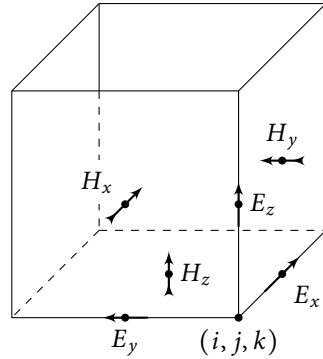


Figure 5.9 – Yee Lattice used in finite difference frequency domain calculations.

Figure 5.9 shows the $(i, j, k)^{\text{th}}$ cube in our lattice. As you can see, the fields are defined at different positions. Let Δx , Δy and Δz represent the separation of the cubes in \hat{x} , \hat{y} and \hat{z} directions respectively. The index (i, j, k) will be used as a shorthand to refer to the position $\mathbf{r} = (i\Delta x)\hat{x} + (j\Delta y)\hat{y} + (k\Delta z)\hat{z}$. From the figure, we see that the fields are defined at

$$\begin{aligned} E_x &\rightarrow (i + \frac{1}{2}, j, k) & E_y &\rightarrow (i, j + \frac{1}{2}, k) & E_z &\rightarrow (i, j, k + \frac{1}{2}) \\ H_x &\rightarrow (i, j + \frac{1}{2}, k + \frac{1}{2}) & H_y &\rightarrow (i + \frac{1}{2}, j, k + \frac{1}{2}) & H_z &\rightarrow (i + \frac{1}{2}, j + \frac{1}{2}, k). \end{aligned}$$

Why define the positions in such an eclectic way? The reason will be apparent once we investigate the details of the Maxwell's equations, which will be put on the lattice of fields. First, let us recall the differential form of Maxwell's equations

$$\begin{aligned} \nabla \times \mathbf{H} &= \mathbf{J} + \frac{\partial \mathbf{D}}{\partial t} \\ \nabla \times \mathbf{E} &= -\mathbf{M} - \frac{\partial \mathbf{B}}{\partial t} \\ \mathbf{J} &= \mathbf{J}_{\text{source}} + \sigma \mathbf{E} \\ \mathbf{M} &= \mathbf{M}_{\text{source}} + \sigma^* \mathbf{H} \end{aligned} \tag{5.4}$$

where σ is the electrical conductivity in units of siemens/meter and σ^* is the magnetic

conductivity in ohms/meter. \mathbf{J} and \mathbf{M} refer to the electrical and magnetic current densities respectively.

For linear, isotropic, non-dispersive and lossy materials we have the following set of equations:

$$\begin{aligned}\frac{\partial \mathbf{H}}{\partial t} &= -\frac{1}{\mu} \nabla \times \mathbf{E} - \frac{1}{\mu} (\mathbf{M}_{\text{source}} + \sigma^* \mathbf{H}) \\ \frac{\partial \mathbf{E}}{\partial t} &= \frac{1}{\epsilon} \nabla \times \mathbf{H} - \frac{1}{\epsilon} (\mathbf{J}_{\text{source}} + \sigma \mathbf{E})\end{aligned}$$

Looking at the x, y and z components separately results in

$$\begin{aligned}\frac{\partial H_x}{\partial t} &= \frac{1}{\mu} \left(\frac{\partial E_y}{\partial z} - \frac{\partial E_z}{\partial y} - M_{\text{source},x} - \sigma^* H_x \right) \\ \frac{\partial H_y}{\partial t} &= \frac{1}{\mu} \left(\frac{\partial E_z}{\partial x} - \frac{\partial E_x}{\partial z} - M_{\text{source},y} - \sigma^* H_y \right) \\ \frac{\partial H_z}{\partial t} &= \frac{1}{\mu} \left(\frac{\partial E_x}{\partial y} - \frac{\partial E_y}{\partial x} - M_{\text{source},z} - \sigma^* H_z \right) \\ \frac{\partial E_x}{\partial t} &= \frac{1}{\epsilon} \left(\frac{\partial H_z}{\partial y} - \frac{\partial H_y}{\partial z} - J_{\text{source},x} - \sigma E_x \right) \\ \frac{\partial E_y}{\partial t} &= \frac{1}{\epsilon} \left(\frac{\partial H_x}{\partial z} - \frac{\partial H_z}{\partial x} - J_{\text{source},y} - \sigma E_y \right) \\ \frac{\partial E_z}{\partial t} &= \frac{1}{\epsilon} \left(\frac{\partial H_y}{\partial x} - \frac{\partial H_x}{\partial y} - J_{\text{source},z} - \sigma E_z \right).\end{aligned}\tag{5.5}$$

As you can see above, space and time derivatives are coupled to each other through the curl equations. Our aim is to discretize the equations in space-time in order to come up with an iterative mechanism which solves the scattering problem. We will use the convention $A|_{i,j,k}^n$ to denote the discretized version of a function $A(\mathbf{r}, t)$ where (i, j, k) signifies \mathbf{r} and $t = n\Delta t$. Note that, in (5.5), both sides of the equalities have the same time and space coordinates, therefore, our discretization scheme should respect the locality of the underlying differential operators.

We will define electric fields at integer multiples of Δt whereas the magnetic fields will be defined at time steps that are offset by $\Delta t/2$. To understand the reason behind

such a choice, let us take a closer look at the equation for E_x .

$$\frac{\partial E_x}{\partial t} = \frac{1}{\epsilon} \left(\frac{\partial H_z}{\partial y} - \frac{\partial H_y}{\partial z} - J_{\text{source},x} - \sigma E_x \right). \quad (5.6)$$

Here, time derivative of E_x is related to the space derivatives of H_z and H_y . In general, we will calculate the derivatives based on a first order difference equation. For instance, the derivative of an arbitrary function $f(x)$ at $x = x_0$ will be defined as

$$\frac{df(x)}{dx} \Big|_{x=x_0} \approx \frac{f(x + x_0/2) - f(x - x_0/2)}{\Delta x}.$$

As you see above, in order to calculate the derivative at $x = x_0$ we looked at the value of the function at $x = x \pm x_0/2$ so that their difference would give us the slope of $f(x)$ right at where we are interested: x_0 . With that in mind, we can discretize (5.6) as

$$\begin{aligned} \frac{E_x|_{i+\frac{1}{2},j,k}^{n+1} - E_x|_{i+\frac{1}{2},j,k}^n}{\Delta t} &= \frac{1}{\epsilon} \left(\frac{H_z|_{i+\frac{1}{2},j+\frac{1}{2},k}^{n+\frac{1}{2}} - H_z|_{i+\frac{1}{2},j-\frac{1}{2},k}^{n+\frac{1}{2}}}{\Delta y} - \frac{H_y|_{i+\frac{1}{2},j,k+\frac{1}{2}}^{n+\frac{1}{2}} - H_y|_{i+\frac{1}{2},j,k-\frac{1}{2}}^{n+\frac{1}{2}}}{\Delta z} \right. \right. \\ &\quad \left. \left. - J_{\text{source},x}|_{i+\frac{1}{2},j,k}^{n+\frac{1}{2}} - \sigma \frac{E_x|_{i+\frac{1}{2},j,k}^{n+1} - E_x|_{i+\frac{1}{2},j,k}^n}{2} \right) \right). \end{aligned}$$

Note that, in the equation above, the left hand side is defined at $t = (n + \frac{1}{2})\Delta t$ and so is the right hand side— H fields are by construction defined with an half integer offset, and the σE_x term on the right side of (5.6) is averaged at n and $n + 1$ to approximate its value at $n + \frac{1}{2}$. Likewise, E_x is defined at the space location $(i + \frac{1}{2}, j, k)$, and so is $\partial_t E_x$, the left side of the equation. The derivatives on the right side are similarly defined at the effective location $(i + \frac{1}{2}, j, k)$.

Finally, collecting terms in (5.6) gives the following update equation for E_x :

$$E_x|_{i+\frac{1}{2},j,k}^{n+1} = \frac{1 - \frac{\sigma_{i+\frac{1}{2},j,k}\Delta t}{2\epsilon_{i+\frac{1}{2},j,k}}}{1 + \frac{\sigma_{i+\frac{1}{2},j,k}\Delta t}{2\epsilon_{i+\frac{1}{2},j,k}}} E_x|_{i+\frac{1}{2},j,k}^n + \frac{\frac{\Delta t}{\epsilon_{i+\frac{1}{2},j,k}}}{1 + \frac{\sigma_{i+\frac{1}{2},j,k}\Delta t}{2\epsilon_{i+\frac{1}{2},j,k}}} \times \\ \left(\frac{H_z|_{i+\frac{1}{2},j+\frac{1}{2},k}^{n+\frac{1}{2}} - H_z|_{i+\frac{1}{2},j-\frac{1}{2},k}^{n+\frac{1}{2}}}{\Delta y} - \frac{H_y|_{i+\frac{1}{2},j,k+\frac{1}{2}}^{n+\frac{1}{2}} - H_y|_{i+\frac{1}{2},j,k-\frac{1}{2}}^{n+\frac{1}{2}}}{\Delta z} \right. \\ \left. - J_{\text{source},x}|_{i+\frac{1}{2},j,k}^{n+\frac{1}{2}} \right). \quad (5.7)$$

Derivation of the update equations are very similarly done for the other field components. We refer the reader to [151, Ch. 3] for details. The development of the described discretization scheme in time and space in a leapfrogged manner—that is all fields are circulating one another both in time and space—was first developed by Yee in 1966 and therefore Figure 5.9 is also called as the Yee Lattice [152].

So far, we have described the basic structure of the FDTD technique. In order to successfully simulate metallic scatterers at optical frequencies, one needs to be able to

- excite the structure with a given polarization state and frequency range of light,
- take into account the dispersive nature of the optical properties of metals,
- be able to simulate non-periodic scatterers through the use of absorbing boundary conditions, and
- be able to calculate scattered fields through the use of total field/scattered field technique.

Exciting a finite amount of simulation volume by plane waves, which are supposed to be infinite in extent, is non-trivial. However, the total field/scattered field technique is one that solves the problem. We will talk about the total field/scattered field technique next.

The total field/scattered field (TF/SF) method is based on the induction theorem [153, Sec. 7.9, pp. 334–338]. The main idea relies on the observation that, for the electromagnetic wave equations, once the boundary conditions and the properties of the media are

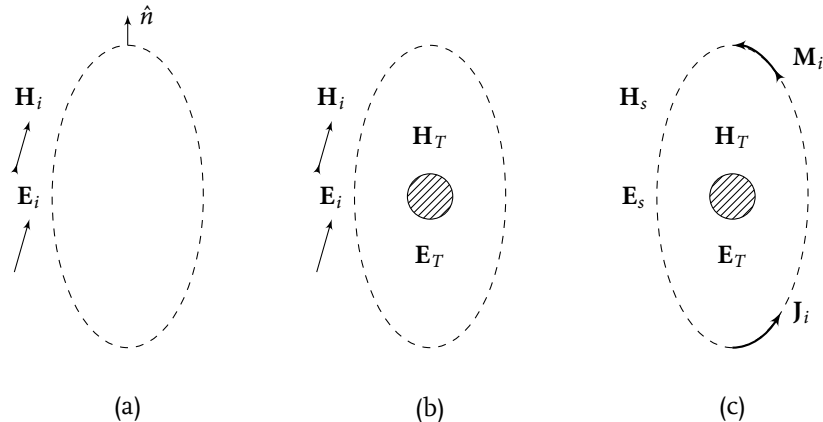


Figure 5.10 – Field teleportation schematic.

determined, the solution of the electromagnetic scattering problem is uniquely defined.

In Figure 5.10(a) incident electric and magnetic fields, \mathbf{E}_i and \mathbf{H}_i are shown to propagate through the volume, V , shown by the dashed curve. Suppose we put a scatterer in V as illustrated in Figure 5.10(b). Due to the interaction of the incident fields with the scatterer, there would be scattered fields \mathbf{E}_s and \mathbf{H}_s . The total fields within V , therefore, are $\mathbf{E}_T = \mathbf{E}_s + \mathbf{E}_i$ and $\mathbf{H}_T = \mathbf{H}_s + \mathbf{H}_i$.

What would happen if we were to put some electric and magnetic surface current terms \mathbf{J}_i and \mathbf{M}_i on the boundary of V as shown in 5.10(c)? From Maxwell's equations, we can derive the boundary conditions

$$\begin{aligned}\hat{n} \times (\mathbf{H}_{\text{out}} - \mathbf{H}_{\text{in}}) &= \mathbf{J}_i \\ \hat{n} \times (\mathbf{E}_{\text{out}} - \mathbf{E}_{\text{in}}) &= -\mathbf{M}_i\end{aligned}$$

by integrating the $\nabla \times \mathbf{E}$ and $\nabla \times \mathbf{H}$ terms in (5.4) along a closed surface that intersects the boundary with the normal to the boundary defined as \hat{n} [153, Sec. 1.5]. Now, we will make a specific choice for \mathbf{J}_i and \mathbf{M}_i : we would like to have only the scattered fields outside of V and the total fields within V . Setting $\mathbf{H}_{\text{out}} = \mathbf{H}_s$, $\mathbf{E}_{\text{out}} = \mathbf{E}_s$, $\mathbf{H}_{\text{in}} = \mathbf{H}_T = \mathbf{H}_s + \mathbf{H}_i$

and $\mathbf{E}_{\text{in}} = \mathbf{E}_T = \mathbf{E}_s + \mathbf{E}_i$ results in

$$\mathbf{J}_i = -\hat{\mathbf{n}} \times \mathbf{H}_i$$

$$\mathbf{M}_i = \hat{\mathbf{n}} \times \mathbf{E}_i.$$

Note that \mathbf{J}_i and \mathbf{M}_i depend only on the incident fields, which are up to us to choose. We can calculate what they will be for a given V and a given space/time input field dependence. Then, we source the volume of interest which encapsulates our scatterer with the surface currents \mathbf{J}_i and \mathbf{M}_i . In the absence of the scatterer, such a sourcing will inject the incident fields into the volume, and there will be no fields outside of V . Once we add the scatterer, however, there will be scattering and we will only observe the scattered fields outside of V . This technique—called **TF/SF** or *field teleportation* method—allows us to source infinite extent plane-wave like excitations within a finite simulation domain, and observe the scattered fields directly. In [154] a detailed numerical analysis of the method, and its application and verification is presented.

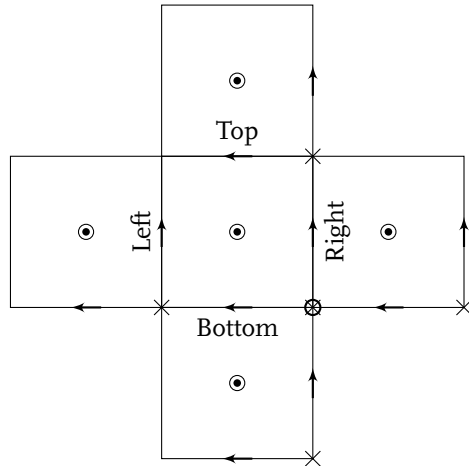


Figure 5.11 – Object oriented programming approach.

Before we conclude this section, we will briefly comment on the way in which we coded the FDTD algorithm. As has been illustrated for the update equation given for E_x in (5.7), electric (magnetic) fields are updated based on the material properties associated with the cube in which they reside and also based on the magnetic (electric) fields surrounding them. One of the most painstaking parts of coding a three dimensional

FDTD program is making sure that all the indices point to the exactly the right location, and that correct values of the fields around a given point are read. Recently, object oriented programming methodology was shown to help in this regard [155]. The idea is to take the unit cell as shown in Figure 5.9 and collect all the information required to update the fields in the unit cell in an “object” associated with the specific material. For instance, one can define objects for lossless dielectric materials, metals with frequency dependant permittivities and absorbing boundary conditions. Then, each cube is created by instantiating an object, and cubes are made aware of their surrounding through pointers to other objects. In Figure 5.11 we show how the computational lattice would look for a cube in a two dimensional world. The cube would have its own fields, and also it would know about its top, bottom, left and right neighbors. Field updates are then done by going through all cubes and telling each one to update their electric fields, then looping through all cubes and this time instructing them to update their magnetic fields. Since electric fields depend on magnetic fields for field updates, and vice versa, once both the electric and magnetic fields are updated, one has successfully finished the calculation of field propagation at a given time instant. The whole procedure repeats until either fields converge to their steady state values for time harmonic excitations, or, until all fields decay to a negligible value for gaussian pulse type excitations.

We will provide results of FDTD calculations in Section 5.4.

5.3.4 Green’s Function Methods

In this section, we will briefly talk about—mostly for reasons of completeness—our last method of scattering analysis: the Green’s Function method. The technique requires the calculation of the vectorial Green’s function for a stratified volume and then the use of the Green’s function to calculate the scattering off of small patches of scatterers, the collection of which lead to the desired scattering geometry. In the method of moments section, we used the free space Green’s function in (5.2) to calculate the vector potential \mathbf{A} due to an arbitrary electric current source \mathbf{J} . When we have multiple layers, a geometry very common for integrated planar optics applications, then the form of the Green’s function will change, but still, an integration of \mathbf{J} with the appropriate Green’s function

will lead to \mathbf{A} and from there one can calculate the other field components.

Calculation of the Green's function is non-trivial, and requires careful convergence studies. For details of the technique and antenna related example calculations, we refer the reader to [156–158].

5.3.5 Summary

We have introduced four techniques for scattering analysis. Mie theory gave exact results for scattering off of spherical geometries with arbitrary material properties. We demonstrated the utility of impedance boundary conditions by using the Mie theory. Method of moments calculations can be used to analyze a variety of geometries, though the use of an arbitrary dielectric constant is not possible—but we have illustrated that through the use of the surface impedance boundary conditions one can get a qualitative understanding for the effects of metals' optical properties on scattering characteristics of various geometries. We then talked about FDTD and demonstrated how it can be applied to arbitrary geometries without any restriction on the dielectric properties. Lastly, we briefly talked about the Green's function method.

Of those methods which rely on discretization of a given volume to find out what the scattering properties of a geometry is, both the method of moments and Green's function techniques requires solving large matrix equations. On the other hand, FDTD does not involve any matrices, but one needs to do enough number of iterations until a steady state is reached or until all fields have left the simulation domain. Due to its conceptual simplicity and general applicability, we will use the FDTD technique in the upcoming section to design an antenna integrated photo-detector.

5.4 Sleeve Dipole Design for a Closely Integrated Antenna-Detector System

The interaction between optics and radio wave science may not be immediately apparent, but the development of the radio telescope is an example of the proximity among

the two disciplines (especially under the umbrella of astronomy), and the interdependence of the data created in one field on the other [159, p. 217]. Ginzton Laboratories at Stanford University, where the author has conducted his research, is another example of the historical continuity between the microwave and the optics community. Founded after WWII to conduct research in microwave theory, in 2009, near the end of its lifespan, most people in Ginzton now work on optics related topics as a result of the steady drive of research agendas that led to an evolution from investigating electron acceleration through the use of the klystron tubes to the use of light amplification by stimulated emission in various experimental setups.

Likewise, advances in integrated circuit fabrication techniques have also resulted in the development of planar optical components to be used in interconnect applications. As the capabilities of manufacturing grew, smaller and faster devices were made possible. At the time these lines are written, 45 nm CMOS technology is available in consumer electronics.

The capability to define such fine structures allows us to think about devices that are on the order of an optical wavelength ($\sim 1 \mu\text{m}$) or smaller. One intriguing idea is to ask whether the antenna technology commonly used in the radio and microwave frequencies can be ported to the optical domain so as to boost the sensitivity of small—even smaller than that of the wavelength—detectors while they retain their reduced dimensions and hence very fast operation speeds?

In this section we will provide an affirmative answer to this question by going over the requirements for an antenna integrated detector and describe a design with which the requirements can be satisfied.

Planar geometry & Substrate Effects The first requirement is that the device should be based on planar integrated circuit technology so that one can take advantage of the available fabrication tools. Although three dimensional networks of integrated circuits are being actively pursued, they are still in the research stage and therefore we will not consider them here. Planar geometry dictates that the antenna will be sitting on a layer with a permittivity higher than that of air. Resonance lengths of antennas are known

to depend strongly on the properties of the media surrounding them [160, 161]. Experiments made on chemically synthesized gold rods have also led to similar conclusions at optical frequencies [162].

Telecom Wavelengths Fiber optic communications are based on the frequency bands where the optical fibers have the lowest amount of loss—around 1300 nm and 1550 nm. The designed device should be able to work at these near infrared frequencies and that requires the choice of a semiconductor which absorbs light at these wavelength ranges.

Choice of Metal Metals' permittivities change as the frequency of operation is varied from the radiowave to the optical domain. In the previous sections, we used the surface impedance method to show that the resonance length of a metallic patch at a given frequency is reduced when we include the inductive surface impedance of the metal.

Antenna-Detector Integration Antennas are very sensitive to the presence of any other scattering elements within their near fields. As a result, one should be very careful about the way in which the semiconductor detector element is electrically contacted. If the design does not take into account the contact geometry, then the resonance obtained by the antenna will possibly shift or degrade.

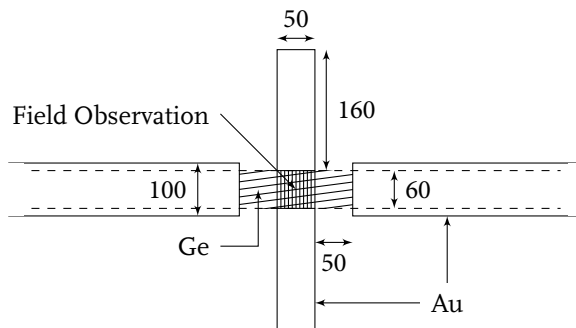


Figure 5.12 – Top view of the open-sleeve dipole geometry. All lengths are shown in units of nanometers. Dashed lines signify the continuation of the Ge line underneath the metal contacts. The metal is 50 nm thick.

Given all these considerations, we decided to use the topology of the open-sleeved

dipole antenna which was initially used to widen the bandwidth of regular dipole antennas [163]. The structure we have is illustrated in Figure 5.12. The antenna element is a regular dipole geometry of length 160 nm. The detector is a line of Ge of 60 nm width, which continues underneath the horizontal metal contacts on both sides of the antenna. The contacts are the sleeves of the open-sleeve topology. The contacts are 100 nm wide, and 50 nm thick. It has been shown that for light polarized in the direction of the dipole element, the sleeves minimally interact with the scattering properties of the dipole. The whole structure is sitting on an oxide surface and is covered with air on the top. The reason for the choice of the oxide geometry was to minimize substrate effects. We observed that if we were to situate the whole structure on silicon, for instance, due to the high refractive index of the silicon, the resonant length of the antenna shrank considerably and the enhancement at resonance was weak. However, moving to an oxide substrate helped us alleviate the problem with minimal impact on the antenna properties.

We tested our design using the FDTD technique. In order to be able to simulate the infinitely long contacts, we used the TF/SF method twice: once to inject plane waves from a simply layered⁴ 2D geometry into another 2D geometry with layers and the infinitely long Ge wire, and again to inject fields from the infinitely long 2D wire geometry into the 3D open-sleeve dipole structure.

	ω_{pm}	ω_m	Γ_m
$m = 1$	1.014076882E16	0.000000000E00	0.000000000E00
$m = 2$	6.861574653E15	2.046174861E10	4.390839341E14
$m = 3$	1.832181311E15	8.225155873E14	3.542118567E15

Table 5.1 – Third order Lorentz fit to experimental permittivity values for Au around 1500 nm.

We chose to use Au as the metal due to its large and negative refractive index at the near-infrared frequencies and the ease with which one can electrically contact Au in experiments. We modeled the relative permittivity of Au using the Drude-Lorentz

⁴by which we mean a semi-infinite space of air and in contact with another semi-infinite space of oxide

function

$$\epsilon_{\text{Au}}(\omega) = 1 + \sum_{m=1}^P \frac{(\omega_{pm})^2}{\omega_m^2 - \omega^2 + i\omega\Gamma_m} \quad \text{with } \omega_1 = 0$$

where ω_{pm} is the plasmon frequency of the m^{th} pole, ω_m is the oscillator frequency and Γ_m is the damping constant as has previously been defined in [164]. Note that, in the expansion above, setting any one of ω_m equal to zero makes it a Drude pole. That is why the first pole has its oscillator frequency, ω_1 , set to zero to make sure we have a mixture of Drude and Lorentz type of poles. We wrote a Mathematica script to fit the experimentally measured optical properties of Au [16] using the Nelder-Mead method⁵ for a three pole, $P = 3$, model. The fit parameters are tabulated in Table 5.1. Figure 5.13 compares the fit to the experimental data. The two curves agree quite well with each other.

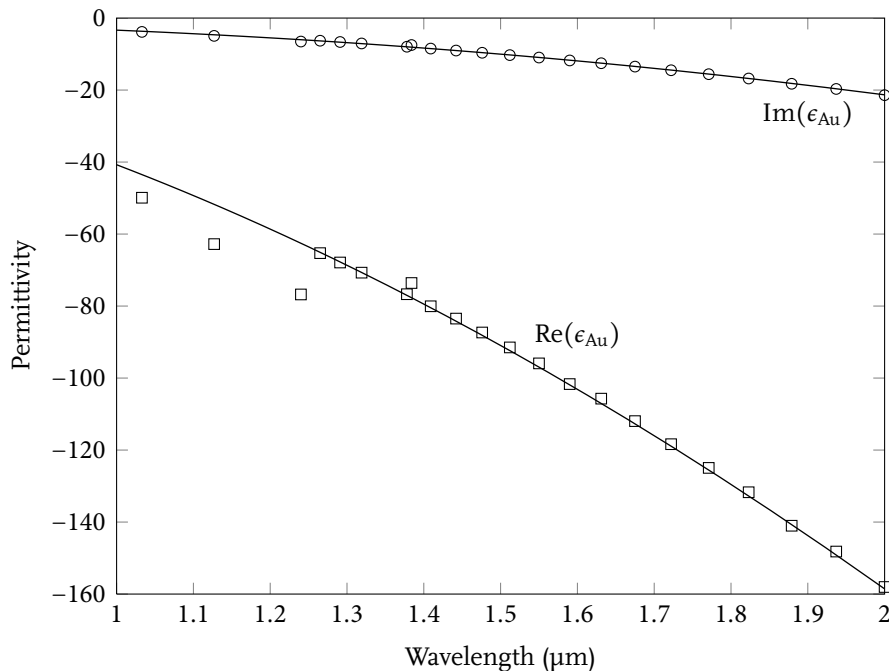


Figure 5.13 – Lorentz fit to experimental permittivity values for Au. Symbols are from [16]. Lines denote the third order Lorentz model fit.

⁵<http://reference.wolfram.com/mathematica/ref/NMinimize.html>

We covered the boundaries of our simulation domain with perfectly matched layers of the uniaxial type [151] and recorded the fields in the volume of Ge in between the two antenna arms as illustrated in Figure 5.12. We also recorded the near fields 25 nm above the oxide interface, which corresponds to the plane that symmetrically bisects the antenna geometry horizontally. In Figure 5.14 we plot the volumetric field intensity enhancement for two different polarizations: TM refers to polarization along the dipole direction, TE refers to polarization along the contact lines. As expected, volumetric enhancement is maximized when the polarization is parallel to the antenna arms. The ratio of the two responses is also plotted as a function of wavelength. At resonance, near fields show strong enhancement at the antenna edges and the Ge region as shown in the inset. Due to the high refractive index of Ge, strong energy localization takes place in between the two antenna arms.

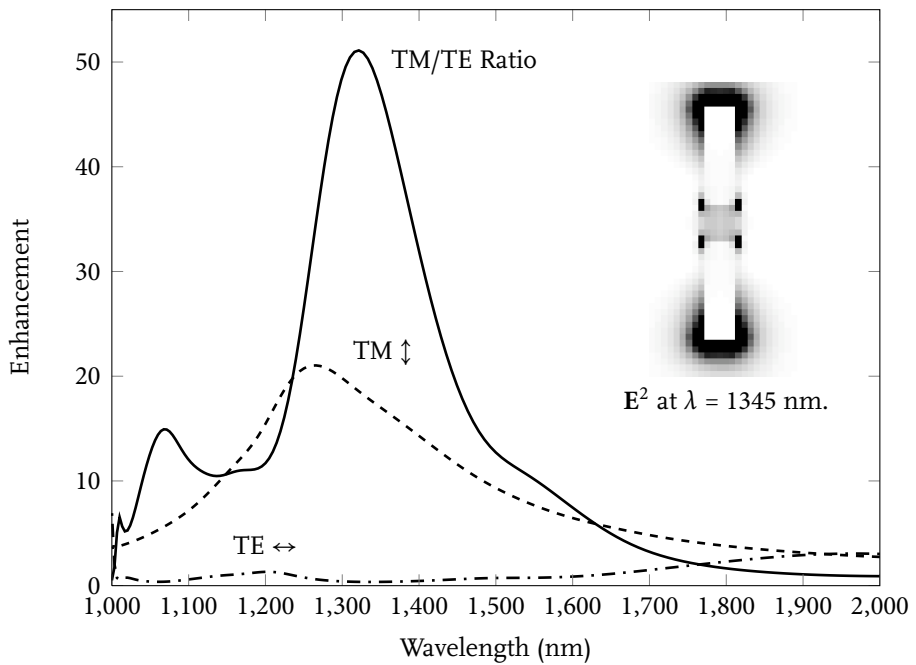


Figure 5.14 – Plot of the volumetric field intensity enhancement as a function of wavelength for different polarizations. Arrows denote the direction of the electric field polarization for the incoming plane wave illumination.

We experimentally tested the design by fabricating Ge based photo-detectors on a thick layer of oxide. The fabrication process—which was quite elaborate and required

us to grow crystalline Ge on oxide as well as to use focused ion beam to shape the Ge and the overlying metal structure—and the relevant measurement results can be found in [165]. In the next chapter, we will describe our efforts at experimentally observing field enhancement by using Si as the detector element via the silicon-on-oxide wafer technology and various optical measurement schemes.

Chapter 6

Fabrication and Measurement Results

6.1 Introduction

IN THE LAST chapter, we mainly talked about theoretical and numerical investigation of antennas and detectors. As we mentioned at the end of the last chapter, we were able to experimentally observe the antenna effect by growing crystalline germanium on a thick ($\approx 1 \mu\text{m}$) oxide and investigate the properties of optical antennas by building them through the use of focused ion beam (FIB) [165]. One of the main problems we faced was the slow throughput of the FIB process¹ and the variability in the quality of the Ge film that we were growing on oxide. As a result, we decided to switch to the silicon platform, primarily due to the commercial availability of high quality silicon-on-insulator (SOI) wafers. Our aim was to replace the Ge with Si and operate the detectors at lower wavelengths—around 800–900 nm where Si still absorbs. We also decided to use the electron beam lithography technique as it allowed us to fabricate many more samples per run than is possible with the FIB. We will start the chapter by highlighting the changes in the antenna design when one shrinks the wavelength from the 1300 nm range to the 800 nm range. Subsequently, we will explain the nano-fabrication process flow that we developed for the Si platform. Then, we will talk about the opto-electronic characterization setup that we built and provide measurement results from

¹We were using FIB twice: once to shape the Ge nanowire detector element, and another time to shape the metal into a dipole antenna.

the devices that we fabricated. Finally, we will conclude the chapter after a discussion of the measurement results.

6.2 Changes in the Design at 850 nm

Optical properties of metals depends on the wavelength of light. As described in Chapter 5, we fit the experimentally measured permittivity values for gold this time around the 800 nm band. In Figure 6.1 we plot the experimental values from [16] and also the fit we have using a four-pole Lorentz model with parameters as tabulated in Table 6.1. Compared to the longer wavelengths, we see that both the real and imaginary parts of the permittivity have decreased in magnitude. As a result, the surface impedance contribution $Z_s = \sqrt{\mu/\epsilon}$ increases and further reduction in the dipole resonance length is expected—further than a mere rescaling of the wavelengths. In Figure 6.2 we see that a 90 nm arm length for a dipole antenna with Si in between its dipole arms resonates around 880 nm. The ~ 90 nm range is the number to keep in mind when designing antenna integrated detectors at around $\lambda \approx 850$ nm.

	ω_{pm}	ω_m	Γ_m
$m = 1$	4.386227824E15	0.000000000E00	1.565488534E15
$m = 2$	1.008519648E15	1.874386332E15	8.109675964E14
$m = 3$	7.251716026E15	3.534954035E15	0.000000000E00
$m = 4$	1.332784755E16	0.000000000E00	0.000000000E00

Table 6.1 – Fourth order Lorentz fit to experimental permittivity values for Au around 850 nm.

6.3 Clean Room Fabrication

Fabrication of thin, 25 nm, metal rods of varying lengths, aligned to sub-wavelength pieces of silicon sitting on oxide was one of the main challenges that stood between us and working devices. This section will describe the techniques we used at the Stanford Nanofabrication Facility (SNF)² to overcome the fabrication barrier. Most of the pieces

²<http://snf.stanford.edu/>

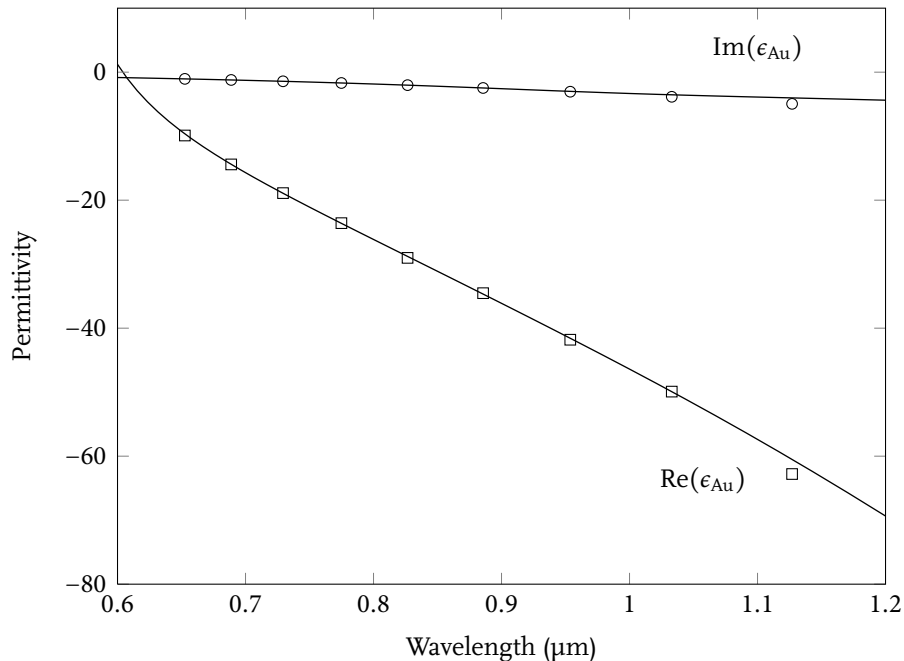


Figure 6.1 – Dispersion plot of the optical properties of Au at 850 nm. Symbols are experimental values from [16] and lines are the result of the fourth-order Lorentz-Drude fit.

of equipment at SNF have nicknames, and in the recipes and techniques to follow, we will make frequent use of those nicknames. Therefore, before we go any further, let us get acquainted with the names first.

Raith is the electron beam lithography system used. Its model number is 150. Raith can be used to expose photoresist with a beam of electrons to get high resolution features on surfaces and also as a high resolution scanning electron microscope.

AMT is a reactive ion plasma etcher. Its model number is 8100. It is mainly used to etch oxides and nitrides, but we use it to etch silicon.

P5000 is a magnetically enhanced reactive ion plasma etcher. It also has optical endpoint detection capability. Its model number is 5000 and the ‘P’ stands for ‘precision.’

Woollam is a spectroscopic ellipsometer which can be used to measure film thicknesses

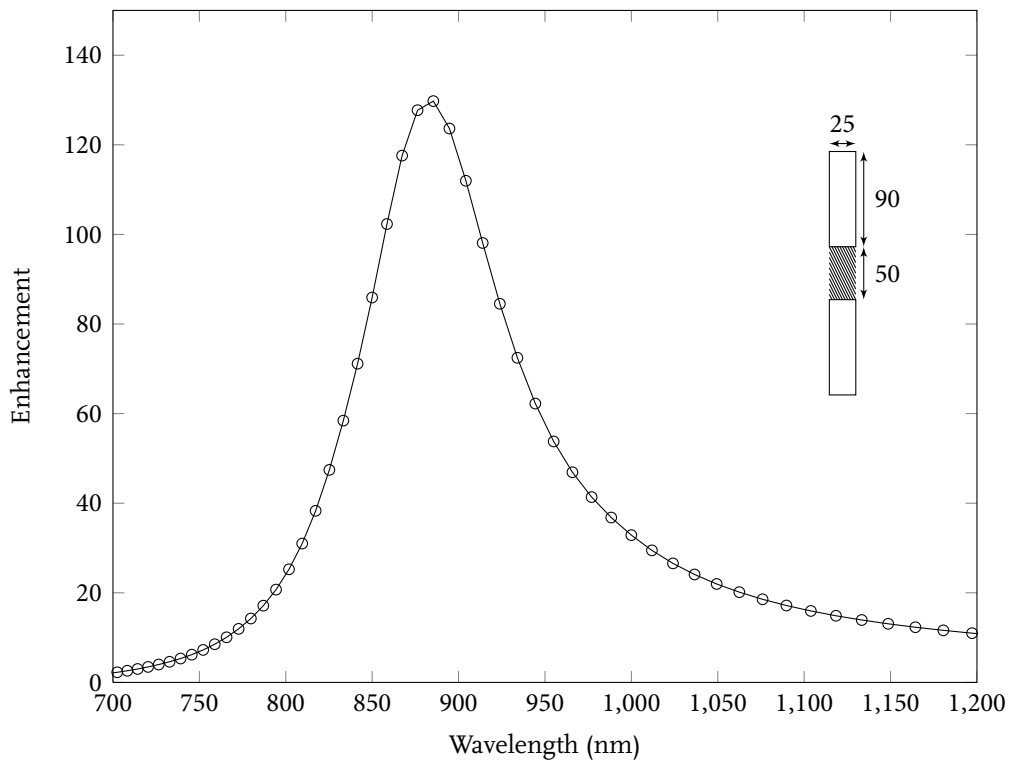


Figure 6.2 – FDTD simulation results for a bare dipole antenna on oxide, resonance at 885 nm. Each antenna arm is 25 nm wide, 25 nm thick, 90 nm long. In between the antenna arms, there is a 50 nm long Si cube shown as the crossed region in the inset.

and refractive indices. It works by sending light at different polarizations, frequencies and at different incidence angles to surfaces and by measuring the polarization and intensity of the reflected light. Its model number is M2000.

WBGen is the wet bench ‘general.’ The generality comes from the versatility of the chemicals allowed to be used at this wet bench. Many non-standard processing steps can be done at WBGen, though one needs to be extra cautious when using WBGen—usage of protective clothing and shielding is a must when handling, say, boiling sulfuric acid + hydrogen peroxide, i.e. *piranha*.

WBNonmetal is another wetbench. Samples that do not have any metals on them can be used here to clean their surfaces or etch them using hydrofluoric acid (HF).

WBDiff is the diffusion wet bench. Most of the furnaces that operate at high temperatures require an extra level of cleanliness which can be achieved through the use of the chemicals at WBDiff.

WBSolvent is the solvent wet bench. We mainly use it for lifting metal off of surfaces to define the nano-metallic structures (the technique is called *lift-off*).

Thermco is an oxidation furnace. It heats up samples to elevated temperatures where silicon surfaces start to oxidize. If the furnace has some water vapor during the oxidation, oxidation takes place much faster, though at the expense of a higher variability in the resulting oxide thickness—this is called *wet oxidation*. If there is no water vapor, then oxidation is much more slower, but the end thickness is more uniform—this is called *dry oxidation*.

Headway is a spin coater used to coat photoresist on samples. Samples are attached to a rotating head by vacuum, photoresist is applied on the sample by the help of a syringe, and pressing a foot pedal starts the rotation of the head. Based on the speed, the film thickness can be adjusted—film thickness is proportional to the square root of the rotation speed.

YES Oven is the baking oven where hexamethyldisilazane (HMDS)³ is also applied to the samples in it.

Innotec is a metal evaporator used to coat samples with thin layers of various metals. Its model number is ES26C. Precise measurement of film thickness is possible as the deposition is made.

SEMHitachi is an older but still functional scanning electron microscope (SEM). Its model number is S800.

Sirion is another SEM which actually resides in the Stanford Nanocharacterization Laboratory (SNL).⁴ Its model number is FEI XL30 and it has better resolution than SEMHitachi.

³a highly toxic chemical used to increase adhesion of resists to surfaces, especially to oxide

⁴<http://snl.stanford.edu/>

After this brief introduction to the tools of nano-fabrication, let us now delve into the specifics of building photodetectors integrated with antennas.

6.3.1 SOI thinning

We start with soi wafers from SOITEC company with 340 nm of active device (i.e. silicon) layer on the top, 1 μm of SiO_2 layer underneath and the Si carrier wafer below. The wafer is lightly p-doped with $14\text{--}22 \Omega \cdot \text{cm}$ resistivity. The Si layer on the top is oriented in the (100) direction. The top layer is too thick for our purposes, therefore we start the process flow by oxidizing wafers at Thermco, and etching them at WBDiff using hydrofluoric acid (HF). We would like to reach a final Si thickness of ~ 80 nm and we do the oxidation in three to four steps. The first steps are done using wet oxidation and do the bulk of the oxidation. The last 1-2 steps are done using dry oxidation to provide us with a uniform Si thickness at the end. After each oxidation-HF etch step, we measure the thicknesses of the top SiO_2 layer and the Si layer underneath using Woollam. When the desired Si thickness is obtained, then we cleave the wafer into roughly 1 cm squares using a diamond scribe pen.

6.3.2 Shaping the Silicon

In order to be able to shape the thinned down Si layer, we need to first put a layer of e-beam sensitive photoresist, write on the photoresist using Raith, and develop the resist. The resist then acts as a mask when we put the sample into a plasma etcher, either AMT or P5000.

There are a couple options for the choice of photoresist. The main choice to be made is whether to use positive or negative tone resist. Positive tone resist is removed when it is exposed whereas negative tone resist is removed everywhere except where the exposure takes place. The main positive tone resist used for e-beam lithography is polymethylmethacrylate (PMMA), whereas Ma-N 2403⁵ is the negative tone one.

PMMA was more popular among the e-beam community at SNF, therefore, we started with the positive resist process. Our aim was to shape the silicon into a thin ($\sim 50\text{--}60$

⁵from Micro Resist Technology

nm) and long (many μm) line for each device. To be able to achieve that end result using PMMA one needs to etch away two large chunks of Si, spaced closely to each other. Our first attempts at trying to expose two large rectangles of uniform beam dosage, separated by $\sim 50 - 60$ nm failed: the two rectangles merged with each other due to the proximity effect seen in e-beam lithography—the scattering of electrons off of the substrate and therefore a fattening of the exposed areas due to this scattering. Subsequently, we decided to expose less where the line would form, and more at the peripheries, further away from where the line would be. In order to achieve that, we exposed the rectangular areas in line scans, progressively increasing the e-beam dosage as a function of distance—parabolically in our case.

Until we found the right dosage conditions, we ran into various problems. In Figure 6.3 we show some SEM images from our process development work. When we were able to pinpoint the right dosage and etching conditions, we could get much better results as illustrated in Figure 6.4.

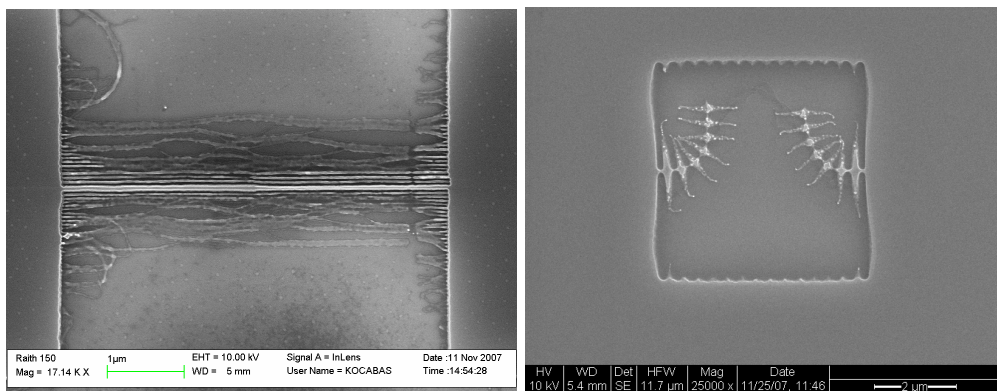


Figure 6.3 – PMMA based Si etch trials. The left picture shows an under exposed sample, and individual line scans on the PMMA were visibly transferred onto the Si after the etch. The right picture shows an interesting pattern which formed when we tried to form the Si line by vertical line scans as opposed to the parallel scan case of the left picture.

Initially, we were using P5000 to etch Si. However, a long downtime in P5000 and the subsequent changes in its etch characteristics made it very difficult to repeat the results of Figure 6.4 after P5000 came back on-line. As a result, we decided to switch to negative resist, and use Ma-N 2403 to define the thin long Si lines. The negative resist process turned out to be much more repeatable. In Figure 6.5 we show an SEM

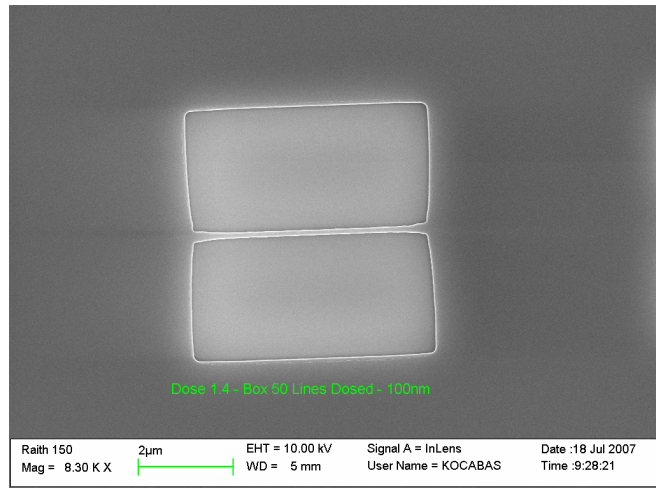


Figure 6.4 – Successful PMMA based Si etch when we found the right dosage condition. Note that the edges of the Si line show the proximity effect non-idealities.

picture of a 60 nm wide Si line. Figure 6.6 shows a cross section SEM image of a wider line. Line edges are rougher than we would like, but the repeatability of the process led us to stick with Ma-N.⁶

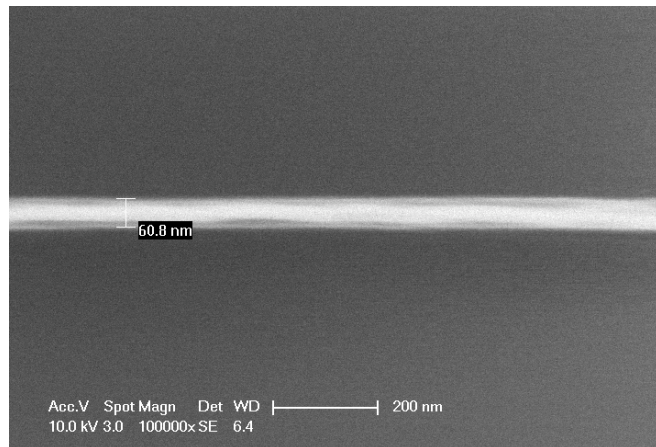


Figure 6.5 – Successful Si etch result using Ma-N resist.

⁶The astute reader who has looked into the details of the SEM pictures we provide in this subsection will realize that the dates on the SEM images do not correlate well with the story told. That is, the etch trial Figure 6.3 is dated later than the successful etch result Figure 6.4. In reality, it took us so much time and effort to reproduce the previous success of the PMMA work, that as a result our failures were much more glorious than those which took place during the initial process development, and hence our choice of the more extraordinary, though anachronistic, SEMs to illustrate possible failures one could face.

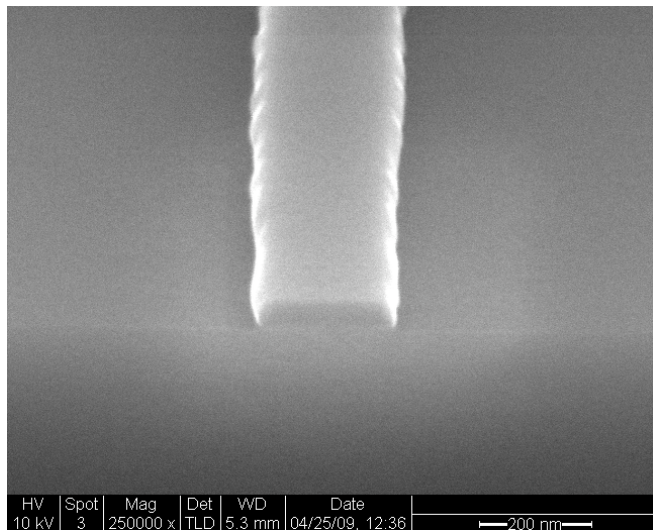


Figure 6.6 – Cross section SEM image of a thick Si line.

6.3.3 Crowning the Silicon with a Golden Antenna

In order to be able to pull out the photo generated electron-hole pairs in Si, we need to have an electrical contact to the Si line. Furthermore, we need to precisely align an antenna element to the Si line to enhance the local field concentration in the vicinity of the Si line in between the antenna arms. We use Raith to define both the metal contacts and the antenna elements. We choose the positive PMMA resist since we would like to minimize the amount of time spent on defining the shapes we want—it is much quicker to draw the two arms of the dipole antenna than to draw the area to be carved out.

The alignment problem is solved by writing alignment marks on the sample on the first layer. Before the second layer is written, the electron beam used to shape patterns on the surface, is scanned over the alignment marks to form an image around where the alignment marks are expected. Then, from those images, the center point of each of the alignment marks is deduced and that information is used to precisely calibrate the location of the features on the surface—the features of the first layer—to what is to be written on the second layer. In Figure 6.7, the cross shapes are the alignment marks etched onto the Si layer. The rectangular, bright spots on the alignment marks are the imaged areas before the second layer is written. There are two regions imaged per mark,

one horizontal and one vertical. The center locations of the vertical and horizontal scans give the exact location of the center of the alignment mark. Knowing the centers of the three out of four alignment marks that surround each device leads one to correct for any deficiencies in the positioning of the sample to get a layer to layer alignment precision of around 10 nm.

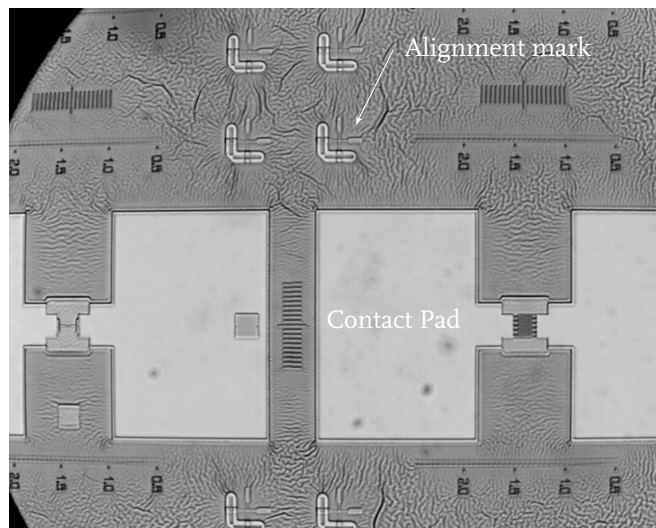


Figure 6.7 – Optical microscope image of an early prototype detector. The alignment marks are shown with the cross shapes. The sample is coated with Au after the development of the second layer resist. Lift-off will follow this step. Note the wrinkles on the Au layer which are due to the degassing of the PMMA in the low pressure evaporation chamber of Innotec.

After the second layer e-beam step is completed, PMMA is developed and then the sample is coated with gold. In between the two steps, it is important to bake the sample at 90 °C for 2 minutes so that no developer is left in the PMMA. Failure to do so leads to degassing during the metal evaporation which manifests itself with poor film quality following the deposition. The wrinkles in Figure 6.7 are a result of forgetting to bake the sample after development. It is also important to set the parameters of Raith right, otherwise, bizarre dosage problems might occur. One such example is shown in Figure 6.8 where the metal which was supposed to be a continuous film turned out to be a collection of little dots. The problem here was the very large step size used when writing areas with the e-beam: areas are written as a combination of a large number of ‘dots’ and if the dots are far away from each other they no longer form a continuum.

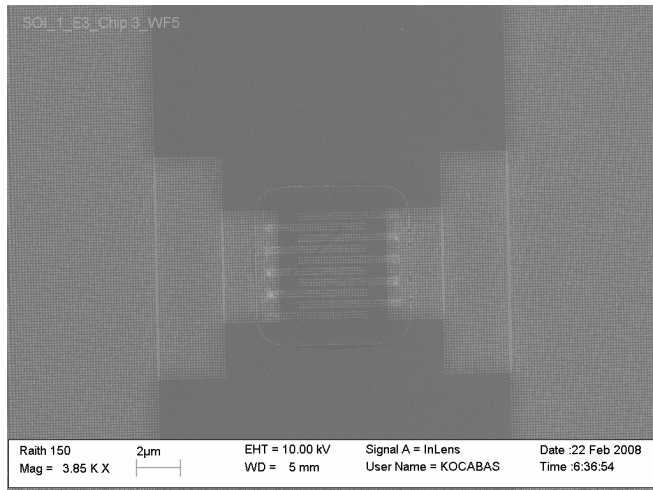


Figure 6.8 – Bizarre metal dosage problem which led to a dot array instead of a continuous metal film. The underlying pattern is that of a fingered metal-semiconductor-metal detector which we use to debug our process flow.

Once all steps are done correctly, one gets very good alignment of the metal layer to the underlying silicon. In Figure 6.9 we show an SEM image of a sleeved dipole structure. In Appendix D we provide a detailed recipe of our process flow. Now, though, it is time to talk about the measurement setup.

6.4 Opto-Electronic Measurement Setup

After we fabricate our devices, we test them by shining light onto the detectors and by measuring the photocurrent generated under various lighting and electrical biasing conditions. The optical portion of the setup is an infrared microscope which allows precise control over the polarization state of the laser light that illuminates the sample. The electrical portion applies a voltage bias and measures the dark current as well as the photocurrent. Due to the very small volume of the detector elements, proper shielding of electrical connections turn out to be quite important. The mechanical part is responsible for aligning the sample right at the peak intensity point of the illumination region. In this section, we will go through each portion (optical, electrical & mechanical) and describe their properties.

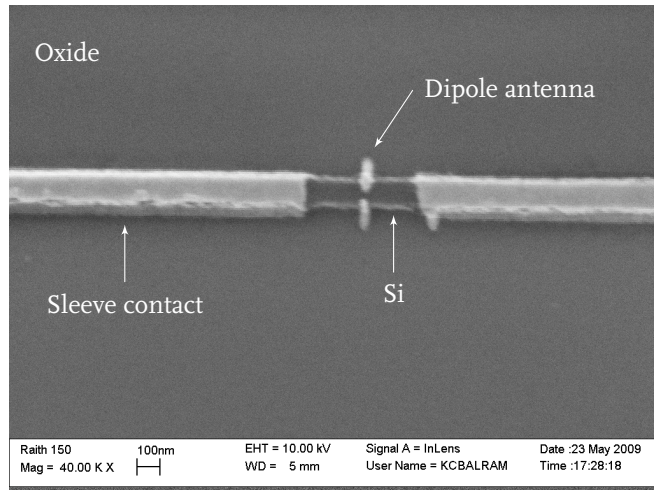


Figure 6.9 – Long Si lines and the antenna with sleeves on the top. The bright parts are gold and the horizontal line is Si. The underlying material is oxide.

6.4.1 Optics

The light source that we use is a titanium-sapphire solid state mode locked laser.⁷ The laser is pulsed and the pulse width is on the order of 100 fs. Even though the laser is tunable over a frequency range of roughly 800 – 900 nm, we mostly use the laser at a fixed wavelength of 850 nm. In Figure 6.10, we sketch the optical setup. The laser light is guided to the setup with dielectric mirrors, and then the beam passes through a Risley prism pair. The Risley prism allows us to steer the beam to an arbitrary direction, and we make use of the Risley prism to make sure that the beam enters at a normal angle to the microscope lens.

After the Risley, the beam goes through a neutral density (ND) filter wheel that we use to adjust the light intensity. Two non-polarizing beam splitters (NPBS) are then used in the beam path for imaging through a charge-coupled device (CCD) camera and for illuminating the sample with an 850 nm infrared light emitting diode (LED). We use a Tamron zoom lens to image the sample onto the CCD. An 850 nm polarizer and a matching half-wave ($\lambda/2$) plate from Meadowlark Optics is used to polarize and to rotate the polarization state of the incoming light. We use a Mitutoyo M Plan Apo NIR 20x

⁷More specifically, the mode locked laser is a Spectra Physics Tsunami model and it is pumped with a Millenia series diode laser.

long working distance objective lens to focus the light onto the sample. The objective lens has a numerical aperture of 0.40. By focusing and de-focusing the laser spot, and by adjusting the angular position of the beam through the help of the Risley prisms, we get a circular, stigmatization-free focused spot on the sample. We found that it was best to set the polarization state of the beam right before the beam enters the objective lens—bouncing the beam off of dielectric mirrors or letting the beam go through beam splitters turned out to be detrimental to the polarization state of the light.

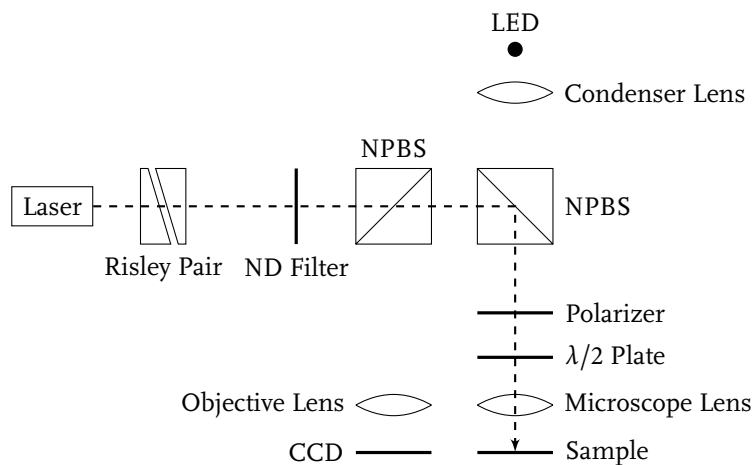


Figure 6.10 – Optical setup used in the measurements. ND stands for neutral density, NPBS for non-polarizing beam splitter, CCD for charge-coupled device, LED for light-emitting diode.

6.4.2 Electronics

The electrical requirements are fairly simple: apply a voltage bias to the detector, and measure its photo response. The catch is, due to the low levels of available photo response of the detectors, noise elimination turns out to be quite important. In Figure 6.11 we sketch the electrical part of our measurement system. We use Model 79 triaxial probe holders and matching probe tips from Micromanipulator to electrically contact the photodetectors. Measurement of the photocurrent requires us to use a lock-in amplifier⁸ to filter out the noise from the system. We use a mechanical chopper to chop

⁸Stanford Research Systems Model SR830

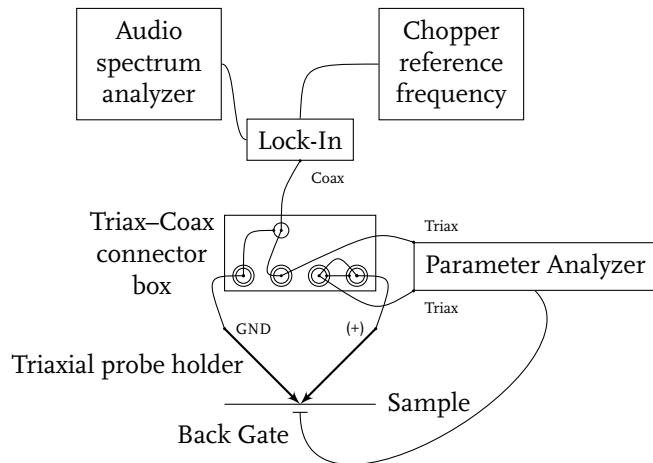


Figure 6.11 – Serial electrical connection between the sample, the lock-in and the parameter analyzer through the help of the triax-coax connector box.

the light, and feed the chopper frequency signal to the lock-in to filter out the noise. We connect the monitor output of the lock-in to an audio spectrum analyzer⁹ to see the noise spectrum of the electrical system and choose a chopping frequency near where the noise is minimal. Voltage biasing of the sample is done through a parameter analyzer.¹⁰ The parameter analyzer has triaxial connectors whereas the lock-in has coaxial (BNC type) inputs. We built a triax-coax shielded serial connection box to connect the sample to both the parameter analyzer and the lock-in amplifier's current input channel.¹¹ The parameter analyzer is also used to gate the detectors through the back of the samples. We put the samples on an electrically isolated conducting tape, and connect the tape to a voltage output channel of the parameter analyzer. Furthermore, the parameter analyzer is also used to measure the dark current as a function of applied voltage. We wrote Matlab scripts to talk to the lock-in and the parameter analyzer through their GPIB ports in order to set electrical biasing conditions, read the measurement results

⁹HP 3580A

¹⁰Agilent 4155C

¹¹The photo detectors have a very high impedance on the order of many gigaohms, and the low impedance current input channel of the lock-in provides the lowest noise when making photo current measurements. The parameter analyzer has a teraohm level voltage source impedance—much larger than the photodetector impedance as required from a proper voltage source.

and save the results in a human-readable ASCII data file.

6.4.3 Mechanics

All optical parts in Figure 6.10 are mounted on Linos Microbench opto-mechanical components. The sample is held horizontally, and the beam is routed above the sample, just as done in a regular microscope setup. The microscope objective is attached to a turret, and the long working distance of the objective lens allows the probe holders to contact the sample without interfering with the imaging properties of the optical system. The sample is mounted on a piezo stage with 20 μm of travel in \hat{x} , \hat{y} and \hat{z} directions. The piezo stage itself sits on a Newport three axis mechanical translation stage. Probe holders are attached to Rocker&Kolls Model 448 manipulators and the manipulators are attached on top of the piezo stage so that the sample can be moved by the piezo while making measurements.¹² We used the machine shop to build various parts used to attach different components together.¹³

6.5 Measurement Results and Discussion

We made measurements on different samples to electrically characterize the photo response of our detectors under various illumination and biasing conditions. Our main aim was to build a set of detectors with different antenna elements, or none at all, attached to them and to measure their properties in order to have an electrical characterization scheme for photo detectors integrated with nano-metallic scatterers. We were inherently assuming that comparison of different devices on the same sample and on different samples would be simple to achieve. After all, we would be judiciously applying the same clean room techniques for fabricating our samples.

However, our initial attempts failed. After the subsequent literature surveys, we realized that the devices we were making were very similar to the popular nanowire

¹²The piezo has a 1 kg weight limit, and that led us to use very light manipulators. Rocker&Kolls ones were the lightest we could find.

¹³We thank Mehmet Solyali at the Varian Physics Machine Shop for teaching us the basics of machining.

based structures—a plethora of papers are available on various properties of nanowires.

Due to the small diameter of the nanowires, the surface to volume ratio of devices made out of nanowires is exceptionally high compared to bulk structures. Therefore, many effects that could have previously been neglected become critical in understanding the measured nanowire properties. Let us start with the current-voltage characteristics and, in general, the transport of carriers within nanowire structures.

6.5.1 Transport

There are various techniques to electrically measure the properties of nanowires—many of which are described in detail in [166]. Current-voltage measurements are one of the easiest ways to test the quality of devices with nanowires. The properties of the nanowire surfaces and the way in which contacts are made to the nanowires have profound effects on the current-voltage measurement results.

Surface States

As-grown nanowires are known to have dangling bonds on their surfaces which act as charge traps. As charges are trapped on the surface, surface depletion takes place which leads to band bending at the surface [167]. If nanowires are fabricated using a top-down technique, such as e-beam lithography, surface effects are amplified due to the etching process which results in roughness—therefore more carrier scattering—and sensitivity to ambient conditions due to adsorption effects [168]. The most prominent signature of surface effects is the hysteresis observed on current-voltage plots of nanowires.

In Figure 6.12 we show a typical current-voltage plot for a device as in Figure 6.9. The current was limited to 100 nA, and the arrows in the figure show the direction of the voltage sweep. As can be seen from the figure, scanning the voltage in different directions lead to different current-voltage curves, a standard form of hysteresis.

One way to reduce the hysteresis is to oxidize the nanowires in order to decrease the number of dangling bonds at the surface. The Si-oxide interface is well studied for planar geometries and oxidation models for different crystal orientations have been developed [169, Sec. 6.5.5]. It was found that the (100) direction of the Si crystal leads

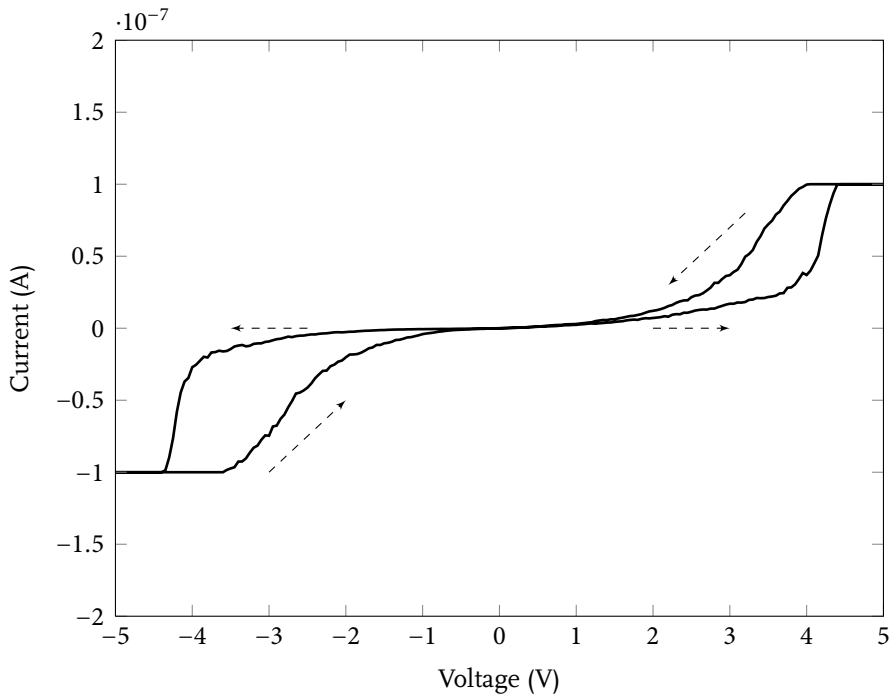


Figure 6.12 – Hysteresis in the dark current-voltage plot for a Si photo detector.

to the best Si-oxide interface, and therefore most of today's electronic circuitry use (100) oriented wafers. However, for nanowires the situation is more complicated. There is no single crystal orientation on the surface, but rather, all different directions are present as one circulates the wire radius. Indeed, oxidation was shown to anisotropically decrease the radius of nanowires defined by e-beam lithography [170].

In the case of nanowires, oxidation rates were shown to be dependent on the wire radius [171, 172]. Oxidation under the right conditions was shown to decrease the hysteresis effects [173]. Another way to eliminate the effects of hysteresis is to scan the voltage in a very slow manner, so that the carriers trapped on the surface have enough time to conclude their transport through the nanowire [174]. However, when we tried to sweep the voltage slowly, we did not see a significant decrease in the hysteresis, which suggests that the carrier lifetimes at the trapping sites of our samples are relatively long.

Contacts

Most of the devices that we fabricated show back-to-back Schottky type contacts as can also be inferred from Figure 6.12. However, a non-negligible number of the devices showed a single-sided, diode-like current-voltage relationship. Such asymmetrical I-V curves are also observed by others and are associated with the difference in the quality of the contacts on both sides of the wire [175].

We tried to extract the contact resistance in our devices through the use of the 4-point contact technique [176]. However, the fact that each contact significantly changes the transport properties and that the 4-point technique works only for ohmic contacts resulted in the failure of our measurements. As quoted in [177], “a gated four-point measurement would not give the intrinsic nw resistivity because additional band bending would be introduced at the inner contacts and thus the measurement would be corrupted.” Nevertheless, contact resistance measurements were made by others through the investigation of temperature dependence of I-V curves [178].

Schottky contacts to nanowires were investigated by different groups, and as quoted in [179] it was seen that “electronic transport properties of nanoscale contacts can differ significantly from those of their bulk counterparts.” For instance, for contacts smaller than a characteristic size, reverse currents were shown to dominate the transport properties, fundamentally changing the Schottky characteristics [180, 181].

Gating nanowires through a non-conducting contact turns a nanowire geometry into a field effect transistor (FET). The easiest way to gate a nanowire is to place the wire on an oxidized silicon substrate and to use the substrate as the gate electrode. In the case of lithographically defined nanowires, the same effect can be obtained by using soi wafers. However, this type of gating is not the same as gating in regular FETs, as the gate also overlaps the source and drain regions, and affects the Schottky barrier height [182]. Due to the possible presence of very high fields and associated large band bending in nanowires, tunneling effects should also be taken into consideration in order to calculate the transport properties [183, 184].

In Figure 6.13 we show the effects of gating on the current-voltage relationships on one of our samples. Note that there is a micron thick oxide between the conduction

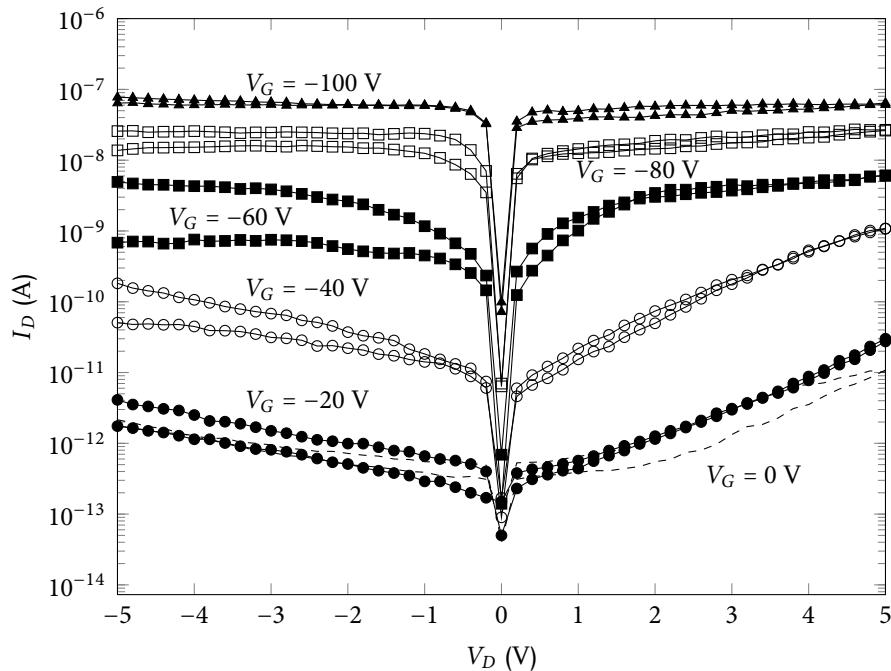


Figure 6.13 – Effects of gating on the voltage-current relationship. Dashed line is the $V_G = 0$ curve where V_G stands for the gate potential applied through the back of the carrier substrate.

channel and the position where the gate potential is applied.¹⁴ As can be seen from the figure, we can tune the conductance in the channel region through the application of the gate potential. Note that the hysteresis is still visible at various gating potentials.

Schottky-to-ohmic conversion of the contact characteristics through the help of annealing was shown to be achievable in GaN nanowires [185]. For Si nanowires Ni was shown to have lower contact resistance than Ti contacts, and annealing was seen to help with the I-V characteristics [186]. Ion beam doping of nanowires was also tried, and it was possible to get ohmic contacts—though hysteresis effects were seen to increase due to induced defects during the doping process [187, 188].

Having large contact areas, especially when defining the nanowire geometry through the use of e-beam lithography, seems to help with having reliable contacts both for back gated FETs [189] and FETs gated from the top, within a limited region of the transport

¹⁴In reality, we apply the gate potential through the back of the carrier wafer which has the same low doping as the active region. Therefore, it is very conceivable that some of the voltage drop occurs at the ~ 500 μm thick carrier wafer.

channel [190]. In these examples, the channel is in the form of a nanowire, and it connects to large rectangular patches of contacts for the source and drain regions. For large contact areas, doping of the source and drain regions becomes much easier and size effects are minimized.

High fields within the nanowires may lead to depletion widths larger than the length of the channel. At such high fields punchthrough occurs, and super linear I-V characteristics can be observed—this is also called *space charge limited current* [191]. In [192, 193] space-charge-limited current and the effects of trap levels on the I-V characteristics are discussed in detail. One intriguing feature of space-charge-limited current is the way in which it resembles avalanching. Temperature dependence of I-V characteristics is one way to differentiate between these two different effects [194]. Lastly, it was shown that ballistic transport and different scattering mechanisms can lead to kinks in the I-V curves [195].

6.5.2 Photoresponse

Nanowire light absorption is polarization dependent [196]. When the electric field is parallel to the wire, due to the continuity of tangential fields, the field inside and outside the nanowire are equivalent to each other. However, when the electric field is perpendicular, this time the displacement field, $\mathbf{D} = \epsilon\mathbf{E}$, is continuous and since the permittivity of the wire is larger than the surrounding environment, field inside the wire will be less.

When we measured the photocurrent of our samples as a function of the applied source-drain potential, we observed plots similar to those in Figure 6.14. In our measurements, we apply polarized light to the device, move the device with the piezo stage until the photo current reading is maximized at the lock-in and then sweep the voltage to record the photo current as a function of drain-source voltage. Our detectors show a strong polarization dependence: photocurrent is larger when light is polarized along the long Si wire direction.

Contacts are shown to have profound effects on the photo response of nanowires.

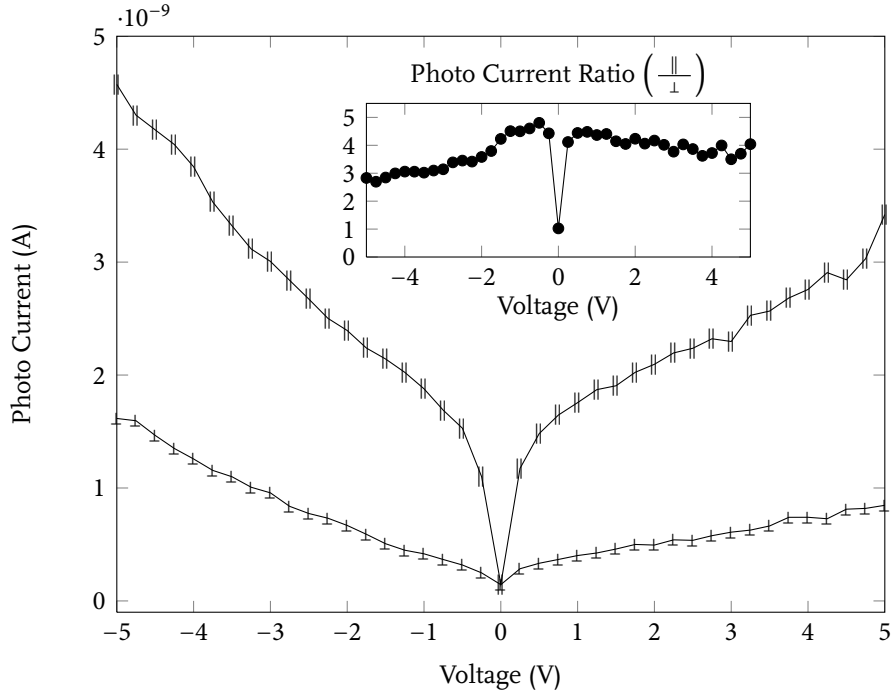


Figure 6.14 – Photocurrent as a function of parallel (\parallel) and perpendicular (\perp) polarization. $V_G = 0$ in these plots. Inset shows the ratio of the two currents as a function of voltage.

When the contacts to the nanowire are of the Schottky-type, most of the applied source-drain voltage drops across the reverse biased Schottky contact and the photo generated electron-hole pairs in the vicinity of the reverse biased contact are efficiently swept [197]. However, those electron-hole pairs generated away from the reverse biased contact do not observe significant fields and therefore they recombine before being swept away [198].

We built test samples with only a long Si line (no antennas) connected at its both ends to large metal pads. In Figure 6.15 we show the dark current as well as the photocurrent readings when we sweep the drain-source voltage at a fixed gate voltage of $V_G = -50$ V. From the figure we see typical Schottky-type photo current characteristics: as the reverse bias across the junction increases, the photocurrent saturates to a maximal value, and at forward biases photocurrent is negligible. The hysteresis effect is also visible in the figure.

Our main aim was to measure the antenna properties, and the antennas perform

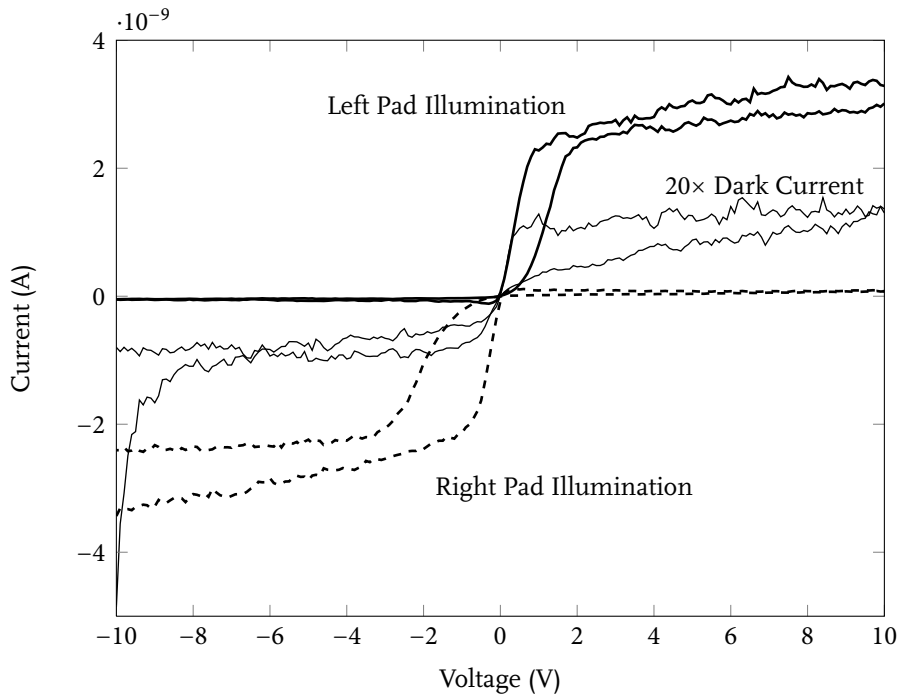


Figure 6.15 – Effects of contacts on photocurrent characteristics. A gate bias of $V_G = -50$ V is applied. The dark current is multiplied by 20 so as to make it visible in the plot.

best when the light polarization is parallel to the dipole arms, that is, perpendicular to the Si nanowire that goes through the antenna gap region. Unfortunately, for those detectors as shown in Figure 6.9 we did not observe a significant difference in the ratio of the photocurrent due to light in orthogonal polarization directions. We got similar figures as shown in the inset of Figure 6.14 for those samples with and without antennas. There can be two reasons for this behavior: a) the effective Schottky contact is away from the antenna, and therefore photo generated carriers near the vicinity of the antenna are not collected, b) finite thickness of the metal layer on the Si nanowire is not sufficient to block the light, and the photo current signal of the antenna is swamped by the absorption through the microns-long nanowire section.

In order to decrease the inherent polarization dependence of the photo detectors without antennas—so that when we put the antennas around the detector volume, antenna effects would be easier to measure—we built samples with modified Si geometries. In one set of devices, we reduced the length of the original Si line such that the

line would only be couple hundred nm in length. Having a short Si line also reduces the possibility of the nanowire photocurrent swamping the photocurrent due to the antenna. Figure 6.16 shows the SEM images of the samples with the short Si lines, with and without antennas.

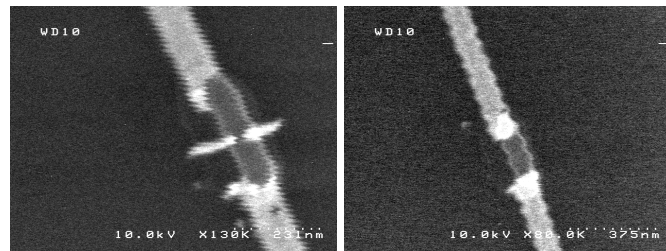


Figure 6.16 – Short Si detectors with an antenna (left) and without an antenna (right).

The photocurrent response of the short Si lines without antennas did still depend on the polarization with varying degrees of strength. We were not able to conclusively demonstrate the antenna effect due to the large variation in the current-voltage characteristics both for dark measurements and measurements with light—reliably contacting such a small volume of Si turned out to be a great challenge. However, some devices did show quite promising results. In Figure 6.17 we plot the photocurrent response of one of the short Si detectors as a function of light intensity. At high field values, the photocurrent increases for a fixed light intensity, suggesting the presence of a gain mechanism.

Different photo-induced gain mechanisms have been reported in the literature. One mechanism is due to the surface band bending. When electron-hole pairs are generated by photons, due to the surface band bending, holes go towards the surface and get trapped at the dangling bonds, whereas electrons go to the core of the nanowire. The presence of holes on the surface effectively changes the gate potential of the wire (photogating), whereas the electrons at the core act as extra dopants (photodoping) [199–202]. At high voltages, there is enough field away from the reverse biased Schottky contact to sweep the photo generated carriers in the non-Schottky region away, and the gain mechanism becomes observable on the I-V plots. Of course, another plausible explanation is avalanching due to the presence of very large fields. Temperature dependent current measurements can differentiate between the two possible explanations.

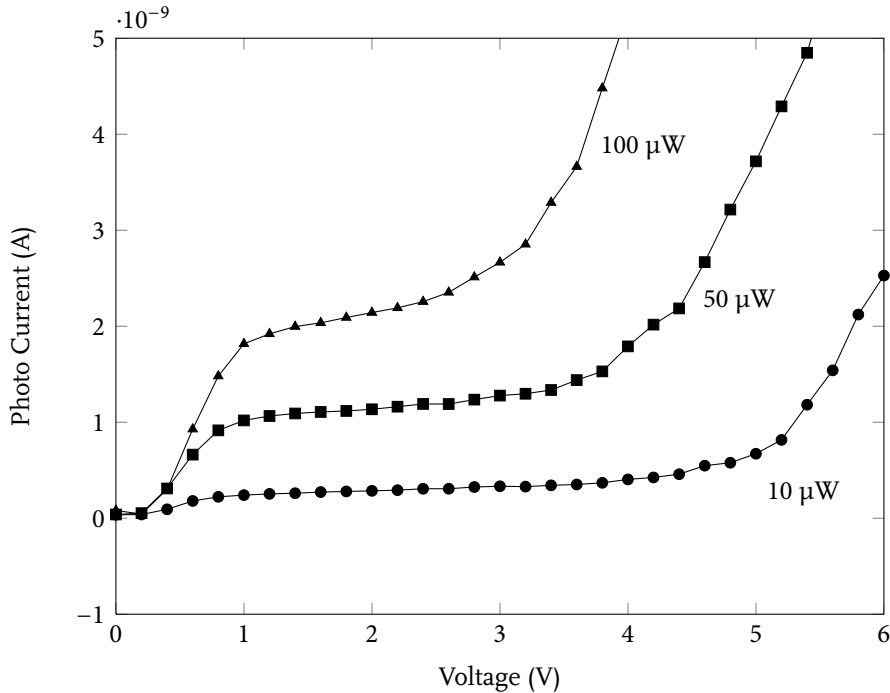


Figure 6.17 – Photo current as a function of light intensity for short Si detectors. The labels show the power in the light beam measured right after the ND filter wheel. Actual power that hits the sample is roughly 10% of the measured power.

It is worthwhile mentioning that if we were to have ohmic contacts, then we would not need to have the antenna element near where the reverse biased Schottky contact is. As shown in [203], nanowires with ohmic contacts can have substantial photocurrent even in the mid section of the wires, away from the contacts. And more interestingly, the location of the maximum photocurrent contribution can be tuned by the choice of the source-drain bias voltage. Furthermore, it was also shown that polarization dependences of photocurrent generated at the reverse-biased Schottky regions and at regions where the nanowire acts as a photoconductor (away from the reverse-biased Schottky contact) are different [204].

Another set of devices that we fabricated had the long Si line turned into a circle as shown in Figure 6.18. Our aim was to minimize the polarization dependence of the Si nanowire to make the antenna contribution more visible. When we measured the photo-current of the circularly shaped detector elements without any antennas, we observed that the photocurrent did not depend on the polarization of the incoming light

as we expected. However, those samples with antennas did not show any statistically significant increase in the photocurrent. In our measurements, we first maximize the photocurrent at a given polarization and then sweep the source-drain voltage to get curves as in Figure 6.14. It is very likely that the maximum photocurrent position was near where the reverse bias Schottky contact was, and thus we were not able to observe the antenna enhanced photocurrent. If we were to have ohmic contacts we could circumvent this problem. Another possibility is to get photocurrent vs position images as done for instance in [203] for different polarizations, and to calculate the ratio of two images to see where the ratio would maximize. If the maximum location is where the antenna is, then we will have showed what we were looking for.

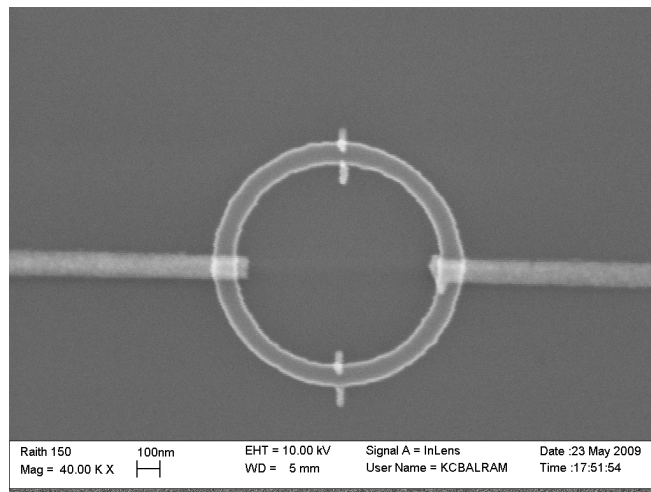


Figure 6.18 – Circular detection element.

Lastly, we would like to briefly talk about the finite thickness of the oxide layer that we had in our SOI wafers. As elaborated in [205], choosing an oxide thickness that minimizes the reflections of electromagnetic waves coming from the air side improves antennas' detection capabilities. In Figure 6.19 we plot the intensity reflection coefficient¹⁵ of a plane wave coming from the air side to an air-oxide-Si three layer system. The plane wave is coming perpendicularly to the surface. The calculation is made through the use of the transfer matrix technique, though for a three layer system closed form formulas also exist. We plotted the intensity reflection coefficient for two cases: one

¹⁵which is the magnitude square of the reflection coefficient for fields

for the Si detectors designed to work around $\lambda = 850$ nm and another for the Ge-based photodetectors of [165] which were resonant around $\lambda = 1400$ nm. As can be seen from the figure, the reflection coefficient is close to minimum for 1 μm oxide thickness when $\lambda = 850$ nm, but it is close to its maximal value for $\lambda = 1400$ nm. In all our designs, we were assuming an infinite oxide thickness due to the limited computational power that we had for our FDTD calculations. We observed the antenna effect on Ge based detectors fabricated on 1 μm thick oxide. The fact that the reflection coefficients are at opposing regimes for the 850 nm and the 1400 nm wavelengths for a fixed oxide thickness, suggests that a thorough investigation of the antenna properties sitting on a finite oxide thickness might prove useful.

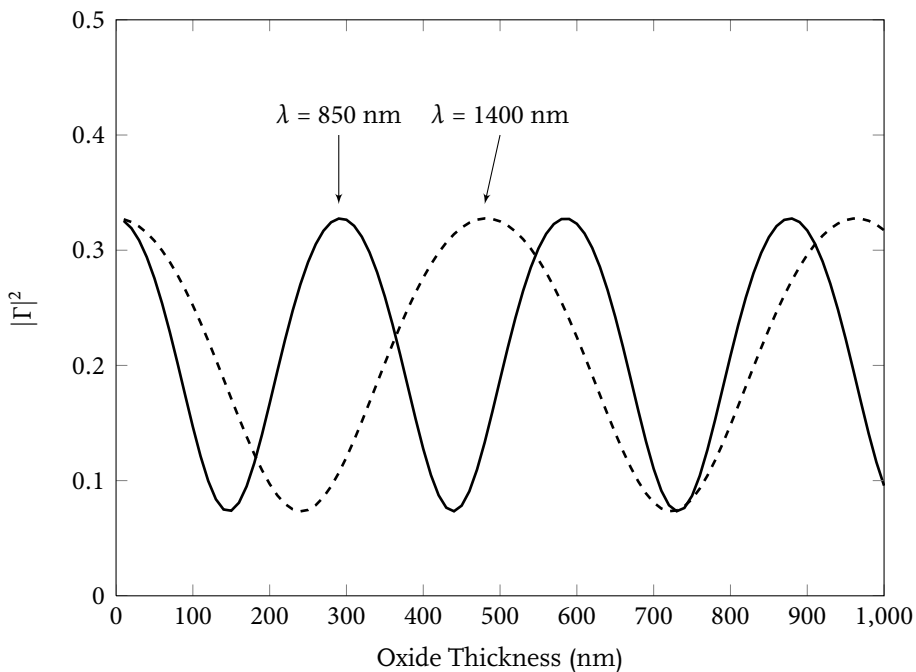


Figure 6.19 – Intensity reflection coefficient from an air-oxide-Si three layer system as a function of oxide thickness. Solid curve is for $\lambda = 850$ nm and dashed curve is for $\lambda = 1400$ nm.

6.6 Concluding Remarks

In this chapter we summarized our efforts at fabricating and measuring antenna-integrated Si photodetectors using electron beam lithography, and compared and contrasted our results with the relevant literature on nanowire detectors and field effect transistors. We were not able to conclusively show the antenna effect in photodetectors, but throughout our efforts we believe we made progress on understanding the carrier transport in and photo response of deep sub-wavelength volumes of Si. Surface effects and contacts are critically important in understanding the properties of sub-wavelength photodetectors. By appropriate surface passivation, and having ohmic contacts via doping and contact annealing, many of the problems we report in this section can potentially be solved. Additionally, it would be very illuminating to have photocurrent maps of the detector geometries as a function of position, wavelength and polarization—which is within our measurement capabilities—to be able to characterize the antenna integrated photodetectors for near-infrared frequencies.

સુ

Chapter 7

Conclusion

OPTICAL NETWORKS form the backbone of the communications infrastructure of the world. The ability to send immense amounts of data through very long distances with minimal loss is what makes it possible to watch videos online, listen to radio shows on the other side of the planet and to discover new forms of self expression through the creative technologies of the ‘information age.’ In addition to being able to send information around, the capability to create new content, to process the generated data and to store it indefinitely is crucially important to be able to taste the fruits of technology in our daily lives—so that we can blog about various topics, look up Wikipedia when need be, read the news, be a part of lively discussions on email lists etc.

On the information processing side, electronic circuitry in our gadgets is using more and more energy to be able to communicate with the outer world. It now takes as much—and sometimes even more—energy to send the information around by moving electrons in the electrical cabling that connects to the switching transistors (also known as the *interconnect*), as it does to process the information by switching transistors on and off. The fact that we cannot cool the electronics fast enough, bounds the amount of energy density that can be dissipated in a chip and therefore the speed of electronic circuitry. Loosing a significant portion of the energy to heat in the transport of electrons is one of the main factors that limit the speed of electronics.

The use of optics in the transfer of information is proliferating. Whereas previously it was only distances measured in thousands of kilometers—from one continent

to another—between which it was economically feasible to use optics, advances in technology led to the use of optics to replace the electrical cables in the back-planes of high speed switches used in today’s internet backbone. Could it be that we can also use optics at shorter length scales, to connect chips to each other, or even, to send bits from one corner of a single chip to the other? The question has long been on the agenda of many, and the idea of using optics in cmos compatible electronics is gaining a lot of attention recently [206].

Successful integration of optics into electronics will have stringent requirements: $\sim 10 \text{ fJ/bit}$ energy to transfer information, photodetectors with a couple femtofarads of capacitance, clock rates of tens of GHz, a well understood and densely integrable waveguide technology and wavelength-division multiplexing among others [9]. Furthermore, modeling techniques that can potentially predict the collective operation of millions of devices are crucial to be able to design complicated, multi functional opto-electronic components.

We started this dissertation by analyzing different nano-metallic, i.e. *plasmonic*, waveguide geometries that can be packed densely to each other. We focused on the metal-insulator-metal (**MIM**) geometry, and in detail analyzed the modes that the **MIM** waveguide supports. We showed that **MIM** waveguide modes are a hybrid of the parallel plate and dielectric slab waveguide modes: they include an infinitely large set of discrete modes as in the parallel plate case, in addition to a continuum set of modes analogous to that of the dielectric slab’s. Deep subwavelength guiding properties of the **MIM** waveguides make them suitable for use in applications where light needs to be focused to volumes similar to those of today’s transistors, tens of nanometer cubes.

We extended the mode-matching calculation technique, frequently used in the microwave domain, to analyze junctions of **MIM** waveguides. Our understanding of the modal properties of the **MIM** structure was crucial in this respect. We then mapped the modal scattering characteristics of **MIM** junctions into a much simpler representation through the use of the scattering matrix approach. We showed how to analytically design mode converters that can act as a bridge between the modes of conventional dielectric waveguides and those of the deep subwavelength nano-metallic structures. We illustrated how technologies of the microwave domain can still be of great use for optical

design through our use of various microwave concepts and methods such as the Smith Chart and the development of an exact equivalent circuit for MIM junctions. Conceptualizing scattering of electromagnetic fields as equivalent voltages, currents and relevant circuit parameters led us to significantly reduce the amount of time necessary to calculate the coupling between MIM waveguides.

We then switched gears, and shifted our focus to very low capacitance photodetectors. In order to lower the capacitance, the semiconductor volume in the detector was made even smaller than a cubic wavelength. When detectors are made so small, it becomes harder to get the light to couple to the detecting volume. We again borrowed a concept from the microwave/radio-frequency domain and decided to surround the detector volume by an antenna which would resonate at the wavelength of our laser, around the 1300 nm band.

Properties of metals greatly change as the frequency of operation is tuned from microwaves to the optical range of hundreds of THz. Design rules valid at microwave frequencies need to be re-evaluated and modified for the optics regime. We designed an antenna integrated photodetector, based on the topology of the open-sleeved dipole from microwave frequencies. We used the sleeves to bias and to collect the photocurrent generated at our deep subwavelength semiconductor volume positioned between the arms of the dipole element. The dipole element resonated at the design wavelength and concentrated light into the volume of the detector and hence enhanced the intrinsic photo response of the detecting volume. We experimentally verified our simulation results through the use of Ge on oxide samples with antennas on them, fabricated by the help of the FIB technique.

The last part of the dissertation focused on the experimental work we conducted. Ge-based antenna integrated photodetectors showed a lot of variation from one sample to another due to the annealing process we were using to crystallize the Ge. We switched to Si, and used SOI wafers as the starting material in our subsequent fabrication steps. We used electron beam lithography and plasma etching to define the subwavelength structures on our samples—and this time we fabricated designs which would resonate around 850 nm, where Si still absorbs. In order to be able to test our devices, we built opto-electronic measurement setups with precise control over the polarization state of

light hitting the sample and with low noise electrical contacts so that we could measure any small amount of photocurrent generated in our samples.

Effects related to the surface quality of the etched Si lines, and the properties of contacts to small volumes of Si prevented us from making conclusive measurements about the effects of antennas around Si detector volumes. However, we were able to fabricate Schottky contact field effect transistors by back gating our samples. We observed polarization dependent photocurrent from our samples. Furthermore, we fabricated samples that would make it easier to observe the antenna effect: samples with a short Si element, and those with a circular Si region. After developing the fabrication recipes to reliably connect to small volumes of Si, and following an effective Si passivation, we believe that we will be able to make more conclusive measurements.

During our work, some interesting questions occurred to us:

1. What are the architectural requirements for optical interconnects for chip to chip connections? What sort of topologies would fit those requirements the best?
2. Antennas are useful for converting the energy in one mode of a waveguide to a radiation mode directed in a specific direction. What is the shape of an antenna that best matches the given optical mode of a laser for guiding the light into a given mode of a specific waveguide?
3. What sort of fabrication techniques lead to reliable electrical connections to nanometer scale volumes of silicon?
4. Nanowire geometries can easily be turned into field effect transistors by putting a gate on the wires. Would it be possible to integrate such a transistor intimately with a photodetector with antennas around it?
5. Would it be possible to take advantage of two-photon-absorption in Si to design photodetectors that work at longer wavelengths?
6. How do confinement of carriers and field enhancement interact with each other? If one were to build an antenna around a quantum dot, would it be possible to tune the optical properties of the quantum dot in any way that is not possible otherwise?

It is our hope that this dissertation will contribute to the efforts to further the research on optics of subwavelength geometries and devices. We look forward to learning more about the subject matter, and wish that some of the questions raised above will be answered soon.

Stanford, CA
September 2009

સુ

Appendix A

Overview of Maxwell's Equations for Guided Modes

In this section, Maxwell's equations will be summarized for the case of waveguides with waves that propagate in the \hat{z} direction. Waveguides are formed by a permittivity profile $\epsilon(x, y)$ which is independent of z . Also $\epsilon(x, y)$ is assumed to be a discontinuous function of x and y composed of regions with fixed permittivity values. Therefore it is possible to separate the field into transverse and longitudinal components as $\mathbf{E} = \mathbf{E}_\perp + \hat{z}E_z$ and $\mathbf{H} = \mathbf{H}_\perp + \hat{z}H_z$. Furthermore, it is possible to decompose the gradient operator as $\nabla = \nabla_\perp + \hat{z}\partial_z$. With those definitions, one can get the following from Maxwell's equations with the time harmonics dependence of $e^{+j\omega t}$:

$$\nabla \cdot \mathbf{D} = 0 \rightsquigarrow \nabla \cdot \mathbf{E} = 0 \rightsquigarrow \nabla_\perp \cdot \mathbf{E}_\perp + \partial_z E_z = 0$$

$$\nabla \cdot \mathbf{B} = 0 \rightsquigarrow \nabla \cdot \mathbf{H} = 0 \rightsquigarrow \nabla_\perp \cdot \mathbf{H}_\perp + \partial_z H_z = 0$$

$$\nabla \times \mathbf{E} = -\partial_t \mathbf{B} \rightsquigarrow \nabla \times \mathbf{E} = -j\omega\mu\mathbf{H} \rightsquigarrow \hat{z} \cdot (\nabla_\perp \times \mathbf{E}_\perp) = -j\omega\mu H_z$$

$$\rightsquigarrow \hat{z} \times (\partial_z \mathbf{E}_\perp - \nabla_\perp E_z) = -j\omega\mu \mathbf{H}_\perp$$

$$\nabla \times \mathbf{H} = \partial_t \mathbf{D} \rightsquigarrow \nabla \times \mathbf{H} = j\omega\epsilon\mathbf{E} \rightsquigarrow \hat{z} \cdot (\nabla_\perp \times \mathbf{H}_\perp) = j\omega\epsilon E_z$$

$$\rightsquigarrow \hat{z} \times (\partial_z \mathbf{H}_\perp - \nabla_\perp H_z) = j\omega\epsilon \mathbf{E}_\perp$$

Above equations are valid for all allowed electric and magnetic fields inside the waveguides. For the specific case of modes of the structure (i.e. eigenvectors of the waveguide system) one can further simplify the equations by the transformation $\partial_z \rightarrow -j\beta_k$ where β_k is the propagation constant of the mode in the \hat{z} direction. Since in the coupled mode formulations one would want to distinguish between the permittivity profile of the mode and the surrounding system, we will distinguish between them by explicitly stating that the mode is for a permittivity profile of $\epsilon_k(x, y)$.

$$\begin{aligned}\nabla_{\perp} \cdot \mathbf{E}_{k\perp} - j\beta_k E_{kz} &= 0 \\ \nabla_{\perp} \cdot \mathbf{H}_{k\perp} - j\beta_k H_{kz} &= 0 \\ \hat{z} \cdot (\nabla_{\perp} \times \mathbf{E}_{k\perp}) &= -j\omega\mu H_{kz} \\ -\hat{z} \times (j\beta_k \mathbf{E}_{k\perp} + \nabla_{\perp} E_{kz}) &= -j\omega\mu \mathbf{H}_{k\perp} \quad (\text{A.1})\end{aligned}$$

$$\begin{aligned}\hat{z} \cdot (\nabla_{\perp} \times \mathbf{H}_{k\perp}) &= j\omega\epsilon_k E_{kz} \\ -\hat{z} \times (j\beta_k \mathbf{H}_{k\perp} + \nabla_{\perp} H_{kz}) &= j\omega\epsilon_k \mathbf{E}_{k\perp} \quad (\text{A.2})\end{aligned}$$

In general, it is possible to divide the modes of a system into two categories, TE ($E_z = 0$) and TM ($H_z = 0$). By treating the longitudinal components (E_z, H_z) as source terms one can come up with expressions for the transverse components solely based on the longitudinal ones. With that in mind, we will further modify the above formulations by making use of the vector identity $\mathbf{A} \times (\mathbf{B} \times \mathbf{C}) = \mathbf{B}(\mathbf{A} \cdot \mathbf{C}) - \mathbf{C}(\mathbf{A} \cdot \mathbf{B})$. First take the cross product of both sides of (A.2) with \hat{z} to get

$$j\beta_k \mathbf{H}_{k\perp} + \nabla_{\perp} H_{kz} = j\omega\epsilon_k (\hat{z} \times \mathbf{E}_{k\perp}). \quad (\text{A.3})$$

Rearranging the terms in (A.1) results in

$$-j\omega\mu \mathbf{H}_{k\perp} - \hat{z} \times \nabla_{\perp} E_{kz} = j\beta_k (\hat{z} \times \mathbf{E}_{k\perp}). \quad (\text{A.4})$$

Multiplying both sides of (A.3) with $j\beta_k$ and substituting the expression for $j\beta_k (\hat{z} \times$

$\mathbf{E}_{k\perp}$) from (A.4) results in

$$\mathbf{H}_{k\perp} = \frac{-1}{\delta_k} (\mathbf{j} \beta_k \nabla_{\perp} H_{kz} + \mathbf{j} \omega \epsilon_k \hat{z} \times \nabla_{\perp} E_{kz}) \quad (\text{A.5})$$

where $\delta_k = \omega^2 \mu \epsilon_k - \beta_k^2$. Similarly taking the cross product of (A.1) with \hat{z} , multiplying the result with $\mathbf{j} \beta_k$ and substituting the definition of $\mathbf{j} \beta_k (\hat{z} \times \mathbf{H}_{k\perp})$ from (A.2) one gets

$$\mathbf{E}_{k\perp} = \frac{1}{\delta_k} (-\mathbf{j} \beta_k \nabla_{\perp} E_{kz} + \mathbf{j} \omega \mu \hat{z} \times \nabla_{\perp} H_{kz}).$$

As can be seen, we have now expressed transverse fields in terms of the longitudinal components.

Appendix B

Argument Principle Method

In this section we will briefly describe the method we used to find the zeros of (3.8) and (3.15). One of the main problems of any root finding algorithm is the starting point in the search domain. When the search needs to be done over two dimensions of the complex plane, brute force approaches have limited applicability. Luckily, there have been many advances in the root finding algorithms for waveguides [207–212].

If the function $f(z)$ ¹ is analytic, possesses no poles on and within the closed contour C and finally if $f(z)$ does not go to zero on C then:

$$\sum_{k=1}^N z_k^m = \frac{1}{2\pi i} \oint_C z^m \frac{f'(z)}{f(z)} dz \quad (\text{B.1})$$

where z_k denote the zeros of $f(z)$ in C , N is the total number of zeros in C and m is an arbitrary nonnegative integer. Specifically, for $m = 0$ one gets the total number of zeros within C . Knowing the number of zeros in a closed region enables one to dismiss regions of the complex search space in which there are no zeros. Furthermore, given the number of zeros in a region, one can do a subdivision until there is only one zero in the region of interest as described in [209]. For those regions with a single zero, another contour integral as in (B.1) with $m = 1$ will give the location of the zero. If better numerical accuracy is desired, one can do a local search given the approximate

¹The variable z in this appendix denotes an arbitrary complex number in the complex plane. It is *not* the space coordinate.

position obtained by the contour integration. This method of finding the zeros of a function by repeated integration on the complex plane is called the *argument principle method (APM)*.

Note that for the APM to work, the function $f(z)$ should be analytic in C . That requires no branch points to exist in the closed contour. Our implementation takes κ_m as the variable of interest. Equations (3.8) and (3.15) are rewritten in terms of only κ_m by using (3.9). Singularities of $\tanh(\kappa_i a)$ and of $\tanh(\kappa_m h)$ are removed by multiplying both sides of (3.8) by $\cosh(\kappa_i a)$ and of (3.15) by $\cosh(\kappa_i a) \cosh(\kappa_m h)$. At this stage the equations look like:

$$\epsilon_m \kappa_i \sinh(\kappa_i a) + \epsilon_i \kappa_m \cosh(\kappa_i a) = 0 \quad (\text{B.2})$$

$$\begin{aligned} \epsilon_m \kappa_i \sinh(\kappa_i a) \cosh(\kappa_m h) + \\ \epsilon_i \kappa_m \cosh(\kappa_i a) \sinh(\kappa_m h) = 0 \end{aligned} \quad (\text{B.3})$$

with $\kappa_i = \sqrt{\kappa_m^2 - k_0^2(\epsilon_m - \epsilon_i)}$ where $k_0 = 2\pi/\lambda$. The only branch points² are those caused by the square root function in the definition of κ_i . Note that the function $\sqrt{z} \sinh(\sqrt{z})$ is single valued everywhere on the complex plane, since regardless of the choice for the sign of the square root, the result does not change. Similarly $\cosh(\sqrt{z})$ is single valued due to the evenness of the hyperbolic cosine function. Therefore, (B.2) and (B.3) have no branch points and are analytic in the whole complex plane.

In our implementation, we also did the conformal mapping $\kappa_m = e^z$ to map the complex plane into strips. $z = \log(\kappa_m) \equiv \log|\kappa_m| + i \arg(\kappa_m) = \log|\kappa_m| + i \arg(\kappa_m) + i2\pi m$ for any integer m . The logarithm function is multi-valued, and repeats itself in strips that result from the $i2\pi m$ term. For instance, when we are interested in finding proper modes with $\text{Re}(\kappa_m) > 0$ we only need to search the strip $-\pi/2 < \text{Im}(z) < \pi/2$.

Lastly, using computer algebra systems that can do symbolic mathematical manipulations, one can easily calculate $f'(z)$ from the definition of $f(z)$ given by (B.2) or (B.3) in addition to doing numerical integrations on the complex plane.

²The concept of Riemann surface is another way to look at the branch points of complex functions. For instance, the square root function has a two-sheeted Riemann surface due to the two possible ways of choosing the sign of the result. [212] visualizes and talks about Riemann surfaces.

Appendix C

Some Details of the Mode Matching Algorithm

Once the full set of modes are found using `APM`, implementation of the mode-matching algorithm reduces to the calculation of the overlap integrals to build the matrix equation that should be solved to get the reflection and transmission coefficients, R_{kp} and T_{kp} , of (3.18)-(3.19). Since we have the analytical solutions for the fields as given in (3.7) and (3.16), overlap integrals $\Omega_{\{L,R\}}^{(m)}$ and $[e_{\{L,R\}}^{(m)} | h_{\{R,L\}}^{(k)}]$ can be calculated analytically in closed form. The expressions are too long to reproduce here, but a computer algebra system can do the analytical manipulations. Once we have closed form results for the overlap integrals, formation of the matrix equation is very quick. The matrices have relatively small sizes and the solution of the linear matrix equation proceeds quickly. Also note that we numerically check the validity of the mode orthogonality condition of (3.13) before we start the mode-matching calculations so as to check the correctness of the `APM` implementation. We used Mathematica to implement `APM` and the mode-matching method. The source code is available on the Internet under the GNU general public license.

Appendix D

Fabrication Recipe

1. SOI silicon layer thinning

- Clean wafers at WBNonmetal by Piranha
- Clean wafers at WBDiff by a pre-diffusion clean
- First do wet and then dry oxidation at Thermco
- Measure oxide thickness by Woollam
- Do oxide etch using HF
- Repeat until desired Si thickness is reached

2. Cleave chips into pieces with roughly 1-1.5 cm sided squares

3. Clean for Layer 1 at WBNonmetal

- 9:1 H₂SO₄:H₂O₂ at 90 °C for 20 minutes
- Rinse
- 50:1 HF for 30 sec
- Rinse & Dry
- YES Oven bake

4. Coating for Layer 1 at Headway

- Coat Ma-D 2403 at 5000 rpm
- 90 °C, 2 min bake

5. EBL for Layer 1 at Raith

- Before EBL do 90 °C, 2 min bake
- Before login, set settings to default values
- Make sure Area Step Size and Line Step Size are as small as possible while having a write speed less than 10 mm/sec
- In “Exposure Details” section, have exposure raster to be free metric raster and click on the calculator button
- Also make sure that Area Mode is set to line
- Dosages are less than 80 for areas, around 230 for lines
- Save the protocol file after each session for logging purposes

6. Develop for Layer 1 at the e-beam wet bench

- Ma-D 532 for 40 sec
- DI Water for 5 min
- Blow Dry

7. Etching for Layer 1 at AMT. Modify the “Si Trench Etch” by copying program 1 into program 5 such that

- Pressure is 20 mT
- NF₃ flow is 20 sccm
- Bias Setting is -430 Volts
- Set the etch to a long time (~15 min) and visually confirm the bull's eye closing pattern. Then wait for 10-20 secs more and stop the etch.
- After the etch, check the silicon thickness with Woollam.

8. Clean for Layer 2 at WBNonMetal

- 9:1 H₂SO₄:H₂O₂ at 90 °C for 20 minutes
- Rinse
- 50:1 HF for 30 sec
- Rinse & Dry
- 30 min Singe oven bake at 150°

9. Coating for Layer 2 at Headway

- 2% PMMA 950K at 1600 rpm
- 2 min, 200 °C bake

10. EBL for Layer 2 @ Raith

- Before EBL do 90 °C 2 min bake
- Before login, set settings to default values
- Make sure Area Step Size and Line Step Size are as small as possible while having a write speed less than 10 mm/sec
- In Exposure Details section, have exposure raster to be free metric raster and click on the calculator button
- Make sure that Area Mode is set to line
- Save the protocol file after each session for logging purposes

11. Develop for Layer 1 at the e-beam wet bench

- 1:3 (MIBK:IPA) 30 sec
- IPA 30sec
- Blow dry
- Bake the sample at 90 °C for two minutes after develop for degassing to enhance metal deposition on the surface.

12. Metalization for Layer 2 at Innotec or by Tom Carver

- Do 5-6 secs of 20:1 BOE dip before evaporation, that etches the native oxide on the silicon lines
- Deposit 5 nm Ti + 30 nm Au

13. Lift-off for Layer 2 at WBSolvent

- Remover PG 40-50 °C 10 min
- Acetone flush
- Remover PG 40 °C + Ultrasonic 10 min
- Acetone Room Temp + Ultrasonic 5 min
- IPA Room Temp + Ultrasonic 5 min
- Blow Dry

Bibliography

- [1] K. Hyland, "Graduates' gratitude: the generic structure of dissertation acknowledgements," *English for Specific Purposes*, vol. 23, no. 3, pp. 303 – 324, 2004.
- [2] Wikipedia, "History of optics — wikipedia, the free encyclopedia," 2009, [Online; accessed 13-July-2009]. http://en.wikipedia.org/w/index.php?title=History_of_optics&oldid=301776825
- [3] BBC Radio 4, "In our time: History of optics," March 2007, [Online; accessed 9-September-2009]. http://www.bbc.co.uk/radio4/history/inourtime/inourtime_20070301.shtml
- [4] M. W. Davidson, "Sir David Brewster," *Lab Medicine*, vol. 40, no. 9, pp. 563–564, 2009.
- [5] D. Ihde, "Epistemology engines," *Nature*, vol. 406, no. 6791, pp. 21–21, Jul 2000.
- [6] J. Raskin, "The Iron Heel at 100 - Jack London - the artist as 'antenna of the race'," *Monthly Review*, vol. 59, no. 10, pp. 1–7, Mar 2008.
- [7] J. Light, "When computers were women," *Technology and Culture*, vol. 40, no. 3, pp. 455–483, Jul 1999.
- [8] D. A. B. Miller, "Rationale and challenges for optical interconnects to electronic chips," *Proceedings of the IEEE*, vol. 88, no. 6, pp. 728–749, Jun 2000.
- [9] D. A. B. Miller, "Device requirements for optical interconnects to silicon chips," *Proceedings of the IEEE*, vol. 97, no. 7, pp. 1166–1185, July 2009.
- [10] E. Özbay, "Plasmonics: merging photonics and electronics at nanoscale dimensions," *Science*, vol. 311, pp. 189–193, 2006.
- [11] Şükrü Ekin Kocabas, G. Veronis, D. A. B. Miller, and S. Fan, "Modal analysis and coupling in metal-insulator-metal waveguides," *Physical Review B*, vol. 79, no. 3, p. 035120, 2009.
- [12] Ş. E. Kocabas, G. Veronis, D. A. B. Miller, and S. Fan, "Transmission line and equivalent circuit models for plasmonic waveguide components," *Selected Topics in Quantum Electronics, IEEE Journal of*, vol. 14, no. 6, pp. 1462–1472, Nov.-Dec. 2008.
- [13] W. S. Fann, R. Storz, H. W. K. Tom, and J. Bokor, "Electron thermalization in gold," *Physical Review B*, vol. 46, no. 20, p. 13592, Nov 1992.

- [14] C. F. Bohren and D. R. Huffman, *Absorption and Scattering of Light by Small Particles*. Wiley Science, 1983.
- [15] L. D. Landau, E. M. Lifshitz, and L. P. Pitaevskii, *Electrodynamics of Continuous Media*. Pergamon Press, 1984.
- [16] E. D. Palik, Ed., *Handbook of Optical Constants of Solids*. Academic, New York, 1985.
- [17] E. N. Economou, "Surface plasmons in thin films," *Physical Review*, vol. 182, no. 2, pp. 539 – 54, 1969.
- [18] N. W. Ashcroft and N. D. Mermin, *Solid State Physics*. Thomson Learning, 1976.
- [19] D. Marcuse, *Theory of Dielectric Optical Waveguides*, 2nd ed. San Diego, CA: Academic Press, 1991.
- [20] C. Davis and T. Tamir, "Bound waves in compressible plasma gaps," *International Journal of Electronics*, vol. 19, no. 4, pp. 323 – 342, UK 1966.
- [21] C. Davis and T. Tamir, "Surface and interface waves in plasma gaps," *Journal of Applied Physics*, vol. 37, no. 1, pp. 461 – 462, 1966.
- [22] T. Takano and J. Hamasaki, "Propagating modes of a metal-clad-dielectric-slab waveguide for integrated optics," *IEEE Journal of Quantum Electronics*, vol. 8, no. 2, pp. 206–212, 1972.
- [23] I. P. Kaminow, W. L. Mammel, and H. P. Weber, "Metal-clad optical waveguides: analytical and experimental study," *Applied Optics*, vol. 13, no. 2, pp. 396 – 405, Feb 1974.
- [24] B. Prade, J. Y. Vinet, and A. Mysyrowicz, "Guided optical waves in planar heterostructures with negative dielectric constant," *Physical Review B*, vol. 44, no. 24, pp. 13 556 – 72, Dec 1991.
- [25] F. Villa, T. Lopez-Rios, and L. E. Regalado, "Electromagnetic modes in metal-insulator-metal structures," *Phys. Rev. B*, vol. 63, no. 16, p. 165103, Apr 2001.
- [26] D.-K. Qing and G. Chen, "Nanoscale optical waveguides with negative dielectric claddings," *Physical Review B*, vol. 71, no. 15, p. 153107, 2005.
- [27] J. A. Dionne, L. A. Sweatlock, H. A. Atwater, and A. Polman, "Plasmon slot waveguides: Towards chip-scale propagation with subwavelength-scale localization," *Physical Review B*, vol. 73, no. 3, p. 035407, Jan 2006.
- [28] P. Ginzburg, D. Arbel, and M. Orenstein, "Gap plasmon polariton structure for very efficient microscale-to-nanoscale interfacing," *Optics Letters*, vol. 31, no. 22, pp. 3288 – 3290, Nov 2006.
- [29] K. Y. Kim, Y. K. Cho, H.-S. Tae, and J.-H. Lee, "Light transmission along dispersive plasmonic gap and its subwavelength guidance characteristics," *Opt. Express*, vol. 14, no. 1, pp. 320–330, 2006.
- [30] R. Gordon, "Light in a subwavelength slit in a metal: propagation and reflection." *Physical Review B*, vol. 73, no. 15, p. 153405, 2006.

- [31] E. Feigenbaum and M. Orenstein, "Modeling of complementary (void) plasmon waveguiding," *Journal of Lightwave Technology*, vol. 25, no. 9, pp. 2547 – 2562, September 2007.
- [32] Y. Kurokawa and H. T. Miyazaki, "Metal-insulator-metal plasmon nanocavities: Analysis of optical properties," *Physical Review B*, vol. 75, no. 3, p. 035411, Jan 2007.
- [33] X. Wang and K. Kempa, "Plasmon polaritons in slot waveguides: Simple model calculations and a full nonlocal quantum mechanical treatment," *Physical Review B*, vol. 75, no. 24, p. 245426, 2007.
- [34] Z. J. Sun and D. Y. Zeng, "Coupling of surface plasmon waves in metal/dielectric gap waveguides and single interface waveguides," *Journal of the Optical Society of America B: Optical Physics*, vol. 24, no. 11, pp. 2883 – 2887, November 2007.
- [35] A. R. Zakharian, J. V. Moloney, and M. Mansuripur, "Surface plasmon polaritons on metallic surfaces," *Optics Express*, vol. 15, no. 1, pp. 183 – 197, 2007.
- [36] B. Sturman, E. Podivilov, and M. Gorkunov, "Eigenmodes for metal-dielectric light-transmitting nanostructures," *Physical Review B*, vol. 76, no. 12, p. 125104, 2007.
- [37] T. Tamir and A. A. Oliner, "The spectrum of electromagnetic waves guided by a plasma layer," *Proceedings of the IEEE*, vol. 51, no. 2, pp. 317 – 332, 1963.
- [38] C. R. Paiva and A. M. Barbosa, "Spectral representation of self-adjoint problems for layered anisotropic waveguides," *IEEE Transactions on Microwave Theory and Techniques*, vol. 39, no. 2, pp. 330–338, Feb 1991.
- [39] T. F. Jabolnski, "Complex modes in open lossless dielectric waveguides," *Journal of the Optical Society of America A (Optics and Image Science)*, vol. 11, no. 4, pp. 1272 –1282, Apr 1994.
- [40] W. Shu and J. M. Song, "Complete mode spectrum of a grounded dielectric slab with double negative metamaterials," *Progress in Electromagnetics Research*, vol. 65, pp. 103 – 123, 2006.
- [41] K. Y. Kim, Y. K. Cho, H.-S. Tae, and J.-H. Lee, "Guided mode propagations of grounded double-positive and double-negative metamaterial slabs with arbitrary material indexes," *Journal of the Korean Physical Society*, vol. 49, no. 2, pp. 577 – 584, 2006.
- [42] B. Friedman, *Principles and Techniques of Applied Mathematics*. New York: Dover Publications, 1990, reprint of 1956 ed.
- [43] W. C. Chew, *Waves and Fields in Inhomogenous Media*. New York: Van Nostrand Reinhold, 1990.
- [44] E. Kreyszig, *Introductory Functional Analysis with Applications*. John Wiley & Sons, 1978.
- [45] G. W. Hanson and A. B. Yakovlev, *Operator Theory for Electromagnetics*. New York: Springer-Verlag, 2002.
- [46] J. Locker, *Spectral Theory of Non-Self-Adjoint Two-Point Differential Operators*. American Mathematical Society, 2000.

- [47] R. V. Churchill, *Fourier Series and Boundary Value Problems*. New York: McGraw-Hill Book Company, 1941.
- [48] A. Zettl, *Sturm-Liouville Theory*. American Mathematical Society, 2005.
- [49] R. Richardson, “Contributions to the study of oscillation properties of the solutions of linear differential equations of the second order,” *American Journal of Mathematics*, vol. 40, no. 3, pp. 283–316, 1918.
- [50] A. Mostafazadeh, “Pseudo-hermiticity versus PT-symmetry III: Equivalence of pseudo-hermiticity and the presence of antilinear symmetries,” *Journal of Mathematical Physics*, vol. 43, no. 8, pp. 3944 – 3951, Aug 2002.
- [51] A. Mostafazadeh and F. Loran, “Propagation of electromagnetic waves in linear media and pseudo-hermiticity,” *EPL*, vol. 81, no. 1, p. 10007, 2008.
- [52] M. Mrozowski, *Guided Electromagnetic Waves*. UK: Research Studies Press, 1997.
- [53] E. B. Davies, “Non-self-adjoint differential operators,” *Bulletin of the London Mathematical Society*, vol. 34, pp. 513 – 532, Sep 2002.
- [54] V. V. Shevchenko, *Continuous Transitions in Open Waveguides*. Boulder, Colorado: Golem Press, 1971.
- [55] T. Rozzi and M. Mongiardo, *Open Electromagnetic Waveguides*. The Institution of Electrical Engineers, 1997.
- [56] D. A. B. Miller, *Quantum Mechanics for Scientists and Engineers*. Cambridge University Press, 2008.
- [57] R. E. Collin, *Field Theory of Guided Waves*, 2nd ed. Wiley-Interscience, 1991.
- [58] A. Kostenbauder, Y. Sun, and A. Siegman, “Eigenmode expansions using biorthogonal functions: complex-valued HermiteGaussians,” *Journal of the Optical Society of America A*, vol. 14, no. 8, pp. 1780–1790, 1997.
- [59] C. R. MacCluer and Y. Chait, “Choosing an inner product that separates variables,” *SIAM Review*, vol. 33, no. 3, pp. 467–471, 1991.
- [60] V. V. Shevchenko, “Forward and backward waves: three definitions and their interrelation and applicability,” *Physics-Uspekhi*, vol. 50, no. 3, pp. 287 – 292, March 2007.
- [61] H. J. Hagemann, W. Gudat, and C. Kunz, “Optical constants from the far infrared to the X-ray region: Mg, Al, Cu, Ag, Au, Bi, C, and Al₂O₃.” *Journal of the Optical Society of America*, vol. 65, pp. 742–744, 1975.
- [62] P. J. B. Clarricoats and K. R. Slinn, “Numerical solution of waveguide-discontinuity problems,” *Proceedings of the Institution of Electrical Engineers*, vol. 114, pp. 878–887, 1967.
- [63] P. Bienstman, “Rigorous and efficient modelling of wavelength scale photonic components,” Ph.D. dissertation, Ghent University, 2001.
- [64] I. Breukelaar and P. Berini, “Long-range surface plasmon polariton mode cutoff and radiation in slab waveguides,” *Journal of the Optical Society of America A-Optics Image Science And Vision*, vol. 23, no. 8, pp. 1971–1977, Aug. 2006.

- [65] I. Breukelaar, R. Charbonneau, and P. Berini, "Long-range surface plasmon-polariton mode cutoff and radiation in embedded strip waveguides," *Journal of Applied Physics*, vol. 100, p. 043104, 2006.
- [66] R. F. Oulton, D. F. P. Pile, Y. Liu, and X. Zhang, "Scattering of surface plasmon polaritons at abrupt surface interfaces: Implications for nanoscale cavities," *Physical Review B*, vol. 76, no. 3, p. 035408, 2007.
- [67] R. Bousso and J. Polchinski, "Quantization of four-form fluxes and dynamical neutralization of the cosmological constant," *Journal of High Energy Physics*, vol. 2000, p. 006, 2000.
- [68] L. P. Felsen and N. Marcuvitz, *Radiation and Scattering of Waves*. IEEE Press, 1994.
- [69] K. A. Zaki, C. Seng-Woon, and C. Chunming, "Modeling discontinuities in dielectric-loaded waveguides," *IEEE Transactions on Microwave Theory and Techniques*, vol. 36, no. 12, pp. 1804 – 1810, Dec 1988.
- [70] A. S. Omar and K. Schunemann, "Complex and backward-wave modes in inhomogeneously and anisotropically filled waveguides," *IEEE Transactions on Microwave Theory and Techniques*, vol. 35, pp. 268–275, 1987.
- [71] A. S. Omar and K. Schunemann, "Formulation of the singular integral-equation technique for planar transmission-lines," *IEEE Transactions on Microwave Theory and Techniques*, vol. 33, no. 12, pp. 1313 – 1322, Dec 1985.
- [72] A. S. Omar and K. F. Schunemann, "The effect of complex modes at finline discontinuities," *IEEE Transactions on Microwave Theory and Techniques*, vol. 34, no. 12, pp. 1508 – 1514, 1986.
- [73] B. Sturman, E. Podivilov, and M. Gorkunov, "Eigenmodes for the problem of extraordinary light transmission through subwavelength holes," *EPL*, vol. 79, no. 2, p. 24002, 2007.
- [74] B. Sturman, E. Podivilov, and M. Gorkunov, "Theory of extraordinary light transmission through arrays of subwavelength slits," *Physical Review B*, vol. 77, no. 7, p. 075106, 2008.
- [75] G. V. Eleftheriades, A. S. Omar, L. P. B. Katehi, and G. M. Rebeiz, "Some important properties of waveguide junction generalized scattering matrices in the context of the mode matching technique," *IEEE Transactions on Microwave Theory and Techniques*, vol. 42, no. 10, pp. 1896 – 1903, Oct 1994.
- [76] G. Veronis and S. H. Fan, "Bends and splitters in metal-dielectric-metal subwavelength plasmonic waveguides," *Applied Physics Letters*, vol. 87, p. 131102, 2005.
- [77] A. K. Bhattacharyya, "On the convergence of MoM and mode matching solutions for infinite array and waveguide problems," *IEEE Transactions on Antennas and Propagation*, vol. 51, no. 7, pp. 1599 – 1606, July 2003.
- [78] S. W. Lee, W. R. Jones, and J. J. Campbell, "Convergence of numerical solutions of iris-type discontinuity problems," *IEEE Transactions on Microwave Theory and Techniques*, vol. 19, no. 6, pp. 528 – 536, 1971.

- [79] M. Leroy, "On the convergence of numerical results in modal analysis," *IEEE Transactions on Antennas and Propagation*, vol. 31, no. 4, pp. 655–659, Jul 1983.
- [80] R. Mittra, T. Itoh, and T.-S. Li, "Analytical and numerical studies of the relative convergence phenomenon arising in the solution of an integral equation by the moment method," *IEEE Transactions on Microwave Theory and Techniques*, vol. 20, no. 2, pp. 96 – 104, Feb 1972.
- [81] E. Prodan, C. Radloff, N. J. Halas, and P. Nordlander, "A Hybridization Model for the Plasmon Response of Complex Nanostructures," *Science*, vol. 302, pp. 419–422, 2003.
- [82] I. Kay and H. Moses, "Reflectionless Transmission through Dielectrics and Scattering Potentials," *Journal of Applied Physics*, vol. 27, p. 1503, 1956.
- [83] J. Lekner, *Theory of Reflection*. Hingham, MA: Kluwer Academic Publishers, 1987.
- [84] C. Siewert, "Explicit results for the quantum-mechanical energy states basic to a finite square-well potential," *Journal of Mathematical Physics*, vol. 19, p. 434, 1978.
- [85] P. Paul and D. Nkemzi, "On the energy levels of a finite square-well potential," *Journal of Mathematical Physics*, vol. 41, p. 4551, 2000.
- [86] R. Blümel, "Analytical solution of the finite quantum square-well problem," *J. Phys. A: Math. Gen.*, vol. 38, no. 42, pp. L673–L678, 2005.
- [87] Z. Ahmed, "Reflection from an interface," *Journal of Physics A: Mathematical and General*, vol. 33, no. 16, pp. 3161–3172, 2000.
- [88] C. M. Bender, "Making sense of non-hermitian hamiltonians," *Reports on Progress in Physics*, vol. 70, no. 6, pp. 947–1018, 2007.
- [89] F. S. H.B. Geyer, W.D. Heiss, "Non-hermitian hamiltonians, metric, other observables and physical implications," 2008, arXiv:0710.5593v1 [quant-ph].
- [90] M. T. David Krejcirik, "Non-hermitian spectral effects in a \mathcal{PT} -symmetric waveguide," *Journal of Physics A: Mathematical and Theoretical*, vol. 41, no. 24, p. 244013, 2008.
- [91] S. Albeverio, U. Guenther, and S. Kuzhel, "j-self-adjoint operators with \mathcal{C} -symmetries: extension theory approach," arXiv:0811.0365 [math-ph].
- [92] S. Kuzhel, "On pseudo-hermitian operators with generalized \mathcal{C} -symmetries," arXiv:0802.4269 [math-ph].
- [93] D. Williams, B. Alpert, U. Arz, D. Walker, and H. Grabinski, "Causal characteristic impedance of planar transmission lines," *Advanced Packaging, IEEE Transactions on*, vol. 26, no. 2, pp. 165–171, 2003.
- [94] M. Haakestad and J. Skaar, "Causality and Kramers-Kronig relations for waveguides," *Optics Express*, vol. 13, no. 24, pp. 9922–9934, 2005.
- [95] F. Lopez-Tejeira, S. G. Rodrigo, L. Martin-Moreno, F. J. Garcia-Vidal, E. Devaux, T. W. Ebbesen, J. R. Krenn, I. P. Radko, S. I. Bozhevolnyi, M. U. Gonzalez, J. C. Weeber, and A. Dereux, "Efficient unidirectional nanoslit couplers for surface plasmons," *Nature Physics*, vol. 3, no. 5, pp. 324 – 328, May 2007.

- [96] E. Verhagen, J. A. Dionne, L. K. Kuipers, H. A. Atwater, and A. Polman, "Near-field visualization of strongly confined surface plasmon polaritons in metal–insulator–metal waveguides," *Nano Letters*, vol. 8, no. 9, pp. 2925–2929, 2008.
- [97] J. A. Dionne, E. Verhagen, A. Polman, and H. A. Atwater, "Are negative index materials achievable with surface plasmon waveguides? A case study of three plasmonic geometries," *Opt. Express*, vol. 16, no. 23, pp. 19 001–19 017, 2008.
- [98] V. V. Klimov and M. Ducloy, "Spontaneous emission rate of an excited atom placed near a nanofiber," *Phys. Rev. A*, vol. 69, no. 1, p. 013812, Jan 2004.
- [99] D. E. Chang, A. S. S. rensen, P. R. Hemmer, and M. D. Lukin, "Quantum optics with surface plasmons," *Physical Review Letters*, vol. 97, no. 5, p. 053002, 2006.
- [100] D. Chang, A. Sørensen, E. Demler, and M. Lukin, "A single-photon transistor using nanoscale surface plasmons," *Nature Physics*, vol. 3, pp. 807–812, 2007.
- [101] Y. C. Jun, R. D. Kekatpure, J. S. White, and M. L. Brongersma, "Nonresonant enhancement of spontaneous emission in metal-dielectric-metal plasmon waveguide structures," *Physical Review B*, vol. 78, no. 15, p. 153111, 2008.
- [102] F. Intravaia and A. Lambrecht, "Surface plasmon modes and the casimir energy," *Physical Review Letters*, vol. 94, no. 11, p. 110404, 2005.
- [103] F. Capasso, J. Munday, D. Iannuzzi, and H. Chan, "Casimir forces and quantum electro-dynamical torques: Physics and nanomechanics," *Selected Topics in Quantum Electronics, IEEE Journal of*, vol. 13, no. 2, pp. 400–414, March-April 2007.
- [104] S. Collin, F. Pardo, and J. L. Pelouard, "Waveguiding in nanoscale metallic apertures," *Optics Express*, vol. 15, no. 7, pp. 4310 – 4320, Apr 2007.
- [105] F. M. Kong, K. Li, B. I. Wu, H. Huang, H. S. Chen, and J. A. Kong, "Propagation properties of the spp modes in nanoscale narrow metallic gap, channel, and hole geometries," *Progress in Electromagnetics Research*, vol. 76, pp. 449 – 466, 2007.
- [106] F. M. Kong, B. I. Wu, H. S. Chen, and J. A. Kong, "Surface plasmon mode analysis of nanoscale metallic rectangular waveguide," *Optics Express*, vol. 15, no. 19, pp. 12 331 – 12 337, Sep 2007.
- [107] M. W. Vogel and D. K. Gramotnev, "Adiabatic nano-focusing of plasmons by metallic tapered rods in the presence of dissipation," *Physics Letters A*, vol. 363, no. 5-6, pp. 507 – 511, Apr 2007.
- [108] A. A. Oliner, "Historical perspectives on microwave field theory," *IEEE Transactions on Microwave Theory and Techniques*, vol. 32, no. 9, pp. 1022 – 1045, Sep 1984.
- [109] S. A. Schelkunoff, "Forty years ago: Maxwell's theory invades engineering-and grows with it," *IEEE Transactions on Antennas and Propagation*, vol. 18, no. 3, pp. 309–322, 1970.
- [110] P. J. Schuck, D. P. Fromm, A. Sundaramurthy, G. S. Kino, and W. E. Moerner, "Improving the mismatch between light and nanoscale objects with gold bowtie nanoantennas," *Phys. Rev. Lett.*, vol. 94, no. 1, p. 017402, Jan 2005.

- [111] A. Alu and N. Engheta, "Optical nanotransmission lines: synthesis of planar left-handed metamaterials in the infrared and visible regimes," *Journal of the Optical Society of America B (Optical Physics)*, vol. 23, no. 3, pp. 571 – 583, March 2006.
- [112] N. Engheta, "Circuits with Light at Nanoscales: Optical Nanocircuits Inspired by Metamaterials," *Science*, vol. 317, no. 5845, pp. 1698–1702, 2007.
- [113] A. I. Csurgay and W. Porod, "Surface plasmon waves in nanoelectronic circuits," *International Journal of Circuit Theory and Applications*, vol. 32, no. 5, pp. 339–361, September–October 2004.
- [114] A. Hosseini, H. Nejati, and Y. Massoud, "Design of a maximally flat optical low pass filter using plasmonic nanostrip waveguides," *Opt. Express*, vol. 15, no. 23, pp. 15 280–15 286, 2007.
- [115] A. Hosseini, H. Nejati, and Y. Massoud, "Modeling and design methodology for metal-insulator-metal plasmonic bragg reflectors," *Optics Express*, vol. 16, no. 3, pp. 1475 – 1480, Feb 2008.
- [116] E. Feigenbaum and M. Orenstein, "Perfect 4-way splitting in nano plasmonic X-junctions," *Optics Express*, vol. 15, no. 26, pp. 17 948 – 17 953, Dec 2007.
- [117] Z. Han and S. He, "Multimode interference effect in plasmonic subwavelength waveguides and an ultra-compact power splitter," *Optics Communications*, vol. 278, no. 1, pp. 199–203, Oct. 2007.
- [118] K. Tanaka and M. Tanaka, "Simulations of nanometric optical circuits based on surface plasmon polariton gap waveguide," *Applied Physics Letters*, vol. 82, no. 8, pp. 1158–1160, Feb. 2003.
- [119] G. Veronis and S. H. Fan, "Theoretical investigation of compact couplers between dielectric slab waveguides and two-dimensional metal-dielectric-metal plasmonic waveguides," *Optics Express*, vol. 15, no. 3, pp. 1211 – 1221, Feb 2007.
- [120] J. R. Whinnery and H. W. Jamieson, "Equivalent circuits for discontinuities in transmission lines," *Institute of Radio Engineers – Proceedings*, vol. 32, no. 2, pp. 98 – 114, Feb 1944.
- [121] H. A. Jamid and S. J. AlBader, "Reflection and transmission of surface plasmon mode at a step discontinuity," *IEEE Photonics Technology Letters*, vol. 9, no. 2, pp. 220 – 222, Feb 1997.
- [122] P. Ginzburg and M. Orenstein, "Plasmonic transmission lines: From micro to nano scale with $\lambda/4$ impedance matching," *Optics Express*, vol. 15, no. 11, pp. 6762 – 6767, May 2007.
- [123] J. C. Weeber, Y. Lacroix, A. Dereux, E. Devaux, T. Ebbesen, C. Girard, M. U. Gonzalez, and A. L. Baudrion, "Near-field characterization of bragg mirrors engraved in surface plasmon waveguides," *Physical Review B*, vol. 70, no. 23, p. 235406, 2004.
- [124] C. Girard, "Near fields in nanostructures," *Reports on Progress in Physics*, vol. 68, no. 8, pp. 1883 – 1933, Aug 2005.

- [125] D. M. Pozar, *Microwave Engineering*. Addison-Wesley, 1990, ch. Microwave Network Analysis, pp. 220–234.
- [126] S. Ramo, J. R. Whinnery, and T. V. Duzer, *Fields and Waves in Communication Electronics*, 3rd ed. John Wiley & Sons, 1994.
- [127] C. Montgomery, R. Dicke, and E. Purcell, *Principles of Microwave Circuits*. Peter Peregrinus Ltd., London, UK, 1987, reprint of the first publication in 1948 by the McGraw-Hill Book Company Inc.
- [128] P. A. Rizzi, *Microwave Engineering, Passive Circuits*. Prentice Hall, 1988.
- [129] R. E. Collin, *Field Theory of Guided Waves*, 2nd ed. Wiley-Interscience-IEEE, 1991, ch. 8, pp. 581–588.
- [130] R. E. Collin, *Foundations for Microwave Engineering*. McGraw-Hill Book Company, 1966.
- [131] P. H. Smith, *Electronic Applications of the Smith Chart in Waveguide, Circuit and Component Analysis*. Robert E. Krieger Publishing Company, 1983.
- [132] E. L. Ginzton, *Microwave Measurements*. McGraw-Hill Book Company Inc., 1957, ch. Representation and Measurement of Microwave Circuits, pp. 313–345.
- [133] N. Marcuvitz, Ed., *Waveguide Handbook*, ser. Radiation Laboratory series. McGraw-Hill, 1951, vol. 10.
- [134] J. Schwinger and D. S. Saxon, *Discontinuities in Waveguides*. Gordon and Breach Science Publishers Inc., 1968, ch. 5, pp. 99–124.
- [135] L. Lewin, *Advanced Theory of Waveguides*. Iliffe & Sons Ltd., 1951, ch. 5, pp. 98–106.
- [136] T. V. Teperik, V. V. Popov, and F. J. G. de Abajo, “Total light absorption in plasmonic nanostructures,” *Journal Of Optics A-Pure And Applied Optics*, vol. 9, no. 9, pp. S458–S462, Sep. 2007.
- [137] S. J. Garner, D. V. Thiel, and S. G. OKeefe, “Surface impedance time domain reflectometry for the determination of ice depth,” *Geophysical Research Letters*, vol. 24, no. 13, pp. 1599 – 1602, Jul 1997.
- [138] SPICE. Wikipedia, The Free Encyclopedia. <http://en.wikipedia.org/wiki/SPICE>
- [139] *HSPICE® Signal Integrity User Guide*, Z-2007.03 ed., Synopsys, March 2007, ch. S-parameter Modeling Using the S-element.
- [140] G. Veronis and S. H. Fan, “Modes of subwavelength plasmonic slot waveguides,” *Journal of Lightwave Technology*, vol. 25, no. 9, pp. 2511 – 21, September 2007.
- [141] S. Silver, Ed., *Microwave antenna theory and design*, ser. Radiation Laboratory series. McGraw-Hill, 1949, vol. 12.
- [142] W. L. Stutzman and G. A. Thiele, *Antenna theory and design*, 2nd ed. Wiley, 1998.
- [143] R. E. Collin, *Antennas and Radiowave Propagation*. McGraw-Hill Book Company, 1985.
- [144] D.-S. Ly-Gagnon, S. E. Kocabas, and D. A. B. Miller, “Characteristic impedance model for plasmonic metal slot waveguides,” *Selected Topics in Quantum Electronics, IEEE Journal of*, vol. 14, no. 6, pp. 1473–1478, Nov.-Dec. 2008.

- [145] P. Lilienfeld, "Gustav Mie: the person," *Appl. Opt.*, vol. 30, no. 33, pp. 4696–4698, 1991.
- [146] D. J. Segelstein, "The complex refractive index of water," Master's thesis, University of Missouri, Kansas City, 1981.
- [147] J. D. Jackson, *Classical electrodynamics*, 3rd ed. Wiley, 1999.
- [148] D.-S. Wang, "Limits and validity of the impedance boundary condition on penetrable surfaces," *Antennas and Propagation, IEEE Transactions on*, vol. 35, no. 4, pp. 453–457, Apr 1987.
- [149] S. Rao, D. Wilton, and A. Glisson, "Electromagnetic scattering by surfaces of arbitrary shape," *Antennas and Propagation, IEEE Transactions on*, vol. 30, no. 3, pp. 409–418, May 1982.
- [150] B. Jung, T. Sarkar, and Y. Chung, "A survey of various frequency domain integral equations for the analysis of scattering from three-dimensional dielectric objects," *Journal of Electromagnetic Waves and Applications*, vol. 16, no. 10, pp. 1419–1421, 2002.
- [151] A. Taflove and S. C. Hagness, *Computational Electrodynamics: The Finite-Difference Time-Domain Method*, 3rd ed. Artech House, 2005.
- [152] K. Yee, "Numerical solution of initial boundary value problems involving Maxwell's equations in isotropic media," *Antennas and Propagation, IEEE Transactions on*, vol. 14, no. 3, pp. 302–307, May 1966.
- [153] C. A. Balanis, *Advanced engineering electromagnetics*. Wiley, 1989.
- [154] M. Watts and R. Diaz, "Perfect plane-wave injection into a finite FDTD domain through teleportation of fields," *Electromagnetics*, vol. 23, no. 2, pp. 187–201, 2003.
- [155] Q. Wei, F. Liu, L. Xia, and S. Crozier, "An object-oriented designed finite-difference time-domain simulator for electromagnetic analysis and design in MRI-applications to high field analyses," *Journal of Magnetic Resonance*, vol. 172, no. 2, pp. 222–230, 2005.
- [156] M. Paulus, P. Gay-Balmaz, and O. J. F. Martin, "Accurate and efficient computation of the green's tensor for stratified media," *Phys. Rev. E*, vol. 62, no. 4, pp. 5797–5807, Oct 2000.
- [157] M. Paulus and O. J. F. Martin, "Light propagation and scattering in stratified media: a green's tensor approach," *J. Opt. Soc. Am. A*, vol. 18, no. 4, pp. 854–861, 2001.
- [158] H. Fischer and O. Martin, "Engineering the optical response of plasmonic nanoantennas," *Optics Express*, vol. 16, no. 12, pp. 9144–9154, 2008.
- [159] S. Frickel and N. Gross, "A general theory of scientific/intellectual movements," *American Sociological Review*, vol. 70, no. 2, pp. 204–232, Apr 2005.
- [160] D. Jackson and N. Alexopoulos, "Analysis of planar strip geometries in a substrate-superstrate configuration," *Antennas and Propagation, IEEE Transactions on*, vol. 34, no. 12, pp. 1430–1438, Dec 1986.
- [161] M. Kominami, D. Pozar, and D. Schaubert, "Dipole and slot elements and arrays on semi-infinite substrates," *Antennas and Propagation, IEEE Transactions on*, vol. 33, no. 6, pp. 600–607, Jun 1985.

- [162] K. Ueno, S. Juodkazis, M. Mino, V. Mizeikis, and H. Misawa, "Spectral sensitivity of uniform arrays of gold nanorods to dielectric environment," *The Journal of Physical Chemistry C*, vol. 111, no. 11, pp. 4180–4184, Mar 2007.
- [163] H. King and J. Wong, "An experimental study of a balun-fed open-sleeve dipole in front of a metallic reflector," *Antennas and Propagation, IEEE Transactions on*, vol. 20, no. 2, pp. 201–204, Mar 1972.
- [164] A. Rakic, A. Djurisic, J. Elazar, and M. Majewski, "Optical properties of metallic films for vertical-cavity optoelectronic devices," *Applied Optics*, vol. 37, no. 22, pp. 5271–5283, 1998.
- [165] L. Tang, S. E. Kocabas, S. Latif, A. K. Okyay, D.-S. Ly-Gagnon, K. C. Saraswat, and D. A. B. Miller, "Nanometre-scale germanium photodetector enhanced by a near-infrared dipole antenna," *Nature Photonics*, vol. 2, no. 4, pp. 226–229, Apr. 2008.
- [166] A. Cavallini and L. Polenta, *Characterization of Semiconductor Heterostructures and Nanostructures*. Elsevier, 2008, ch. Electrical characterization of nanostructures, pp. 55–91.
- [167] V. Schmidt, S. Senz, and U. Goesele, "Influence of the Si/SiO₂ interface on the charge carrier density of si nanowires," *Applied Physics A-Materials Science & Processing*, vol. 86, no. 2, pp. 187–191, Feb 2007.
- [168] J. Jie, W. Zhang, K. Peng, G. Yuan, C. S. Lee, and S.-T. Lee, "Surface-dominated transport properties of silicon nanowires," *Advanced Functional Materials*, vol. 18, no. 20, pp. 3251–3257, Oct 23 2008.
- [169] J. D. Plummer, M. D. Deal, and P. B. Griffin, *Silicon VLSI technology : fundamentals, practice, and modeling*. Upper Saddle River, NJ: Prentice Hall, 2000.
- [170] J. Kedzierski, J. Bokor, and C. Kisielowski, "Fabrication of planar silicon nanowires on silicon-on-insulator using stress limited oxidation," *J. Vac. Sci. Technol. B*, vol. 15, no. 6, pp. 2825–2828, 1997.
- [171] C. C. Büttner and M. Zacharias, "Retarded oxidation of Si nanowires," *Applied Physics Letters*, vol. 89, no. 26, p. 263106, 2006.
- [172] D. Shir, B. Liu, A. Mohammad, K. Lew, and S. Mohney, "Oxidation of silicon nanowires," *Journal of Vacuum Science & Technology B*, vol. 24, no. 3, pp. 1333–1336, May-Jun 2006.
- [173] B. Liu, Y. Wang, T. ta Ho, K.-K. Lew, S. M. Eichfeld, J. M. Redwing, T. S. Mayer, and S. E. Mohney, "Oxidation of silicon nanowires for top-gated field effect transistors," *Journal of Vacuum Science & Technology A: Vacuum, Surfaces, and Films*, vol. 26, no. 3, pp. 370–374, 2008.
- [174] S. A. Dayeh, C. Soci, P. K. L. Yu, E. T. Yu, and D. Wang, "Transport properties of InAs nanowire field effect transistors: The effects of surface states," *Journal of Vacuum Science & Technology B*, vol. 25, no. 4, pp. 1432–1436, Jul-Aug 2007.
- [175] G. Cheng, Z. Li, S. Wang, H. Gong, K. Cheng, X. Jiang, S. Zhou, Z. Du, T. Cui, and G. Zou, "The unsaturated photocurrent controlled by two-dimensional barrier geometry

- of a single ZnO nanowire Schottky photodiode," *Applied Physics Letters*, vol. 93, no. 12, p. 123103, 2008.
- [176] D. K. Schroder, *Semiconductor material and device characterization*. IEEE Press ; Wiley, 2006.
- [177] W. M. Weber, L. Geelhaar, A. P. Graham, E. Unger, G. S. Duesberg, M. Liebau, W. Pamler, C. Cheze, H. Riechert, P. Lugli, and F. Kreupl, "Silicon-nanowire transistors with intruded nickel-silicide contacts," *Nano Letters*, vol. 6, no. 12, pp. 2660–2666, 2006.
- [178] Y.-F. Lin and W.-B. Jian, "The impact of nanocontact on nanowire based nanoelectronics," *Nano Letters*, vol. 8, no. 10, pp. 3146–3150, 2008.
- [179] F. Léonard, A. A. Talin, B. S. Swartzentruber, and S. T. Picraux, "Diameter-dependent electronic transport properties of Au-catalyst/Ge-nanowire Schottky diodes," *Physical Review Letters*, vol. 102, no. 10, p. 106805, 2009.
- [180] G. D. J. Smit, S. Rogge, and T. M. Klapwijk, "Scaling of nano-Schottky-diodes," *Applied Physics Letters*, vol. 81, no. 20, pp. 3852–3854, 2002.
- [181] J. Piscator and O. Engström, "Schottky barriers on silicon nanowires influenced by charge configuration," *Journal of Applied Physics*, vol. 104, no. 5, p. 054515, 2008.
- [182] J. Appenzeller, J. Knoch, M. Bjork, H. Riel, H. Schmid, and W. Riess, "Toward nanowire electronics," *Electron Devices, IEEE Transactions on*, vol. 55, no. 11, pp. 2827–2845, Nov. 2008.
- [183] Z. Y. Zhang, C. H. Jin, X. L. Liang, Q. Chen, and L.-M. Peng, "Current-voltage characteristics and parameter retrieval of semiconducting nanowires," *Applied Physics Letters*, vol. 88, no. 7, p. 073102, 2006.
- [184] Z. Zhang, K. Yao, Y. Liu, C. Jin, X. Liang, Q. Chen, and L.-M. Peng, "Quantitative analysis of current-voltage characteristics of semiconducting nanowires: Decoupling of contact effects," *Advanced Functional Materials*, vol. 17, no. 14, pp. 2478–2489, Sep 24 2007.
- [185] R. Agarwal, "Heterointerfaces in semiconductor nanowires," *Small*, vol. 4, no. 11, pp. 1872–1893, Nov 2008.
- [186] A. Colli, S. Pisana, A. Fasoli, J. Robertson, and A. C. Ferrari, "Electronic transport in ambipolar silicon nanowires," *Physica Status Solidi (B)*, vol. 244, no. 11, pp. 4161–4164, 2007.
- [187] A. Colli, A. Fasoli, C. Ronning, S. Pisana, S. Piscanec, and A. C. Ferrari, "Ion beam doping of silicon nanowires," *Nano Letters*, vol. 8, no. 8, pp. 2188–2193, 2008.
- [188] A. Colli, A. Fasoli, S. Pisana, Y. Fu, P. Beecher, W. I. Milne, and A. C. Ferrari, "Nanowire lithography on silicon," *Nano Letters*, vol. 8, no. 5, pp. 1358–1362, 2008.
- [189] S.-M. Koo, M. D. Edelstein, Q. Li, C. A. Richter, and E. M. Vogel, "Silicon nanowires as enhancement-mode Schottky barrier field-effect transistors," *Nanotechnology*, vol. 16, no. 9, pp. 1482–1485, 2005.

- [190] H. Yoshioka, N. Morioka, J. Suda, and T. Kimoto, "Mobility oscillation by one-dimensional quantum confinement in Si-nanowire metal-oxide-semiconductor field effect transistors," *Journal of Applied Physics*, vol. 106, no. 3, p. 034312, 2009.
- [191] A. A. Talin, F. Léonard, B. S. Swartzentruber, X. Wang, and S. D. Hersee, "Unusually strong space-charge-limited current in thin wires," *Physical Review Letters*, vol. 101, no. 7, p. 076802, 2008.
- [192] W. Chandra, L. K. Ang, and W. S. Koh, "Two-dimensional model of space charge limited electron injection into a diode with Schottky contact," *Journal of Physics D-Applied Physics*, vol. 42, no. 5, Mar 7 2009.
- [193] Y. Gu and L. J. Lauhon, "Space-charge-limited current in nanowires depleted by oxygen adsorption," *Applied Physics Letters*, vol. 89, no. 14, p. 143102, 2006.
- [194] C. Yang, C. J. Barrelet, F. Capasso, and C. M. Lieber, "Single p-type/intrinsic/n-type silicon nanowires as nanoscale avalanche photodetectors," *Nano Letters*, vol. 6, no. 12, pp. 2929–2934, 2006.
- [195] S. Jin, M. Fischetti, and T. wei Tang, "Theoretical study of carrier transport in silicon nanowire transistors based on the multisubband Boltzmann transport equation," *Electron Devices, IEEE Transactions on*, vol. 55, no. 11, pp. 2886–2897, Nov. 2008.
- [196] H. E. Ruda and A. Shik, "Polarization-sensitive optical phenomena in semiconducting and metallic nanowires," *Phys. Rev. B*, vol. 72, no. 11, p. 115308, Sep 2005.
- [197] Y. Gu, E.-S. Kwak, J. L. Lensch, J. E. Allen, T. W. Odom, and L. J. Lauhon, "Near-field scanning photocurrent microscopy of a nanowire photodetector," *Applied Physics Letters*, vol. 87, no. 4, p. 043111, 2005.
- [198] Y. Ahn, J. Dunning, and J. Park, "Scanning photocurrent imaging and electronic band studies in silicon nanowire field effect transistors," *Nano Letters*, vol. 5, no. 7, pp. 1367–1370, 2005.
- [199] C. Rossler, K.-D. Hof, S. Manus, S. Ludwig, J. P. Kotthaus, J. Simon, A. W. Holleitner, D. Schuh, and W. Wegscheider, "Optically induced transport properties of freely suspended semiconductor submicron channels," *Applied Physics Letters*, vol. 93, no. 7, p. 071107, 2008.
- [200] Y. H. Ahn and J. Park, "Efficient visible light detection using individual germanium nanowire field effect transistors," *Applied Physics Letters*, vol. 91, no. 16, p. 162102, 2007.
- [201] A. Zhang, S. You, C. Soci, Y. Liu, D. Wang, and Y.-H. Lo, "Silicon nanowire detectors showing phototransistive gain," *Applied Physics Letters*, vol. 93, no. 12, p. 121110, 2008.
- [202] A. L. Falk, F. H. L. Koppens, C. L. Yu, K. Kang, N. de Leon Snapp, A. V. Akimov, M.-H. Jo, M. D. Lukin, and H. Park, "Near-field electrical detection of optical plasmons and single-plasmon sources," *Nat Phys*, vol. 5, no. 7, pp. 475–479, Jul. 2009.
- [203] Y. Gu, J. P. Romankiewicz, J. K. David, J. L. Lensch, and L. J. Lauhon, "Quantitative measurement of the electron and hole mobility-lifetime products in semiconductor nanowires," *Nano Letters*, vol. 6, no. 5, pp. 948–952, 2006.

- [204] S. Thunich, L. Prechtel, D. Spirkoska, G. Abstreiter, A. F. i Morral, and A. W. Holleitner, "Photocurrent and photoconductance properties of a GaAs nanowire," *Applied Physics Letters*, vol. 95, no. 8, p. 083111, 2009.
- [205] I. Wilke, W. Herrmann, and F. K. Kneubühl, "Integrated nanostrip dipole antennas for coherent 30 THz infrared radiation," *Applied Physics B: Lasers and Optics*, vol. 58, no. 2, pp. 87–95, Feb 1994.
- [206] L. Tsypbeskov, D. Lockwood, and M. Ichikawa, "Silicon photonics: CMOS going optical," *Proceedings of the IEEE*, vol. 97, no. 7, pp. 1161–1165, July 2009.
- [207] E. Anemogiannis and E. N. Glytsis, "Multilayer wave-guides - efficient numerical analysis of general structures," *Journal of Lightwave Technology*, vol. 10, no. 10, pp. 1344 – 1351, Oct 1992.
- [208] A. Bakhtazad, H. Abiri, and R. Ghayour, "A general transform for regularizing planar open waveguide dispersion relation," *Journal of Lightwave Technology*, vol. 15, no. 2, pp. 383 – 390, Feb 1997.
- [209] M. S. Kwon and S. Y. Shin, "Simple and fast numerical analysis of multilayer waveguide modes," *Optics Communications*, vol. 233, no. 1-3, pp. 119 – 126, Mar 2004.
- [210] R. Rodriguez-Bernal, F. Mesa, and F. Medina, "Appropriate formulation of the characteristic equation for open nonreciprocal layered waveguides with different upper and lower half-spaces," *IEEE Transactions on Microwave Theory and Techniques*, vol. 53, no. 5, pp. 1613 – 1623, May 2005.
- [211] R. Rodriguez-Bernal, F. Mesa, and F. Medina, "Systematic and efficient root finder for computing the modal spectrum of planar layered waveguides," *International Journal of RF and Microwave Computer-Aided Engineering*, vol. 14, no. 1, pp. 73 – 83, January 2004.
- [212] R. E. Smith, S. N. Houde-Walter, and G. W. Forbes, "Mode determination for planar waveguide using the four-sheeted dispersion relation," *IEEE Journal of Quantum Electronics*, vol. 28, no. 6, pp. 1520 – 1526, Jun 1992.

This dissertation is typeset using X_ET_EX. FF Scala and FF Scala Sans fonts by Martin Majoor, as well as the Minion Math font by Johannes Küster are used for the text and the math parts respectively.